ARL-TR-8456 ● Aug 2018

US Army Research Laboratory

Development of Methodologies for Evaluating Emissions from Metal-Containing Explosives and Propellants

Kevin McNesby, Michael Nusca, Michael McQuaid, Chiung-Chu Chen, Richard Benjamin, Ronnie Thompson, William Sickels, Eugene Summers, Ray Sparks, Brian Gullett, Amara Holder, and Johanna Aurell

NOTICES

Disclaimers

The findings in this report are not to be construed as an official Department of the Army position unless so designated by other authorized documents.

Citation of manufacturer's or trade names does not constitute an official endorsement or approval of the use thereof.

Destroy this report when it is no longer needed. Do not return it to the originator.

ARL-TR-8456 ● Aug 2018

US Army Research Laboratory

Development of Methodologies for Evaluating Emissions from Metal-Containing Explosives and Propellants

Kevin McNesby, Michael Nusca, Michael McQuaid, Chiung-Chu Chen, Richard Benjamin, Ronnie Thompson, and Eugene Summers, ***Weapons and Materials Research Directorate, ARL***

William Sickels and Ray Sparks
Bowhead Total Enterprise Solution LLC, Belcamp, MD

Brian Gullett and Amara Holder
US Environmental Protection Agency, Office of Research and Development, Washington, DC

Johanna Aurell
University of Dayton Research Institute, Dayton, OH

REPORT DOCUMENTATION PAGE

Form Approved
OMB No. 0704-0188

1. REPORT DATE *(DD-MM-YYYY)*	2. REPORT TYPE	3. DATES COVERED (From - To)
August 2018	Technical Report	1 December 2015–31 December 2016

4. TITLE AND SUBTITLE

Development of Methodologies for Evaluating Emissions from Metal-Containing Explosives and Propellants

5a. CONTRACT NUMBER

5b. GRANT NUMBER

5c. PROGRAM ELEMENT NUMBER

6. AUTHOR(S)

Kevin McNesby, Michael Nusca, Michael McQuaid, Chiung-Chu Chen, Richard Benjamin, Ronnie Thompson, William Sickels, Eugene Summers, Ray Sparks, Brian Gullett, Amara Holder, and Johanna Aurell

5d. PROJECT NUMBER

WP-2611

5e. TASK NUMBER

5f. WORK UNIT NUMBER

7. PERFORMING ORGANIZATION NAME(S) AND ADDRESS(ES)

US Army Research Laboratory
ATTN: RDRL-WML-C
Aberdeen Proving Ground, MD 21005-5066

8. PERFORMING ORGANIZATION REPORT NUMBER

ARL-TR-8456

9. SPONSORING/MONITORING AGENCY NAME(S) AND ADDRESS(ES)

Strategic Environmental Research and Development Program and Environmental Security Technology Certification Program Program Offices
901 North Stuart Street, Suite 303
Arlington, VA 22203-1853

10. SPONSOR/MONITOR'S ACRONYM(S)

SERDP, ESTCP

11. SPONSOR/MONITOR'S REPORT NUMBER(S)

12. DISTRIBUTION/AVAILABILITY STATEMENT

Approved for public release; distribution is unlimited.

13. SUPPLEMENTARY NOTES

14. ABSTRACT

Experiments were performed to develop methodologies that will allow determination of pollutant emission factors for gases and particles produced by exploding metal-containing energetic materials. Materials studied included M855 ammunition (nitrocellulose [$(C_6H_7(NO_2)_3O_5)_n$]/nitroglycerin [$C_3H_5N_3O_9$] propellant, copper-jacketed lead projectile) fired using an M4 carbine shoulder-fired weapon, medium-sized (660 g) charges of neat trinitrotoluene (TNT or $C_7H_5N_3O_6$), and medium-sized (660 g total weight) charges of TNT (80% by weight):magnesium (Mg powder, 325 mesh, 4% by weight):boron (B powder, 0.8 μm, 16% by weight). Although not included here, the analysis methods described are directly applicable to the study of pyrotechnics.

15. SUBJECT TERMS

explosives, propellants, metal-containing, pollutant emissions, emissions factors, modified combustion efficiency, TNT, trinitrotoluene, M855

16. SECURITY CLASSIFICATION OF:			17. LIMITATION OF ABSTRACT	18. NUMBER OF PAGES	19a. NAME OF RESPONSIBLE PERSON
a. REPORT	b. ABSTRACT	c. THIS PAGE			Kevin L McNesby
Unclassified	Unclassified	Unclassified	UU	109	19b. TELEPHONE NUMBER (Include area code) 410-306-1383

Standard Form 298 (Rev. 8/98)
Prescribed by ANSI Std. Z39.18

Contents

List of Figures

List of Tables

Preface

This report was prepared under contract to the Department of Defense Strategic Environmental Research and Development Program (SERDP). The publication of this report does not indicate endorsement by the Department of Defense, nor should the contents be construed as reflecting the official policy or position of the Department of Defense. Reference herein to any specific commercial product, process, or service by trade name, trademark, manufacturer, or otherwise, does not necessarily constitute or imply its endorsement, recommendation, or favoring by the Department of Defense.

Acknowledgments

We wish to acknowledge the following from the US Army Research Laboratory: Dr John Schmidt, Dr Rose Pesce-Rodriguez, and Dr Joe South.

Executive Summary

Objective

This document is the final report of a 1-year effort to demonstrate prediction and measurement of emissions from explosions and combustion events produced by metal-based energetic formulations, based upon observed stages of energy release. The work described here compares simulation to experiment for a series of gun firings (an M4 carbine shoulder-fired weapon) and explosions (detonation of metal-containing trinitrotoluene [TNT] formulations). The simulations predict solid and gaseous chemical species produced by explosive events. The experimental work measured gases and particles emitted during testing of these materials and imaged each event. The original Call for Proposals included a request for analysis of pyrotechnics in addition to explosives. Although not included here, the analysis methods described are directly applicable to the study of pyrotechnics.

Facilities

The simulation and experimental work summarized in this report was conducted at the US Army Research Laboratory (ARL) Detonation Science Facility located at Aberdeen Proving Ground, Maryland. Testing at this site occurred in a medium-scale (up to 25 kg net explosive weight) indoor blast facility, employing particle and chemical species diagnostic equipment developed by the US Environmental Protection Agency (EPA), Office of Research and Development. This equipment was designed by the EPA to allow for field use (to include aerostat and drone deployment[1]), in a setting that attempted to bridge the gap between laboratory and field scale. Each explosive event measured using EPA instrumentation was imaged using ARL high-speed cameras and spectrographs. An overall goal of this work was to develop a predictive methodology for toxic chemical species produced during explosions of metal-containing energetic materials, using simulation tools available to most explosives researchers,[2] building upon previous efforts such as POLU13 (Navy), MERLIN (Army), Products of Combustion/Atmospheric Dispersion (PCAD; El Dorado, Inc.), and ADORA (Blaze Tech, Inc.).[3]

[1] Aurell J, Gullett BK, Pressley C, Tabor D, Gribble R. Aerostat-lofted instrument and sampling method for determination of emissions from open area sources. Chemosphere. 2011;85:806–811.

[2] CHEETAH 6.0 user's manual. Berkeley (CA): Lawrence Livermore National Security; 2010. Report No.: LLNL-SM-416166.

[3] O'Brien RJ, Wade MD. Air emissions inventory guidance document for stationary sources at Air Force installations. Brooks Air Force Base (TX): Air Force Institute for Environment, Safety and Occupational Health Risk Analysis; Revised 2003 Dec. Report No.: IERA-RS-BR-SR-1999-0001.

EPA and ARL Instrumentation

Products of energy release for each material tested were measured using a suite of fielded analytical chemical instrumentation developed by the EPA's Office of Research and Development for measuring particles and chemical species during testing of munitions.[1] The instruments employed included extractive particle analyzers (2 to 100 μm) and extractive mass spectral detection of permanent chemical species to 450 amu. Metal and soot particles were collected as residues on filters and analyzed using X-ray fluorescence techniques. Permanent gases and volatile organic compounds were analyzed continuously and via canister grab samples.[4] All explosive events were recorded using the ARL Detonation Science Facility suite of high-speed imaging instrumentation. Gun firings were imaged using an Edgerton shadowgraphy system. Explosive events were imaged using a high-speed, high-definition framing camera with and without external illumination. Outdoor tests for air-shock velocity measurements were imaged using a laser-synchronized, low-parallax, high-brightness imaging rig.[5]

Qualitative Approach

Observed stages of energy release for each energetic material tested were similar. In each test, a solid material (explosive or propellant) is rapidly (anaerobically) converted to an underoxidized dense gas/particle cloud. This first stage (burning of the propellant in the gun barrel or detonation of the solid explosive) is responsible for most of the observed energy release. The second stage of energy release in each test involves air oxidation of the underoxidized products of the first stage.[6] For gun firings employing propellants, this second stage is mostly associated with muzzle flash, while for detonations of energetics, the second stage is responsible for the explosive fireball. These stages of energy release were verified for all materials tested, prior to chemical emissions measurement, using high-speed digital imaging and synchronized laser illumination, and are reported here.

The analytical approach used here is that the final chemical emissions from the energy release of all materials tested are dependent upon sequential processes. The simulation effort mimicked each observed stage of energy release using equilibrium thermodynamic and chemical kinetic (CHEMKIN) tools developed specifically for explosive and combustion events. For predicting chemical species emission during

[4] AMCCOM. Development of methodology and techniques for identifying and quantifying products from open burning and open detonation thermal treatment methods-field test series A, B and C, vol. 1, test summary. Rock Island (IL): Armament Munitions & Chemical Command; 1992 Jan.

[5] McNesby KL, Homan BE, Benjamin RA, Boyle VM, Densmore JM, Biss MM. Quantitative imaging of explosions with high-speed cameras. Rev Scientific Instruments. 2016;87:051301.

[6] McNesby KL, Homan BE, Ritter JJ, Quine Z, Ehlers RZ, McAndrew BA. Afterburn ignition delay and shock augmentation in fuel rich solid explosives. Propellants Explos Pyrotech. 2010;35(1):57–65.

the first stage of energy release, the NASA-Lewis (or NASA-Glenn) equilibrium thermochemical simulation computer code was used for gun firings[7]; the equilibrium thermochemical simulation computer code CHEETAH was employed for detonations.[2] For the second stage of energy release, flow dynamics coupled to NASA-Lewis equilibrium calculations[8] or finite-rate CHEMKIN calculations (CHEMKIN combustion simulator, Reaction Design, Inc) were used to predict final emissions for gun firings. For solid explosives, the CHEMKIN combustion simulator was used to predict species present in the fireball following detonation.[2,6,9]

Gun Firing Results

In general, for the gun firings, metal species produced by the event were found in particles. Carbon species produced by the event were found in gases and particles. The metal detected in highest concentration following the M4 carbine firing is copper (Cu) (in the range of 50 g per kilogram of propellant), which originates from the bullet casing rather than the propellant. Lead (Pb) is detected for all tests, at approximately 1/3 the level of Cu. The source of the Pb is believed to be in the propellant ignition train; it is present in the No. 41 primer used to initiate the propellant and in the bullet core (cased in a Cu jacket). The sensitivity of the EPA detection methods is illustrated by the measurement of potassium (K) in the "salted" rounds, at about 1/2 the detected level of Cu (K is added as a combustion-radical scavenger to suppress muzzle flash[10] and is not in the "unsalted" rounds). The measured particles were distributed approximately evenly between $PM_{2.5}$ and PM_{10} (emitted total particles approximately 57 g per kilogram "salted" propellant, approximately 32 g per kilogram "unsalted" propellant), at levels similar to previous studies.[11] Unsalted (no K flash suppressant) and legacy (Vietnam-era) M855 rounds exhibited similar particle emissions, while the salted rounds exhibited higher particle concentrations, likely caused by suppression of second-stage combustion by the added K.

For all gun firings, carbon present in the double-base propellant (nitrocellulose [83% by weight]/nitroglycerin [13% by weight]) is distributed between particles and gaseous carbon monoxide (CO) and carbon dioxide (CO_2). However, the

[7] Gordan S, McBride BJ. Computer program for calculation of complex chemical equilibrium compositions and applications. Cleveland (OH): NASA-Glenn; 1994 Oct. Report No.: 1311.

[8] Nusca MJ. Recent upgrades to the ARL-NGEN3 computational interior ballistics model. Aberdeen Proving Ground (MD): Army Research Laboratory (US); 2011 Aug. Report No.: ARL-TR-5613.

[9] Kotlar AJ. The thermodynamics of interior ballistics and propellant performance. Proceedings 29th JANNAF Combustion Meeting; 1992 Oct; CPIA Publication 593.

[10] Glassman I. Combustion. 2nd ed. San Diego (CA): Academic Press; 1987. p. 360–375.

[11] Wingfors H, Svensson K, Hagglund L, Hedenstierna S, Magnusson R. Emission factors for gases and particle-bound substances produced by firing lead-free small-caliber ammunition. J Occup Environ Hyg. 2014;11:282–291.

measured "modified combustion efficiency" (MCE), an indicator of the extent of carbon oxidation,[12] is near 0.44 (legacy) and 0.5 (salted and unsalted), indicating that at the EPA sensor position, the total initial carbon is underoxidized. Total measured gaseous carbon emitted for all gun firings was around 500 g per kilogram of propellant (see Section 13 for details) with CO_2 measured concentrations slightly higher than CO. Hydrogen cyanide gas was not tested here, although it is expected to be present for firings of all rounds tested here at an emission factor near 1 mg per gram of propellant consumed.[13]

This is in slight contrast to the gun simulations, which predict gun-emitted gaseous carbon to be present at the sensor position mostly as CO_2 and as methane (CH_4). Two simulations were performed. The main effort used a modified NASA-Lewis thermochemical code coupled to computational flow dynamics (CFD) to estimate gases at the muzzle exit and at the EPA sensor position (~15 cm from the muzzle of the M4 carbine).[8] This simulation predicted most gaseous carbon at the sensor position present as CO_2, with about one third as much CH_4, and trace amounts of CO, yielding a predicted MCE near 0.73. This modified NASA-Lewis simulation was used because it allows for varying levels of soot production during the interior ballistic cycle and accurately depicts the time-delay as muzzle gases diffuse to the EPA sensors. A second effort, described briefly in Appendix A, used a combination of CHEETAH gun calculations coupled to CHEMKIN.[2] This simulation predicted full carbon oxidation and a MCE of 0.997. Both methods of simulation overpredict carbon oxidation, relative to measurement, with the NASA-Lewis/CFD giving results much closer to measurement. This discrepancy is discussed in detail in this report.

Overall, we believe the main areas for improvement in the gun effort are in the simulation of soot and particle production during interior ballistics, and the simulation of particle combustion during exterior ballistics. Additionally, it is worth emphasizing that simulations do not account for metal particle combustion during the second phase of energy release.

Detonations of Solid Explosives Results

For studies of chemical emissions following detonation of solid chemical explosives, TNT was selected as the base explosive, because it is extremely well

[12] Sinha P, Hobbs PV, Yokelson RJ, Bertschi IT, Blake DR, Simpson IJ, Gao S, Kirchstetter TW, NovakovT. Emissions of trace gases and particles from savanna fires in southern Africa. J Geophys Res. 2003;108:8487. doi:10.1029/2002JD002325.

[13] Kirchner DB, Gaydos JC, Battigelli MC. Combustion products of propellants and ammunition. In Occupational health: the soldier and the industrial base. Aberdeen (MD): Office of the Surgeon General, Department of the Army (US); Bethesda (MD): Army Environmental Hygiene Agency (US); and Washington (DC): Uniformed Services University of the Health Sciences; 1993.

characterized, its stages of energy release form the basis for the approach used in this study, and particles of graphitic carbon are predicted as a major species (mole fraction) following detonation (luminescence from condensed carbon is responsible for the yellow color of the TNT fireball).[5] The magnesium (Mg)/boron (B) additive was selected because it is a metal additive designed to overcome thermodynamic limitations on realizing full-combustion enthalpy for B on detonation timescales.[14] The TNT:Mg:B ("hot mill alloy", 80:4:16 by weight, stoichiometry approximately MgB_2) formulation therefore allows study of pollutant emission by explosions that produce carbonaceous particles, study of metal additives known to combust when formulated in explosives (Mg), and study of metal additives (B) for which full explosive performance has yet to be realized. The loading level (20% metal by weight) was selected because it is similar to the loading level of the aluminum (Al)-containing fielded explosive formulation Tritonal (80% TNT, 20% Al powder).[15]

As with the gun firings, metals in the explosive formulations are found after testing in the emitted particles, and carbon is found in the emitted gases and particles. Metals detected in highest concentration following detonation/explosion of "neat" (i.e., pure) TNT within the blast chamber are iron and Al, at less than 20 g per kilogram of explosive formulation, likely from fixtures in the test environment and the blast chamber walls. B and Mg are detected at trace levels (as are all other tested metals) following detonation of neat TNT. The experimental MCE for all detonations/explosions of neat TNT is near 0.98, indicating most of the carbon measured following explosion is fully oxidized. For detonation/explosion of the TNT:Mg:B formulation, B and Mg are the metals detected at highest concentration after explosion, with measured particle masses approaching 300 g per kilogram of explosive formulation. The full elemental analysis of the B- and Mg-containing particles was not available at time of this writing. The measured MCE for the TNT:Mg:B formulations was near 0.98, indicating initial carbon was fully oxidized.

It is expected that during explosion, anaerobic (first-stage energy release) reaction of metals in metal-containing explosive formulations will decrease available oxygen, increasing the level of carbonaceous soot/particles.[6] This is seen in experiment and in simulation. For the detonation/explosion simulations, the CHEETAH simulation of the first stage of energy release allows the choice of the B additive to be inert (inactive) or reactive (active). Mg is always active. In the CHEMKIN simulation of the second stage of energy release (afterburn or fireball), particle combustion is ignored, and the simulation approximates the afterburn as

[14] Kuo KK, Acharya R. Ignition and combustion of single energetic solid particles. New York (NY): John Wiley and Sons, Inc; 2012.

[15] Meyer R, Kohler J, Homburg IA. Explosives. 6th ed. Berlin (Germany): John Wiley & Sons, Wiley-VCH Verlag GmbH and Co; 2007.

occurring in a homogeneous (single-phase, well-mixed) reactor. For all simulations, the calculated MCE (0.86 for neat TNT, approaching 0.76 for metallized formulations) was in reasonable agreement (within 15% to 25%) with experiment.

It is worth noting that for detonations within the ARL blast chamber, shock reflections from the interior walls stir the detonation product gases, promoting afterburn. Additionally, because the CHEETAH simulation predicts condensed products for the first-stage energy release, the calculated emission factors (CHEETAH + CHEMKIN) neglect particle combustion, yielding values less than measured by experiment.

Summary

Overall, we believe the main areas for improvement in the gun effort are in the simulation of soot and particle production during interior ballistics and the simulation of particle combustion during exterior ballistics. Of particular concern is the high level of CO gas measured following firing of the M4 carbine. For measurements and simulation of metal-containing explosives, the main areas for improvement are in prediction of particle combustion during the second stage of energy release and eventual incorporation of heterogeneous reaction chemistry into fluid dynamic modeling. The methodology of using computer simulation to predict emissions of sequential stages of energy release is well known and provides the ability to estimate emissions over a wide range of gun firing and detonative conditions, from firing within an enclosed position, to open air firing, to detonation within closed volumes, to open detonations. Other shortcomings of this work are mostly on the simulation side, and include the lack of predictive ability for most polycyclic aromatic hydrocarbons and the general need for reduced CHEMKIN mechanisms that are amenable to insertion into CFD.

1. Introduction

This document is the final report of a 1-year effort to demonstrate prediction and measurement of emissions from explosions and combustion events produced by metal-based energetic formulations, based upon observed stages of energy release. The work described here compares simulation to experiment for a series of gun firings (an M4 carbine shoulder-fired weapon) and explosions (detonation of metal-containing trinitrotoluene [TNT] formulations). The simulations predict solid and gaseous chemical species produced by explosive events. The experimental work measured gases and particles emitted during testing of these materials and imaged each event.

2. Small-Caliber Gun Propulsion

2.1 Background

2.1.1 Prediction of Product Species for Small-Caliber Gun Firings

A gun is similar in essence to a piston-type internal combustion engine. The gun function is similar to the power stroke of a four-cycle engine, with the expansion of hot gases driving a projectile instead of a piston. When the propelling charge (made up of propellant "grains") behind the projectile (bullet) is ignited, gases are evolved from the surface of the burning propellant grains, and the pressure in the temporarily sealed chamber (breach-sealed gun barrel) increases rapidly. Resistance to initial motion of the projectile is high and relatively high chamber pressures are attained before motion of the projectile occurs. The chemistry and physics within the sealed chamber volume, prior to bullet "uncorking", are considered part of the topic of gun interior ballistics (IB). As the projectile begins to move within the gun barrel, the chamber volume is increased and the rate of burning of the solid propelling charge increases. The net effect is a rapid increase in the pressure within the chamber until the point of maximum pressure is reached. This usually occurs at a relatively short distance from the origin of barrel rifling. Beyond that point, the pressure drops and prior to bullet exit reaches a value from 10% to 30% of maximum, depending upon the weapon design and propellant type. This pressure at muzzle exit continues to act on the projectile for a short distance beyond the muzzle, accelerating the projectile beyond the muzzle (Jones et al. 1965).

As the projectile exits the gun barrel, hot, dense, fuel-rich propellant gases and particles (usually soot) push into surrounding air, creating an air shock wave. These

propellant product gases are typically fuel rich (underoxidized). If the gases and particles are hot enough, they may incandesce, producing a light with a gray-body emission signature near the muzzle exit. As the gases expand and mix with air, they may also combust, emitting light that is a combination of incandescence and discrete emission from flame-propagation combustion radicals, such as methylidyne and diatomic carbon (McNesby et al. 2016). The light emission from hot particles at muzzle exit and combustion of fuel-rich propelling particles and gases after mixing with air is responsible for the muzzle "flash" seen for most firings of small-caliber guns (for the discussion here, bullet diameter of 12.5 mm and below). Within a few to tens of centimeters after bullet exit from the gun barrel, aerodynamic drag causes the expelled gases and particles to lose much of their forward velocity, and the bullet emerges from the propellant gases and moves downrange. The chemistry and physics of the gases and particles after the projectile exits from the gun barrel and the disposition of the projectile after barrel exit are considered part of the topic of gun exterior ballistics.

For the shoulder-fired M4 carbine, firing M855 ammunition (5.56-mm-diameter bullet), the bullet velocity is near 890 m/s. Figure 1 (top) shows an M4 carbine in a rig designed to allow remote firing of the weapon during high-speed imaging. Figure 1 (bottom) is a series of shadowgraphs showing bullet exit from the M4 carbine and expansion of the propelling gases as the bullet travels downrange.

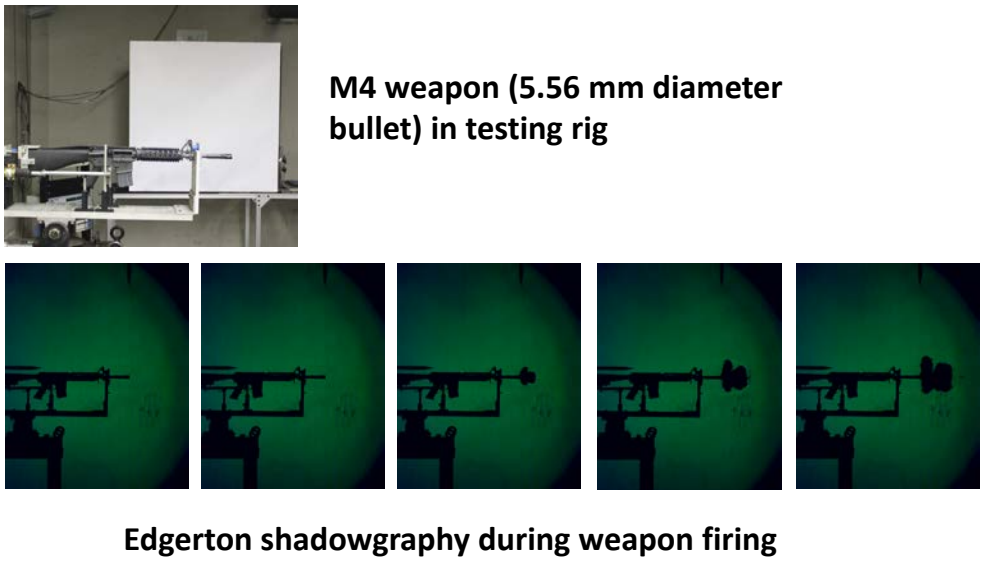

Fig. 1 (Top) The M4 carbine shoulder-fired weapon in an experimental fixture; (bottom) sequential Edgerton shadowgraphy images of bullet "uncorking" and propellant gas expansion

As described, prediction of chemical species (gases and particles) from firing of small-caliber guns must take into account chemical and physical processes occurring in the domains of interior and exterior ballistics. For firing of the M4

carbine using a double-base propellant (nitrocellulose [NC] and nitroglycerin [NG]), chemical species are produced during the sequential stages of energy release. The first stage is the anaerobic propellant burning (deflagration) and gas expansion within the gun barrel. The second stage is the reaction of the deflagration products with the ambient air.

The approach we employ to predict final products of detonations/explosions attempts to simulate, and link, the two stages of energy release described previously. For gun firings, we use equilibrium chemical calculations to predict anaerobic deflagration product species (first stage) followed by flow dynamics coupled to equilibrium thermochemistry to calculate air combustion of these detonation products (second stage). The initial chemical species produced during detonation and anaerobic expansion and their relative amounts, density, and temperature are predicted by the NASA-Lewis (NASA-Glenn) equilibrium simulation computer code (Gordan and McBride 1994). We approximate the end of the first stage of energy release as the density and temperature at which chemical species stop changing (i.e., "freeze out"). For most energetic materials, this occurs near a temperature of 1800 K. These species are expanded into air to simulate second-stage energy release and yield final products.

2.1.2 Converting from Mass/Mass Carbon to Mass/Mass Initial Source

The emission ratio of each analyte/species of interest was calculated from the ratio of background-corrected target analyte concentrations to background-corrected carbon dioxide (ΔCO_2) and carbon monoxide (ΔCO) concentrations. Emission factors (EFs) were calculated using these emissions ratios following the carbon balance method (Burling et al. 2010) and presented as mass pollutant per mass of charge weight. Equations 1 and 2 describe the method employed for calculation of EFs for chemical species and elements, respectively:

$$EF_i = f_c \times \frac{Anlyte_i}{\sum C_j}, \quad (1)$$

where

EF_i = EF of target analyte i in terms of mass pollutant per mass initial source

fc = mass fraction of carbon in the initial source

$Analyte_i$ = the mass emission ratio of species i

ΣC_j = the background corrected mass concentration of carbon in major carbon emissions species j (carbon calculated from ΔCO_2 and ΔCO)

The majority of the carbon emissions were emitted as CO_2 and CO. With this assumption, CO_2 and CO are the only carbon-containing compounds that were required to be measured at each measurement location:

$$EF_{Element_i} = EF_i \times \frac{1}{F_{Element}}, \quad (2)$$

where

$EF_{Element_i}$ = EF of target analyte i in terms of mass metal per mass metal in initial source

EF_i = EF of target analyte i in terms of mass pollutant per mass initial source

$F_{Element}$ = mass fraction of element in the initial source

Standard deviations, as well as the relative standard deviations (RSDs), were used for showing the measure of dispersion of three or more data values. The relative percent difference (RPD) was used as a quality indicator when only two data values (duplicate samples) were obtained. Single factor one-way analysis of variance (ANOVA) with a level of significance $\alpha = 0.05$ was used to determine any differences in emissions between 855 salted and legacy rounds. To establish significant difference, the ANOVA-returned p value (significant value) has to be less than level of significance (0.05) and the $F=F/F_{crit}$ value has to be greater than 2.0.

2.1.3 Modified Combustion Efficiency (MCE)

Comparison of simulations with measurements of chemical species emissions from explosions and combustion events can be challenging. Simulations may often focus on estimation of concentrations of permanent gases (e.g., CO_2, nitrogen oxide [NO_x], water [H_2O], CO, and so on) while measurements may focus on emissions of gaseous and particle species in minute quantities or for which thermodynamic or kinetic parameters are incomplete (e.g., hydrogen cyanide [HCN], hydrogen sulfide [H_2S], polycyclic aromatics, and so on). A metric amenable to both simulation and measurement is combustion efficiency (CE; Sinha et al. 2003). CE is the molar ratio of carbon emitted as CO_2 from an explosion/combustion event to the total excess carbon emitted (Ward and Radke 1993). The excess, given the symbol Δ and

expressed as a mole fraction, is the concentration of a species above ambient concentration. CE is then given by

$$CE = \Delta C_{CO2} / (\Delta C_{CO2} + \Delta C_{CO} + \Delta C_{CH4} + \Delta C_{NMOC} + \Delta C_{PC}), \quad (3)$$

where the subscripts NMOC and PC refer to nonmethane organic carbon and particulate carbon, respectively. Equation 3 is often modified, depending on the difficulty of measuring NMOC and PC (Ward and Radke 1993). As used in this report, modified CE (MCE) is given by

$$MCE = \Delta C_{CO2} / (\Delta C_{CO2} + \Delta C_{CO} + \Delta C_{CH4} + \Delta C_{PC}). \quad (4)$$

It is worth noting that neglecting NMOC and PC in calculation of MCE has been reported to result in errors of less than a few percent, compared to calculations of CE (Sinha et al. 2003).

2.2 Materials: M4 Carbine

Three types of ammunition rounds were used:

- Unsalted: X7468 M855 non-salt-coated SMP842 with propellant weight equal to 26.4 gr (1.71 g) per round (copper [Cu] jacketed lead bullet, bullet is 5.56 mm in diameter, no additives in propellant for muzzle flash reduction).
- Salted: X7393 M855 SMP842 with propellant weight 26.1 gr (1.69 g) per round. No additive in propellant to reduce muzzle flash.
- Legacy (Vietnam-era ammunition, for comparison to modern issue): Same composition as unsalted round, but approximately 30 years older. No additive in propellant to reduce muzzle flash.

The "salted" rounds contained potassium nitrate (KNO_3) for improved ignition behavior and suppressed flash. All three round types contained a no. 41 primer. The composition percentage and carbon fraction (F_C) for these rounds are found in Tables 1 and 2.

Table 1 F_C and metal fractions (e.g., antimony mass fraction is F_{Sb}) in each ammunition round, propellant and primer

Test item	F_C	F_{Pb}	F_{Al}	F_{Ba}	F_{Sb}	F_S	F_{Bi}	F_K
855	0.31	0.0034	0.0010	0.0007	0.0046	0.0009	0.0020	NA
855 salted	0.31	0.0035	0.0014	0.0034	0.0022	0.0009	0.0020	0.0027
Legacy	0.31	0.0034	0.0010	0.0007	0.0046	0.0009	0.0020	NA

NA = not applicable (not in the composition).

Table 2 Composition in each ammunition round, propellant, and primer

Test item	855 salted mg/round	855 mg/round	Legacy mg/round
Propellant NC	1,346.0	1,373.9	1,373.9
NG	226.6	229.3	229.3
Graphite	3.4	3.4	3.4
Ethyl centralite	65.9	66.7	66.7
Diphenylamine	20.3	20.5	20.5
Elemental bismuth	3.4	3.4	3.4
KNO_3	11.8	NA	NA
Lead styphnate	13.0	13.0	13.0
Pentaerythritol tetranitrate (PETN)	1.8	1.8	1.8
Aluminum (Al) powder	2.5	2.5	2.5
Barium nitrate	11.2	11.2	11.2
Antimony sulfide	5.3	5.3	5.3
Tetracene	1.4	1.4	1.4

NA = not applicable (not in the composition).

It must be pointed out that the M855 ammunition used in what is described here is not the currently fielded M855A1 “green” lead (Pb)-free ammunition. The M855 ammo was used in these tests because a Cu-jacketed Pb projectile was desired for this study. Figure 2 shows a photograph of an M855 round, together with a schematic showing the components of the round.

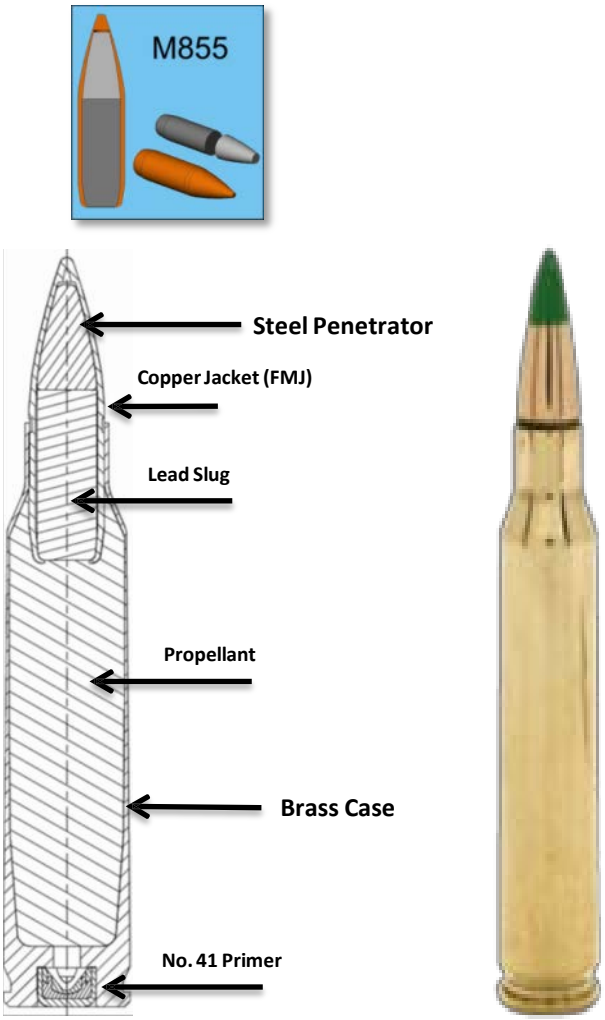

Fig. 2 A photograph of an M855 round, together with a schematic showing the components of the round

2.3 Methods

2.3.1 Target Analytes and Collected Target Analytes

The target analytes for the M4 gun firings are listed in Table 3. CO_2 and CO were successfully measured continuously through all tests. The total number of target analyte samples collected for each type of ammunition are shown in Table 4. The aim was to obtain three replicates of each target compound for 855 salt and two replicates from each of 855 and legacy since they consisted of the same composition. To obtain detectable levels of polycyclic aromatic hydrocarbons (PAHs), only replicate samples were collected.

Table 3 Target analytes for the M4 gun firings

Analyte	Instrument/method	Frequency
CO_2	Nondispersive infrared (NDIR)	Continuous
CO	Electrochemical cell	Continuous
$PM_{2.5}$[a]	Impactor, Teflon filter	Batch
PM_{10}[b]	Impactor, Teflon filter	Batch
NC	Glass fiber filter	Batch
Nitroaromatics	Glass fiber filter	Batch
PAHs	Glass fiber filter and polyurethane foam (PUF)	Batch
Elements	Teflon filter from $PM_{2.5}$ and PM_{10} batch filter	Batch
Volatile organic compounds (VOCs)	SUMMA canister	Batch
PM size distribution	Electrical low-pressure impactor	Continuous and batch
PM composition/size	Single-particle soot photometer	Continuous and batch

Note: PM=particulate matter.
[a]Fine particles in the ambient air with nominal diameters less than or equal to 2.5 μm.
[b]Fine particles in the ambient air with nominal diameters less than or equal to 10 μm.

Table 4 Collected target analytes from each type of ammunition

Analyte	855 salt	855	Legacy	Total
$PM_{2.5}$	3	2	2	7
PM_{10}	3	2	2	7
Nitroaromatics	3	2	2	7
Elements	6	4	4	14
VOCs	3	2	1	6
PAHs	2	2	2	6
PM size	6	4	7	17
PM size/composition	6	6	9	21

2.3.2 Samplers and Analytical

A remotely controlled sampling system, including a computer and control software, was used to sample for the target analytes shown in Table 3. The sampling system computer was connected to an external computer via an Ethernet cable enabling the samplers to be controlled outside of the gun room. All sensor data and flow rates were logged on the sampling system's computer.

CO_2 was continuously measured using an NDIR instrument (LI-COR 820 model, LI-COR Biosciences, Lincoln, NE). This unit is configured with a 14-cm optical bench, giving it an analytical range of 0–20,000 ppm with an accuracy specification of less than 3% of reading. The LI-820 was calibrated in accordance with US Environmental Protection Agency (EPA) Method 3A (EPA 1989), undergoing a three-point, zero, and calibration drift test. All gas cylinders used for calibration

were certified by the suppliers to be National Institute of Standards and Technology (NIST) traceable standards. A precision dilution calibrator, Serinus Cal 2000 (American ECOTECH LC, Warren, RI), was used to dilute the high-level span gases to appropriate levels for the CO_2 LI-COR calibration curves.

CO was continuously measured using an electrochemical gas sensor (e2V EC4-500-CO, SGX Sensortech, UK), which measures CO concentration by means of an electrochemical cell through CO oxidation and changing impedance. The E2v CO sensor has a detection range of 1–500 ppm with resolution of 1 ppm and sensitivity of 55–85 nA/ppm. The temperature and relative humidity (RH) operating range is –20 to +50 °C and 15 to 90% RH, respectively. The response time is less than 30 s. Output is nonlinear from 0 to 500 ppm. A calibration curve has been calculated in the EPA Metrology Laboratory at 0 to 100 ppm with ±2 ppm error using EPA Method 3A (EPA 1989). The sensor was calibrated for CO on a daily basis in accordance with EPA Method 3A (EPA 1989). A post drift check was conducted after each test day. All gas cylinders used for calibration were certified by the suppliers that they are NIST traceable. A precision dilution calibrator, Serinus Cal 2000 (American ECOTECH LC, Warren, RI), was used to dilute the high-level span gases for acquiring the midpoint concentrations for the e2V EC4-500-CO calibration curves. During testing, it was found that the CO levels inside the M4-carbine test enclosure exceeded the CO detection range of 500 ppm. A second CO and CO_2 inlet was added to the test chamber in which the gases from the test chamber were diluted with nitrogen (N_2) to a ratio of approximately 15:1.

$PM_{2.5}$ and PM_{10} were sampled with SKC impactors using 47-mm tared Teflon filters with a pore size of 2.0 µm via Leland Legacy sample pumps (SKC Inc., Covington, GA) with a constant airflow of 10 L/min. PM was measured gravimetrically following the procedures described in 40 CFR Part 50 (EPA 2014a, 2014b). Particles larger than 10 µm in the PM_{10} impactor (or larger than 2.5 µm in the $PM_{2.5}$ impactor) were collected on an oiled 37-mm impaction disc. The Leland Legacy sample pumps were calibrated with a Gilibrator Air Flow Calibration System (Sensidyne LP, St Petersburg, FL).

PM collected on the Teflon filters was used to determine metal concentrations through analysis by energy-dispersive X-ray fluorescence spectrometry according to EPA Compendium Method IO-3.3 (EPA 1999a). B was analyzed by inductively coupled plasma using EPA Compendium Method IO-3.4 (EPA 1999b).

VOCs were sampled via EPA Method TO-15 (EPA 1999c). Sampling for VOCs was accomplished using laboratory-supplied 6-L SUMMA canisters. Each SUMMA was equipped with a manual valve, metal filter, orifice, pressure gauge, pressure transducer, and an electronic solenoid valve. The SUMMA's sampling rate

through the orifice was approximately 0.5 L/min. The SUMMA valves were checked for leakage before sample collection by ensuring that the pressure gauge was not showing decreased pressure with time. The electronic solenoid valve sampling system is opened and closed based on operator-set CO_2 concentration set points using the sampling system's control software program. When the LI-820 measures elevated levels of CO_2, the software enables the solid-state relay, opening the SUMMA's solenoid valve to start sampling. The SUMMA canisters were analyzed by ALS Environmental (Simi Valley, CA) using EPA Method TO-15 (EPA 1999c) using full scan mode gas chromatograph/low-resolution mass spectrometer (GC/LRMS). The SUMMA canisters were also analyzed for CO_2, CO, and methane (CH_4) by a GC/ flame ionization detector according to modified EPA Method 25C (EPA 2017).

Particle-bound and gas phase PAHs were sampled using a PUF/XAD-2/PUF sorbent (modified EPA Method TO-9A [EPA 1999d]) preceded by a quartz microfiber filter with a sampling rate of 0.005 m^3/min (Leland Legacy pump). The PUF/XAD-2/PUF cartridge was purchased pre-cleaned from Supelco (Bellefonte, PA). The glass cartridge is 2.2 cm in outer diameter and 10 cm long with 1.5 g of XAD-2 sandwiched between two 3-cm PUFs. The Leland Legacy pump was calibrated with a Gilibrator Air Flow Calibration System (Sensidyne LP, St Petersburg, FL). The target PAH compounds (naphthalene, acenaphthylene, acenaphthene, fluorene, phenanthrene, anthracene, fluoranthene, pyrene, benzo(a)anthracene, chrysene, benzo(b)fluoranthene, benzo(k)fluoranthene, benzo(a)pyrene, indeno(1,2,3-cd)pyrene, dibenz(a,h)anthracene, and benzo(ghi) perylene) were analyzed using a modified EPA Method 8270D (Wingfors et al. 2014).

Labeled standards for PAHs were added to the XAD-2 traps before the samples were collected. The surrogate recoveries are measured relative to the internal standards and are a measure of the sampling cartridge collection efficiency. Internal standards were added before mass analysis. The filter, XAD, and PUF were combined in a Soxhlet extractor and spiked with quantitation internal standards for PAHs. The extraction was conducted by toluene. After extraction, the extracts were concentrated with a three-ball Snyder column (no rotary evaporation). The three-ball Snyder setup is only able to concentrate down to 50–100 mL so the solution was filtered and transferred to a TurboVap device (Biotage, Sweden) for nitrogen blow-down concentration. The extract final volume was 1 mL. Prior to analysis, a recovery spike was added to determine the percent recovery of the internal standards through the extraction process. PAH analyses were conducted by GC/LRMS selected ion monitoring. The target PAHs are the 16 PAH priorities of

the EPA. PAH EFs were evaluated using toxic equivalent factors relative to benzon[a)-pyrene toxicity equivalent (Larsen and Larsen 1998).

Energetics, including nitroaromatics, NC, and their byproducts, were sampled using a $PM_{2.5}$ impactor with a quartz fiber filter (Fisher Scientific, Hampton, NH). A Leland Legacy pump sampled at a constant flow rate of 10 L/min. The filters were analyzed by APPL Inc. (Clovis, CA) following analytical methods of the EPA Method 8330b (EPA 2006) for nitroaromatics and possible degradation products and EPA Method 353.2 (EPA 1993) for NC by a nitrate-nitrite colorimetric method.

Continuous measurements of particle size distributions were sampled with a porous tube dilution probe and an eductor (DI500, Dekati Ltd, Finland.), with nitrogen as the diluent. The particle size distribution of the diluted emissions was measured with an electrical low-pressure impactor (ELPI; Dekati Ltd, Finland) continuously following gun firing at a 2-s time resolution. For some of the gun firings, polycarbonate filters were placed on the ELPI impactor plates for a gravimetric measurement of the particle size distribution. A single particle soot photometer (SP2) also continuously measured the size distribution of particles that both incandesced and scattered light at 1064 nm at a 1-s time resolution. The SP2 had a secondary dilution flow of nitrogen to further reduce the particle concentration to keep within the range of the instrument. The SP2 had two incandescence photomultiplier tube detectors, a "blue" detector measuring incandescent light from 300–550 nm and a "red" detector measuring incandescent light from 580–710 nm. The color ratio is the ratio of the signal from the two detectors and provides a measure of the temperature at which the particle incandesces and can be used to infer particles of different chemical composition.

2.3.3 Test Chamber

The testing rig for gun firings consisted of an M4 carbine shoulder-fired weapon firing M855 ammunition (Schmidt and Nusca 2009), a polymethylmetacrylate (PMMA; also referred to here as "plexiglass") chamber (0.5 m high × 0.5 m wide × 1.0 m long, 3/8 inch wall thickness) into which the muzzle of the M4 weapon protruded, an extractive chemical/particle analyzer system, and an Edgerton shadowgraphy system for imaging bullet flight and muzzle gases (McNesby et al. 2016). The imaging system enabled verification of proper weapon function (e.g., no bullet fragmentation on launch, bullet launch velocity measurement) and verification of muzzle gases being confined within the sampling chamber. Figure 3 shows a schematic of the testing rig for gun firings. Figure 4 shows A schematic of the extractive chemical and particle analysis system superimposed on a shadowgraph image of an M4 weapon firing.

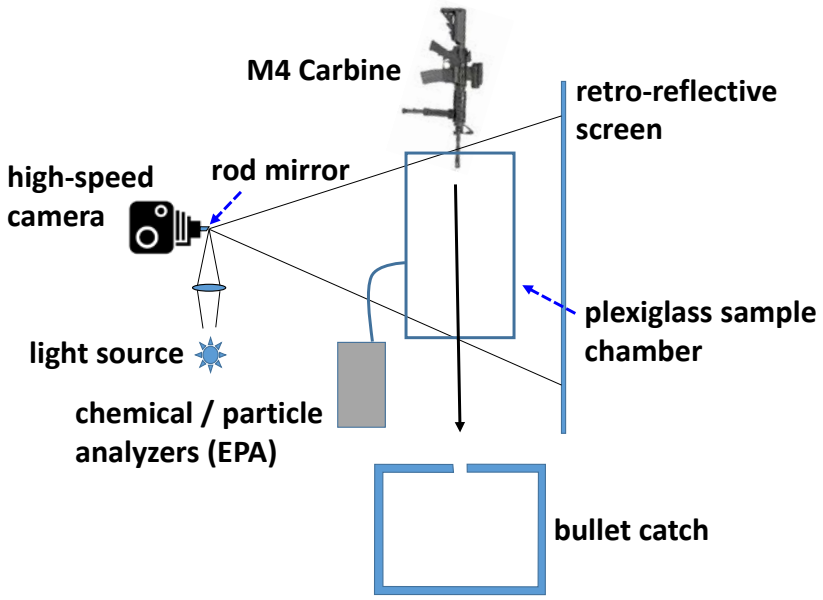

Fig. 3 A schematic of the testing apparatus used for emission measurements following firing of the M4 weapon (M855 ammunition). The PMMA sample chamber is referred to in the figure as "plexiglass".

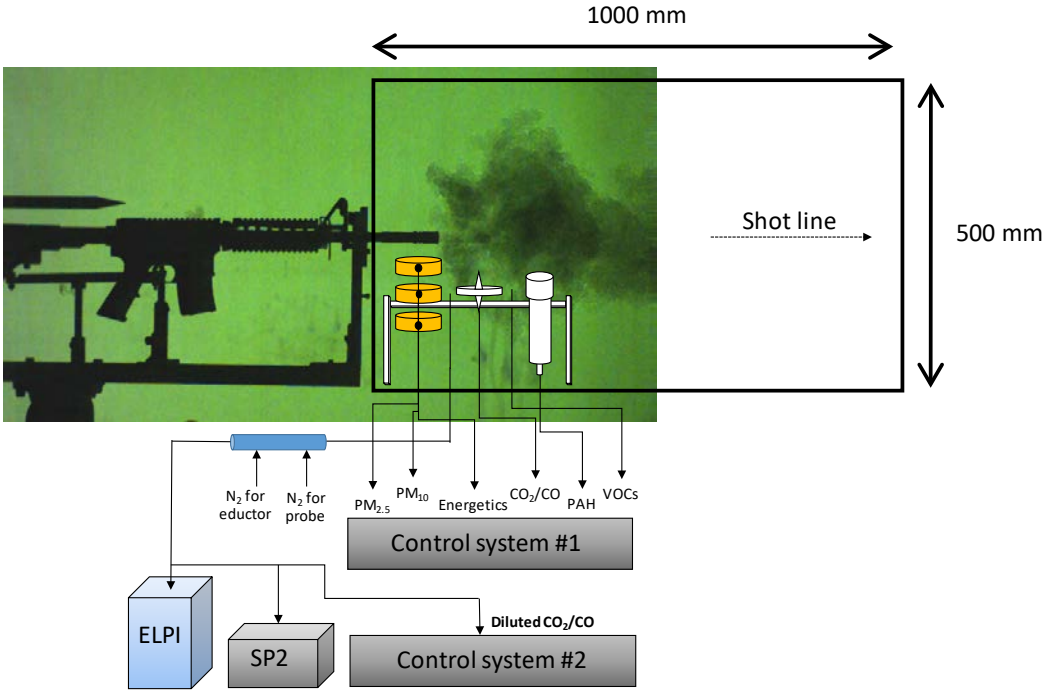

Fig. 4 A schematic of the extractive chemical and particle analysis system superimposed on a shadowgraph image of an M4 weapon firing. The PMMA enclosure is indicated by the heavy black lines in the figure.

A photograph of the testing rig, taken from the vantage point of the imaging system, is shown in Fig. 5. Figure 6 shows the particle and gas samplers within the PMMA enclosure. Figure 7 shows a series of images (times shown are time after initiation of trigger mechanism) during emissions test of the M4 weapon firing salted M855 ammunition.

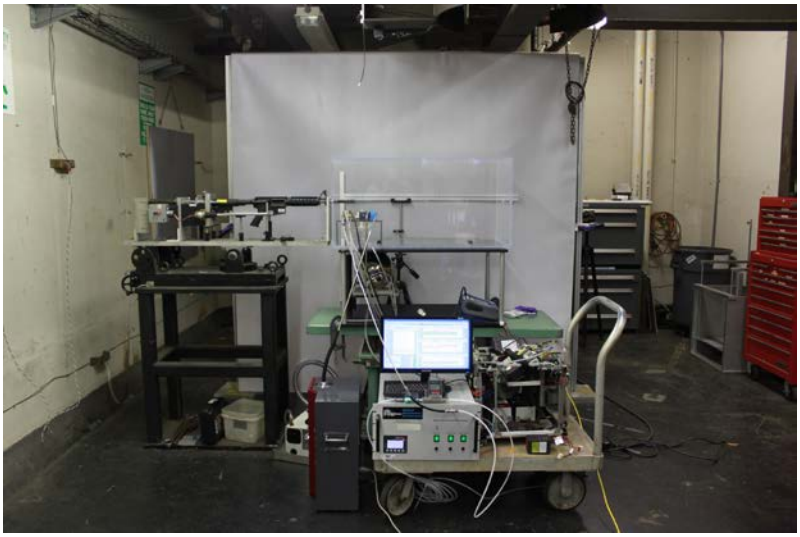

Fig. 5 A photograph of the sampling system used to measure emissions following firing of the M4 weapon. The processors for the in-chamber extractors are on the portable cart.

Fig. 6 The particle and gas samplers within the PMMA enclosure. Note the proximity to the "birdcage".

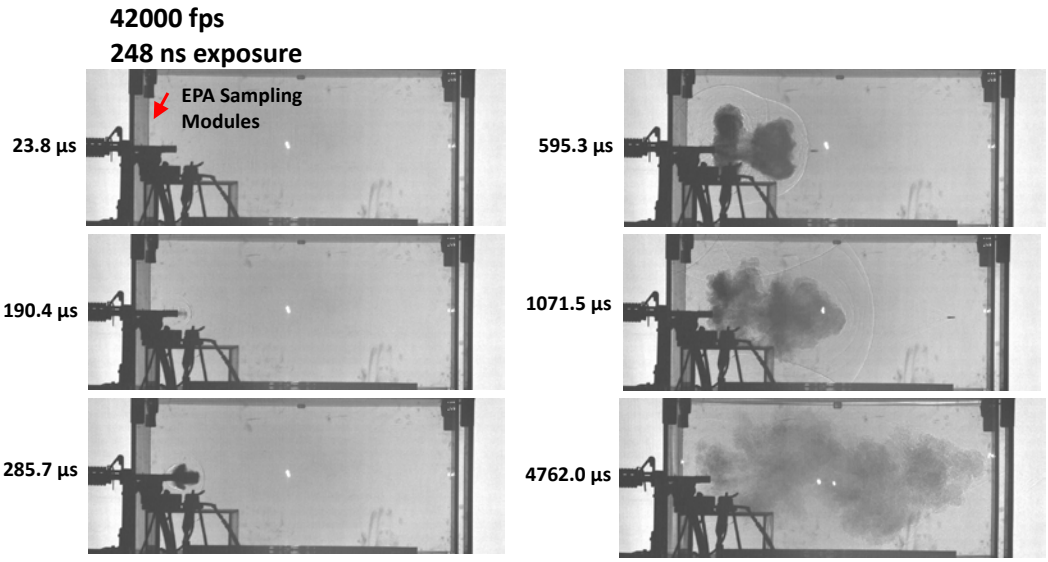

Fig. 7 A series of Edgerton shadowgraph images (times shown are time after initiation of trigger mechanism), measured through the PMMA enclosure, during emissions testing of the M4 weapon firing salted M855 ammunition. The images are part of an image sequence captured at 42,000 fps using an exposure time of 248 ns. Illumination was by arc lamp, camera was a Photron Camera Model SA-z monochrome.

2.3.4 Cleaning of Test Chamber/Box Walls

The test chamber enclosure was made up of PMMA. The PMMA was cleaned between firings with a glass cleaner to obtain clear photographs. This glass cleaner contained the VOCs shown in Table 5.

Table 5 Glass cleaner ingredients (SC Johnson 2017)

Glass cleaner ingredients	
2-hexaoxyehtanol	C9-11 pareth-3
Isopropanolamine	Citronellol
Lauryl dimenthyl amine oxide	Citrus aurantium dulcis peel oil
Sodium dodecylbenzene sulfonate	Dirpopylene glycol
Benzyl acetate	Ethoxydiglycol
Butylphenyl methylpropional	Hexyl cinnamal
Linlool	Terpineol

2.4 Results of Simulations

The simulations used to predict gas and particle emissions from firing of the M4 carbine are based upon a sequence of steps that make up the firing process. When the trigger in the weapon is actuated, a primer adjacent to the propellant within the shell casing is initiated by the firing pin in the weapon. The propellant is ignited by hot gases and particles from the primer, and burns. The burning propellant gases

expand and accelerate a projectile within the gun barrel. The projectile exits the gun barrel at the muzzle, followed by the high-pressure and high-temperature gases and particles. The gases and particles mix with air, and combustion occurs (often incomplete), often producing a muzzle flash and determining the final emission products of the event.

The US Army Research Laboratory (ARL) maintains a suite of gun IB models that range from a lumped-parameter (i.e., well-stirred mixture) representation to 1-D/2-phase and 2-D/2-phase models that utilize computational fluid dynamics (CFD) techniques applicable to multi-phase flow (Horst and Nusca 2006). These models have been successfully applied to weapons of the class used in the present study (i.e., 5.56-mm M855 small-caliber ammunition IB) (Schmidt and Nusca 2009; Nusca 2011). Although some of these IB models have the capability to simulate chemically reacting gas-phase flows (using a well-defined set of chemical kinetics based on Arrhenius reaction rates), this degree of modeling is rarely used when seeking to obtain IB gun chamber pressures, gun tube wave dynamics, and projectile muzzle velocity. Rather, heat-release kinetics is regularly used in these IB models (Nusca 2011). In addition, these IB models do not extend into the "transitional" ballistics domain (i.e., exterior to the gun tube) and thus do not model muzzle gas efflux and blast. The requirements of the present project precipitated the use of an evolving new capability that extends the application of the ARL's 2-D/two-phase IB model into the muzzle environment so that modeling of the blast can naturally follow a simulation that is started with the primer function and proceeds through the events leading to expulsion of the round from the gun (Nusca et al. 2016).

For the present simulations, it is assumed that the propellant used in the M855 ammunition produces (anaerobically) combustion product gases as listed in Table 6 (the mixture molecular weight is 33.8 g/g-mole). These results were generated using the Constant Breech Pressure (CBP) model, which is a very good approximation for optimized fielded guns and gives the equilibrium composition of gases at muzzle (Kotlar 1992) (given the proper species database). The CBP gun calculation is the idealized limiting case of IB, that is, in the CBP gun the chemistry is at equilibrium and the propellant burns at optimum conditions for a given breech pressure. This method is a complete thermochemical state description of the ballistic cycle, the output of which is projectile velocity and equilibrium chemical composition at the muzzle of the gun, modified in-house (ARL) to include variable amounts of condensed carbon (soot). This modification is an alternative to the standard CHEETAH gun calculation performed on the propellant tested here, which predicts no condensed phase products. The formation of soot in the gun propellant products allows a higher concentration of CO_2 relative to CO than that

predicted by CHEETAH. In the interest of completeness, the results of a standard CHEETAH run on the M855 propellant (SMP 842) is shown in Appendix A. Although possible given an appropriate chemical kinetics (CHEMKIN) set for the propellant, it was outside the scope of the present effort to model chemical reactions for the gas-phase species in the muzzle blast flow (although see Appendix B for input data necessary to accomplish this). Rather, the assumption of "frozen chemistry" was used so that the gas species expelled from the gun muzzle at the time of shot exit (about 1.13 ms from gun primer ignition) are then distributed through and mixed with the near field air solely by mean of convection and diffusion.

Table 6 Computed species and mole fractions for muzzle exit efflux, approximately 1.13 ms after primer function. These gas species are mixed with air and combust, producing final products.

Specie	O_2	N_2	H_2	H_2O	CO	CO_2	CH_4	C_2H_6	NH_3
Mole fraction	0.0	0.15749	0.00181	0.07039	0.00143	0.56354	0.20488	0.00008	0.00017

Note: C_2H_6 = ethane and NH_3 = ammonia

The details of the modeling are discussed later in this section, but the end results are shown in Fig. 8 and Table 7. Figure 8 shows the computed time-dependent species mole fraction histories for about 40 ms following gun primer function (the bullet exits the gun muzzle at 1.13 ms) at a specific location in the near-field gun flow-field termed the "probe location". This location is 15 cm below the gun tube centerline and in-line with the gun muzzle. It closely approximates the actual location of the instruments used in the gas and particle measurements without extending the computational domain to a breadth that would make the timely execution of the model prohibitive.

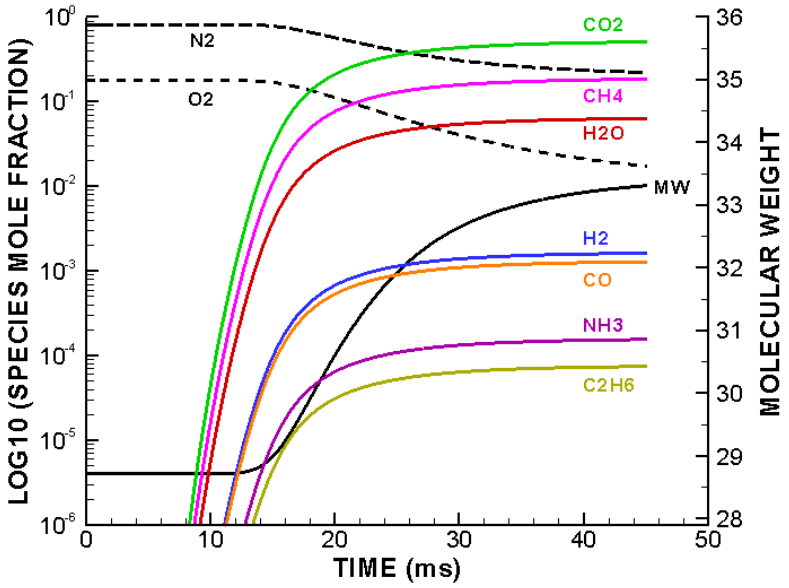

Fig. 8 Computed time history mole fractions and mixture molecular weight up to 40 ms for muzzle gas species at the probe location

Table 7 Computed species and mole fractions at probe location for 142 ms after primer function

Specie	O_2	N_2	H_2	H_2O	CO	CO_2	CH_4	C_2H_6	NH_3
Mole fraction	0.18590	0.00768	0.00173	0.06739	0.00137	0.53952	0.19616	0.00008	0.00017

As the initial environment outside the gun tube is air (at standard pressure and temperature), the sole gas species for about 8 ms (the time it takes for the chemical cloud to reach the probe) are oxygen (O_2) and N_2. Driven by the muzzle blast (shock waves) and modeled using convection and diffusion, the other species eventually reach the probe location. Table 7 lists the species mole fractions at about 142 ms after primer function when the mixture molecular weight is 34.3 g/g-mole.

Figure 9 shows the computational domain for the 5.56-mm ammunition (M855) and M4 gun barrel to include 34 cm in front of the muzzle (the gun tube is 46 cm long) and 30 cm around the gun barrel (referenced to the barrel centerline)—the domain shown in the figure is not plotted to scale (it is stretched in the lateral direction for clarity); as a result, the true curvature of the shock waves is not represented. The boundary conditions prescribed on the edges of the domain are outflow with proper characteristic treatment so the extent of the domain around the gun barrel, which is user-extendable, should not affect the results. The 5.56-mm-diameter bullet (not shown in these views since shot exit is approximately 1.13 ms after primer function) is modeled as a right-cylinder for simplicity and is assumed

to fit perfectly into the gun tube; typical blow-by of gun gases is not considered. The plotted color contours are gas pressure (blue to red: low to high), which are used to highlight the muzzle shock waves (and thus ignore the projectile bow shock). High-pressure gas (250 psia and above) is evident within the gun barrel for which details of the internal flow-field are obscured and low pressures are green-yellow-light blue colors so that relatively low-pressure details as in the projectile bow shock are obscured as well. To highlight details of the muzzle flow, the selected pressure contour level range cannot simultaneously show details for both internal and external regions of the gun barrel. Peak efflux from the gun muzzle occurs at about 15 ms after primer ignition (note the two barrel shocks that end in a normal shock near the gun muzzle in Fig. 10). By 30 ms after primer function, the gun tube "blow-down" event is occurring (note the presence of a rarefaction shock traveling into the gun barrel at 30 ms after primer function in Fig. 11). Similar results and a more detailed description are available (Nusca et al. 2016).

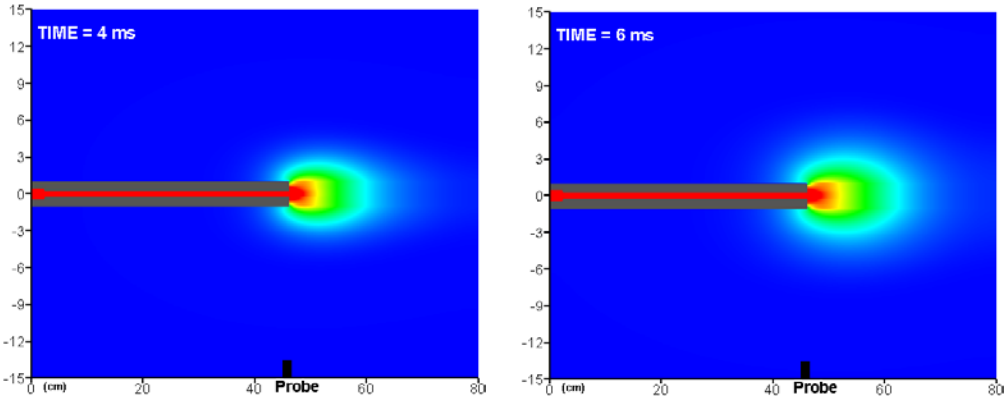

Fig. 9 Computed color pressure contours (blue to red: 0 to 250 psia) for 5.56-mm (M855) ammunition and M4 gun barrel: 4 and 6 ms after primer ignition (bullet exit at 1.13 ms)

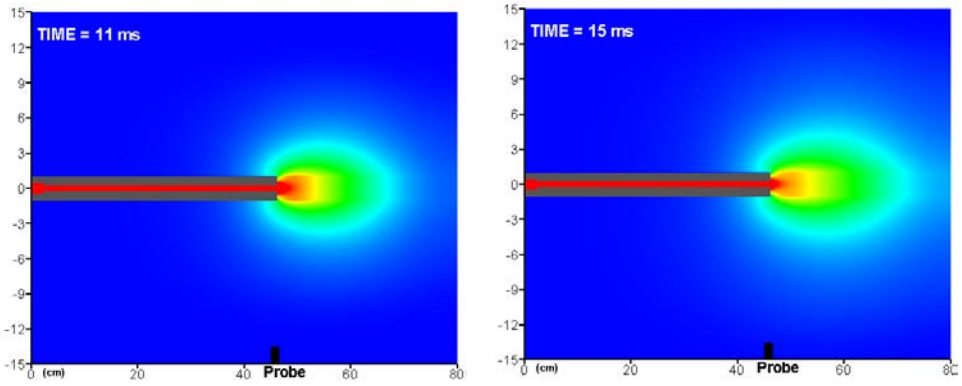

Fig. 10 Computed color pressure contours (blue to red: 0 to 250 psia) for 5.56-mm (M855) ammunition and M4 gun barrel: 11 and 15 ms after primer ignition (bullet muzzle exit at 1.13 ms)

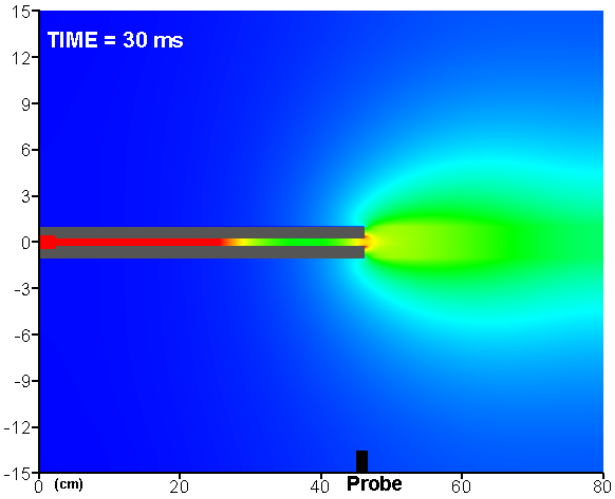

Fig. 11 Computed color pressure contours (blue to red: 0 to 250 psia) for 5.56-mm (M855) ammunition and M4 gun barrel: 30 ms after primer ignition (bullet muzzle exit at 1.13 ms)

Figure 12 shows the computed color (banded for clarity) mole fraction contours for CO_2 throughout the near-field of the gun tube and correspond to the times of the pressure contour plots of Fig. 7. The highest concentration of CO_2 is evident near the gun tube muzzle where the pressure is also the highest and the gas velocity is subsonic.

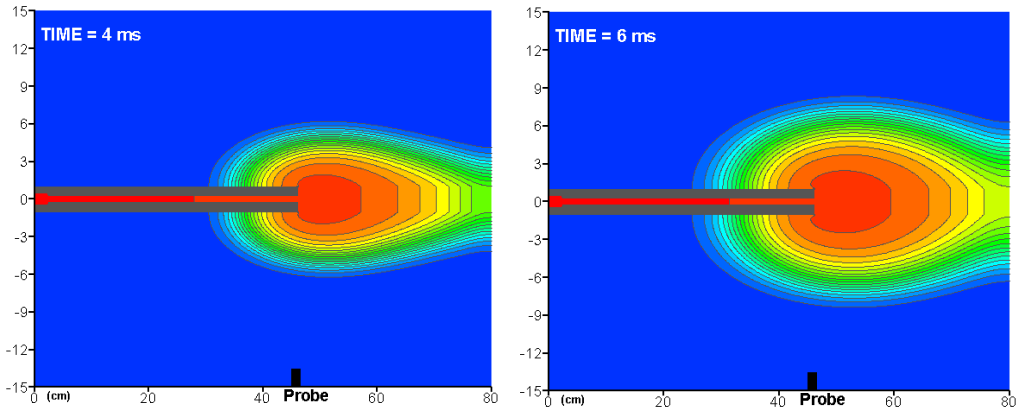

Fig. 12 Computed color (banded) mole fraction contours of CO_2 (blue to red: 0 to 0.6) for 5.56-mm (M855) ammunition and M4 gun barrel: 4 and 6 ms after primer ignition (bullet muzzle exit at 1.13 ms)

By 30 ms after primer ignition (Figs. 13 and 14), the highest concentration of CO_2 should be measured at the probe location since for subsequent times the gun tube flow is reducing due to blow down (recall Fig. 11). This corresponds to the results shown in Fig. 8. The time-dependent behavior of other gas species is similar to that of CO_2.

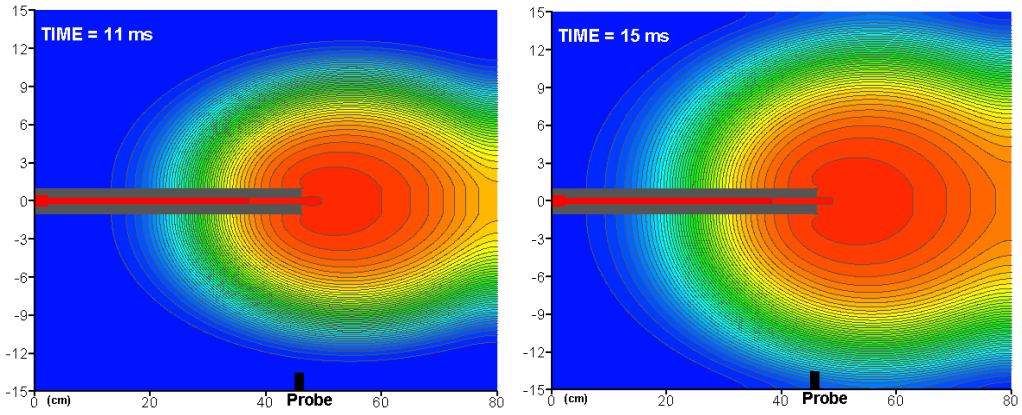

Fig. 13 Computed color (banded) mole fraction contours of CO_2 (blue to red: 0 to 0.6) for 5.56-mm (M855) ammunition and M4 gun barrel: 11 and 15 ms after primer ignition (bullet muzzle exit at 1.13 ms)

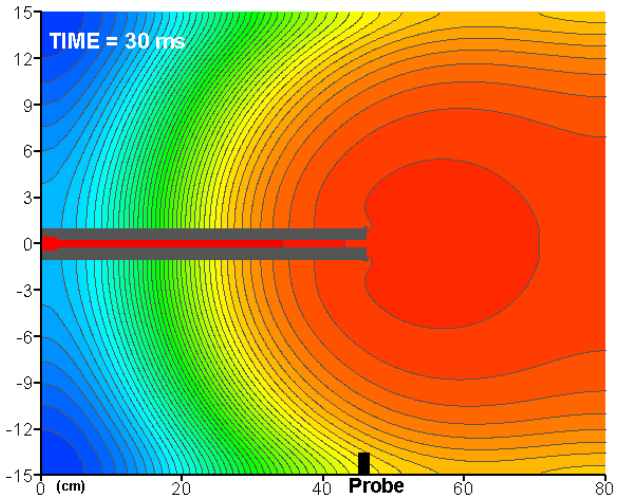

Fig. 14 Computed color (banded) mole fraction contours of CO_2 (blue to red: 0 to 0.6) for 5.56-mm (M855) ammunition and M4 gun barrel: 30 ms after primer ignition (bullet muzzle exit at 1.13 ms)

Calculated EFs for the simulation employing the NASA-Lewis equilibrium thermochemical code are shown in Table 8. MCEs for both simulation methods are shown in Table 9. Output of a CHEETAH gun run for the propellant in the M855 round is shown in Appendix A.

Table 8 Calculated EFs for firing of a single round of M855 ammunition (unsalted, SMP-842, gram of emitted species per gram propellant)

Species	NASA-Lewis
CO	0.0075
N_2	0.101
CO_2	0.465
H_2O	0.024
CH_4	0.0615
H_2	trace

Table 9 MCE for firing of M855 ammunition

Simulation	MCE
NASA-Lewis simulation with soot formation M855	0.732
CHEETAH/CHEMKIN gun calculation M855	0.998

2.5 Results of Experiments: M4 Carbine Emission Factors

2.5.1 CO_2, CO, and CH_4

Major gaseous carbon species are listed in Table 10. Significant levels of incomplete CO oxidation resulted in MCE values less than or equal to 0.5. CH_4 was detected at trace levels. Shot to shot variation was minor as seen by low RSD and RPD values. Slightly less CO oxidation is observed with the M855 salted ammunition than with unsalted rounds, although within experimental error the MCE for each type of round are the same. The legacy rounds exhibited less complete CO oxidation than the M855 salted or M855 unsalted rounds.

Table 10 CO_2, and CO EFs as well as MCE

Compound	855 salted				855 unsalted				Legacy			
		Average	Stand. dev.	RSD[b]		Average	Stand. dev.	RSD[b]		Average	Stand. dev.	RSD[b]
	n[a]	g/kg fuel	g/kg fuel	%	n[a]	g/kg fuel	g/kg fuel	%	n[a]	g/kg fuel	g/kg fuel	%
CO_2	5	284	44	15	4	300	55	18	1	253	56	22
CO	5	191	17	8.9	4	192	19	9.8	1	208	30	14
…	…	Average fraction	Stand. dev. fraction	…	…	Average fraction	Stand. dev. fraction	…	…	Fraction	Stand. dev. fraction	…
MCE[d]	5	0.49	0.056	19	4	0.5	0.064	22	1	0.44	0.080	24

[a] Number of samples collected.
[b] Calculated when n = 3 or more.
[c] Calculated when n = 2. MCE = $(\Delta CO_2/(\Delta CO_2+\Delta CO+\Delta CH_4)$

2.5.2 Particulate Matter (PM)

The near equivalence of $PM_{2.5}$ results with PM_{10} results indicate that the majority of the emitted particles are of diameter less than or equal to 2.5 µm (Table 11 and Figs. 15 and 16). This is consistent with the sampling chamber work of Wingfors et al. (2014) who found the aerodynamic size increasing from 0.2 µm at 2 min after firing to 1 µm after 12 min, the increase in size due to particle agglomeration. The PM EFs for the two different ammunition compositions (855 salted vs. 855 unsalted and legacy) are statistically distinct ($p < 0.004$, $F > 3.8$). The RSD and RPD are low for these rounds indicating consistency in the emissions as well as the testing and sampling method. The EFs for PM_{10} are consistent with those measured by Wingfors et al. (2014) for total suspended particles (0.029–0.030 g/round), albeit using different methods and different ammunition types.

Table 11 PM EFs from firing of the M4 carbine. Grams per kilogram of fuel is used because the ammunition includes both propellant and primer.

PM size	Bullet type	n[a]	Average g/kg fuel	Stand. dev. g/kg fuel	Average g/round	Stand. dev. g/round	RSD[b] %	RPD[c] %
$PM_{2.5}$	M855 salt	3	23	2.3	0.040	0.0040	10.0	…
PM_{10}	M855 salt	3	34	5.3	0.059	0.0091	15.5	…
$PM_{2.5}$	M855	2	15	…	0.025	…	…	15.7
PM_{10}	M855	2	17	…	0.029	…	…	5.4
$PM_{2.5}$	Legacy	2	10	…	0.017	…	…	38
PM_{10}	Legacy	2	11	…	0.020	…	…	21

[a] Number of samples collected.
[b] Calculated when n = 3 or more.
[c] Calculated when n = 2.

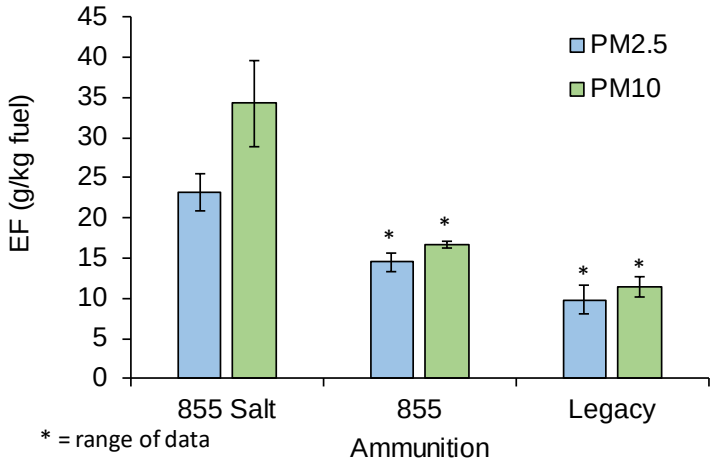

Fig. 15 PM EFs from the M4 carbine in grams per kilograms of fuel. Error bars represent one standard deviation if nothing else stated.

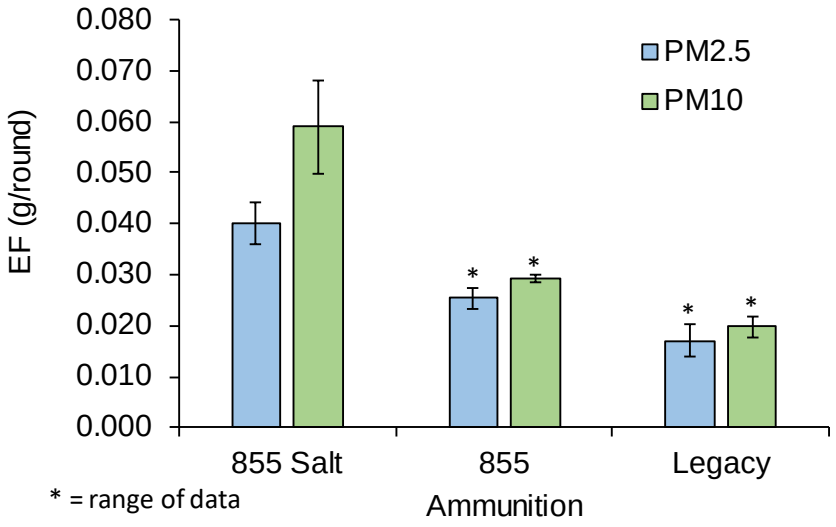

Fig. 16 PM EFs from the M4 carbine in grams per round. Error bars represent one standard deviation if nothing else stated.

2.5.3 Elements

Elemental emissions are found in recovered particles. Element emissions are shown in Tables 12, 13, and 14. All three ammunition types show relatively similar metal EFs (see Figs. 3–5) with the exception of K from the salted (KNO_3) ammunition.

Table 12 Element EFs from the M4 carbine, M855 salted ammunition

	M855 salted							
	$PM_{2.5}$				PM_{10}			
Element	n[a]	Average g/kg fuel	Stand. dev. g/kg fuel	RSD %	n[a]	Average g/kg fuel	Stand. dev. g/kg fuel	RSD %
Mg	3	0.28	0.019	6.5	3	0.40	0.11	26
Al[c]	3	0.072	0.028	39	3	0.15	0.05	34
S	3	0.76	0.20	26	3	0.49	0.17	34
K	3	9.07	0.69	7.6	3	9.94	1.74	17
Fe	3	0.17	0.021	12	3	0.27	0.06	24
Cu	3	16.39	1.01	6.2	3	26.35	4.18	16
Zn	3	2.12	0.14	6.8	3	3.02	0.47	16
Bi	3	2.91	0.60	21	3	4.28	1.24	29
Pb	3	5.77	0.42	7.3	3	7.61	0.89	12
Ba	3	0.31	0.039	13	3	0.47	0.11	24
Sb	3	1.56	0.22	14	3	2.17	0.52	24
V	3	0.017	0.002	11	3	0.025	0.007	29
Cl	0	ND[b]	…	…	0	ND[b]	…	…

[a] Number of samples collected.
[b] ND = not detected.
[c] Al values less than 3 times the uncertainty of the analytical method.

Table 12 Element EF from the M4 carbine, M855 salted ammunition (continued)

Element	M855 salted PM2.5 n[a]	Average g/kg fuel	Stand. dev. g/kg fuel	RSD %	PM10 n[a]	Average g/kg fuel	Stand. dev. g/kg fuel	RSD %
Mg	3	0.49	0.03	…	3	0.70	0.18	…
Al[c]	3	0.12	0.05	…	3	0.25	0.08	…
S	3	1.31	0.34	…	3	0.85	0.29	…
K	3	15.65	1.19	…	3	17.15	3.00	…
Fe	3	0.30	0.04	…	3	0.46	0.11	…
Cu	3	28.29	1.75	…	3	45.47	7.21	…
Zn	3	3.66	0.25	…	3	5.22	0.81	…
Bi	3	5.02	1.04	…	3	7.39	2.13	…
Pb	3	9.96	0.73	…	3	13.14	1.54	…
Ba	3	0.53	0.07	…	3	0.80	0.20	…
Sb	3	2.69	0.37	…	3	3.74	0.90	…
V	3	0.029	0.003	…	3	0.043	0.013	…
Cl	0	ND[b]	…	…	0	ND[b]	…	…
		Average g/kg element[d]	**Stand. dev. g/kg element[d]**			**Average g/kg element[d]**	**Stand. dev. g/kg element[d]**	
Al[c]	3	50.6	19.5	…	3	102.9	34.7	…
S	3	883.7	232.0	…	3	573.6	197.3	…
Pb	3	1672.2	122.6	…	3	2204.6	259.2	…
Ba	3	89.8	11.5	…	3	136.8	33.3	…
Sb	3	715.9	99.0	…	3	993.6	239.7	…
Bi	3	1484.5	306.9	…	3	2184.9	630.3	…

[a] Number of samples collected.
[b] ND = not detected.
[c] Al values less than 3 times the uncertainty of the analytical method.
[d] Element (Al, S, Pb, Ba, Bi, or Sb) in the ammunition.

Table 13 Element EFs from the M4 carbine, M855 ammunition

Element	M855 PM2.5 n[a]	Average g/kg fuel	RPD %	PM10 n[a]	Average g/kg fuel	RPD %
Mg	2	0.22	29	2	0.19	6.4
Al	2	0.086	0.96	2	0.093	21
S[b]	1	0.0005		0	ND	
K	2	0.570	103	2	0.45	91
Fe	2	0.15	4.4	2	0.15	13
Cu	2	15.61	11	2	18.14	10
Zn	2	2.04	11	2	2.09	14
Bi	2	2.85	33	2	2.93	5.6
Pb	2	6.07	7.3	2	5.77	29
Ba	2	0.33	4.7	2	0.33	14

[a] Number of samples collected.
[b] Values less than 3 times the uncertainty of the analytical method.

Table 13 Element EFs from the M4 carbine, M855 ammunition (continued)

	M855					
	$PM_{2.5}$			PM_{10}		
Element	**n[a]**	**Average g/kg fuel**	**RPD[b] %**	**n[a]**	**Average g/kg fuel**	**RPD[b] %**
Sb	2	1.55	5.4	2	1.47	17
V	2	0.086	9.6	2	0.020	5.6
Cl	0	ND[c]		0	ND[c]	
	n[a]	**Average mg/round**		**n[a]**	**Average mg/round**	
Mg	2	0.39	…	2	0.34	…
Al	2	0.15	…	2	0.16	…
S[b]	1	0.00082	…	0	ND[c]	…
K	2	1.00	…	2	0.78	…
Fe	2	0.26	…	2	0.27	…
Cu	2	27.25	…	2	31.67	…
Zn	2	3.55	…	2	3.64	…
Bi	2	4.98	…	2	5.12	…
Pb	2	10.60	…	2	10.07	…
Ba	2	0.57	…	2	0.57	…
Sb	2	2.70	…	2	2.57	…
V	2	0.15	…	2	0.034	…
Cl	0	ND[c]	…	0	ND[c]	…
	n[a]	**Average g/kg element[c]**		**n[a]**	**Average g/kg element[c]**	
Al[b]	2	85.4	…	2	92.5	…
S[b]	1	0.55	…	0	ND[c]	…
Pb	2	1765.2	…	2	1484.6	…
Ba	2	440.9	…	2	1676.4	…
Sb	2	333.6	…	2	441.9	…
Bi	2	1444.6	…	2	317.4	…

[a] Number of samples collected.
[b] Values less than 3 times the uncertainty of the analytical method.
[c] Element (Al, S, Pb, Ba, Bi, or Sb) in the ammunition.

Table 14 Element EFs from the M4 carbine, legacy ammunition

	Legacy					
	$PM_{2.5}$			PM_{10}		
Element	**n[a]**	**Average g/kg fuel**	**RPD[b] %**	**n[a]**	**Average g/kg fuel**	**RPD[b] %**
Mg	2	0.17	32	2	0.13	24
Al	2	0.077	35	2	0.073	26
S	0	n/c[d]	…	0	n/c[d]	…
K	2	0.099	2.3	2	0.090	2.6
Fe	2	0.50	37	2	0.48	37
Cu	2	12.14	28	2	13.71	29
Zn	2	1.76	29	2	1.80	31
Bi	2	0.074	119	2	0.073	115
Pb	2	4.95	20	2	4.69	26
Ba	2	0.28	28	2	0.28	34
Sb	2	1.30	31	2	1.25	33
V	2	0.014	15	2	0.016	32
Cl	2	0.082	87	2	0.042	58
	n[a]	**Average mg/round**		**n[a]**	**Average mg/round**	
Mg	2	0.29	…	2	0.22	…
Al	2	0.13	…	2	0.13	…
S	0	n/c[e]	…	0	n/c[e]	…
K	2	0.17	…	2	0.16	…
Fe	2	0.87	…	2	0.83	…
Cu	2	21.05	…	2	23.77	…
Zn	2	3.05	…	2	3.12	…
Bi	2	0.13	…	2	0.13	…
Pb	2	8.58	…	2	8.13	…
Ba	2	0.48	…	2	0.49	…
Sb	2	2.25	…	2	2.17	…
V	2	0.025	…	2	0.027	…
Cl	2	0.14	…	2	0.073	…
	n[a]	**Average g/kg element[b]**		**n[a]**	**Average g/kg element[b]**	
Al	2	75.9	…	2	72.6	…
S	0	n/c[c]	…	0	n/c[c]	…
Pb	2	1437.7	…	2	1363.7	…
Ba	2	372.2	…	2	378.3	…
Sb	2	280.2	…	2	270.1	…
Bi	2	37.5	…	2	37.0	…

[a] Number of samples collected with detectable levels.
[b] metal (Al, S, Pb, Ba, Bi, or Sb) in the full round.
[c] not collected.

Metals Pb and bismuth (Bi) (except for legacy rounds) result in higher emissions than were present in the initial bullet composition (Fig. 18). This suggests some compositional discrepancies or the presence of residual contamination of the M4 from previous firings.

Cu exhibits the highest metal EF we observed in for the gun firings although there is no Cu in the propellants and primers of the three tested bullets. Rather, the bullets (slug) are encased in a Cu jacket, which is etched by the rifled barrel to enable the bullet to spin, aiding in accuracy. As the barrel etches the Cu jacket, Cu is deposited on the barrel interior and, as these results show, emitted from the barrel. In addition, a de-coppering agent (Bi) is added to the propellant to keep the rifle barrel clean. Other elements are also observed in the PM but are not reported in the propellant and primer formulation including sodium (Na), iron (Fe), zinc (Zn), and K (in the unsalted rounds). It is possible that these elements are alloyed in low amounts in the bullet (slug) casing.

Element emission factors from $PM_{2.5}$ and PM_{10} are quite similar between round types (Fig. 17) indicating that the majority of particles are of 2.5-µm median diameter or less, as stated previously. The metals within the three round types have similar EFs (Fig. 18). The legacy ammunition showed detectable levels of chlorine (Cl) while the 855 ammunition showed no detectable levels of Cl. Rather, the M855 unsalted ammunition showed detectable levels of S, unlike the legacy ammunition. There is limited overlap in reported metals by Wingfors et al. (2014). Their Cu, Pb, and Zn values were 11.4, less than 7.3, and 3.7 mg/round, respectively, which compare with our average values (Tables 12, 13, and 14) of 25.5, 3.4, and 9.7 mg/round. Their Pb values are much lower than measured in this work, consistent with their use of Pb-free rounds.

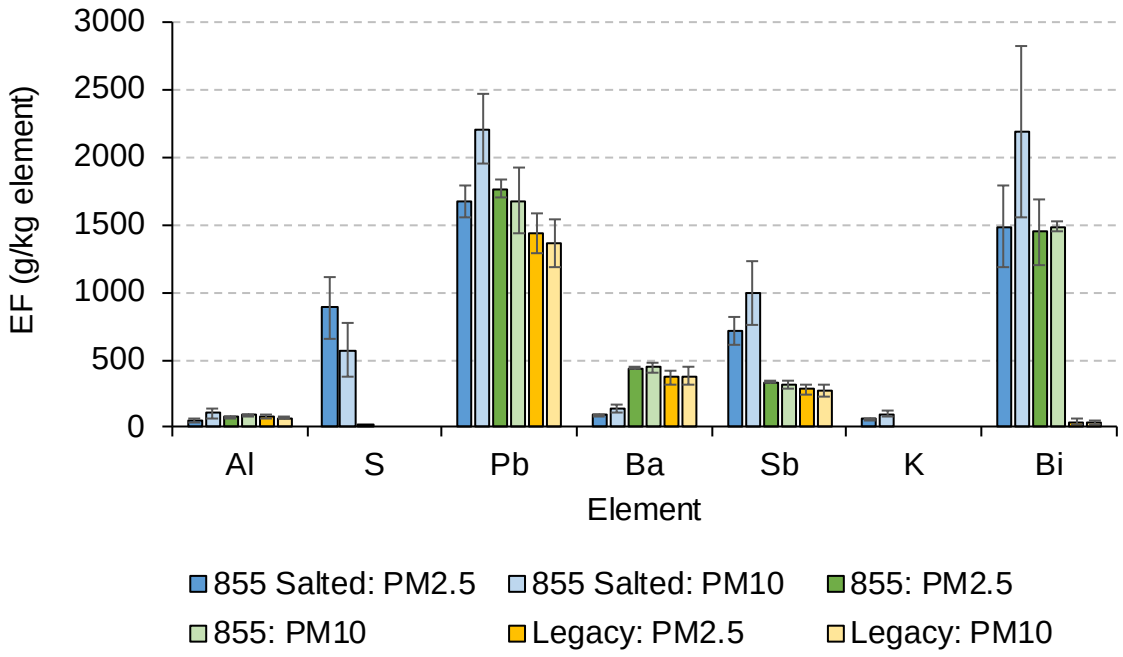

Fig. 17 Element EFs in gram per kilogram of element in $PM_{2.5}$ and PM_{10} fractions from firing of the M4 carbine

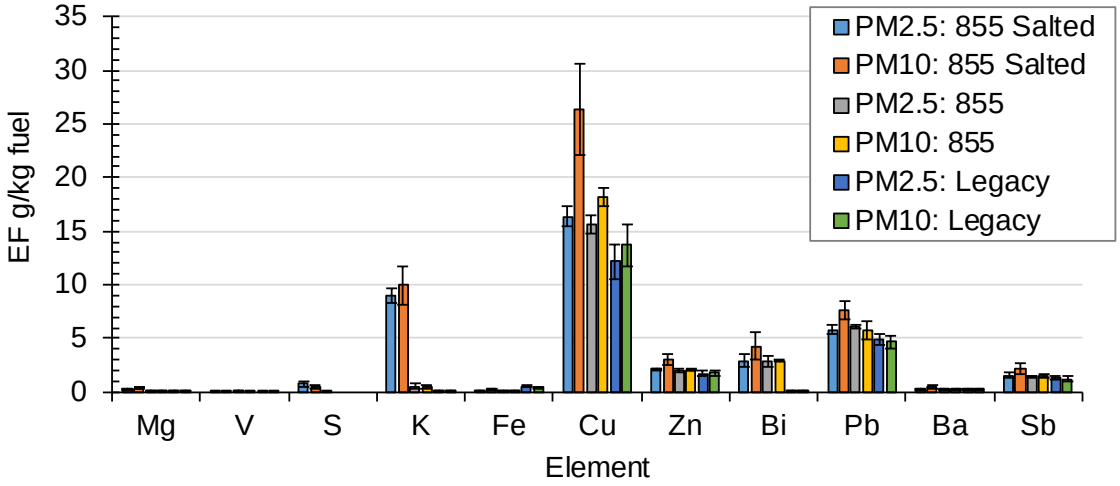

Fig. 18 Element EFs from three different ammunition types fired in the M4 carbine

2.5.4 VOCs

VOC data from the three bullet types are shown in Tables 15 and 16. The sole overlap with data from Wingfors et al. (2014) is acrolein for which they obtained 8 ±1 µg/round as compared to this work at a six-bullet average, 3.8 µg/round. Some of these VOCs may originate from the acrylic glass (PMMA) cracking from the shockwave, such as methyl methacrylate, which showed high levels after the first round (M855 salted): 40 mg/kg fuel compared to less than 5 mg/kg fuel for the rest

of the rounds (Fig. 19). Methylene chloride and trichloroethene followed the same methyl methacrylate level pattern trend, suggesting that these emissions relate to the PMMA cracking as well. Isopropyl alcohol (2-propanol) showed also a pattern with test order (Fig. 20), although it followed the cleaning of the PMMA box, suggesting that it relates to the glass cleaner that contained isopropanolamine. We have no explanation for the spike in methylene chloride (MeCl) levels for the initial test.

Table 15 VOC EFs from firing of the M4 carbine

	M855			M855 salted					Legacy	
	n[b]	Average	RPD	n[b]	Average	Stand. dev.	RSD	RPD	n[b]	
		mg/kg	%		mg/kg	mg/kg	%	%		mg/kg
Propene	2	16.19	5.5	3	13.6	5.17	38	…	1	16.19
1,3-butadiene[a]	2	3.70	8.4	2	3.33	…	…	43	1	2.35
Ethanol	2	3.03	24	2	3.67	…	…	4.8	1	2.67
Acetonitrile	2	86.79	0.07	3	60.0	19.00	32	…	1	93.86
Acrolein[a]	2	1.22	12	3	2.90	0.59	20	…	1	2.06
Acetone	2	0.57	54	1	1.70	…	…	…	0	ND
Trichlorofluoromethane	2	0.76	57	2	0.62	…	…	33	1	0.26
2-Propanol	2	2.10	99	2	6.08	…	…	145	1	4.22
Acrylonitrile[a]	2	9.52	2.5	3	6.71	2.29	34	…	1	12.44
MeCl[a]	2	180.36	51	1	1201	…	…	…	1	13.82
Carbon disulfide[a]	2	0.57	48	2	1.92	…	…	178	1	0.16
2-butanone (MEK) [a]	2	0.62	12	2	0.39	…	…	26	1	0.47
Ethyl acetate	2	4.08	4.9	2	4.28	…	…	16	1	6.80
n-hexane	2	0.08	12	1	0.16	…	…	…	0	ND
Benzene[a]	2	100.33	1.7	3	93.8	27.01	29	…	1	119.58
Carbon tetrachloride[a]	2	0.01	12	1	0.01			…	0	ND
Trichloroethene	2	9.00	57	3	34.2	52.93	155	…	1	1.01
Methyl methacrylate[a]	2	2.17	61	3	13.8	22.61	164	…	1	0.23
n-heptane	2	0.10	12	0	ND			…	0	ND
Toluene[a]	2	7.24	17	3	6.64	2.20	33	…	1	7.67
2-hexanone	2	0.11	12	0	ND	…	…	…	0	ND
n-butyl acetate	0	ND		1	3.05	…	…	…	0	ND
Tetrachloroethene	2	0.24	105	0	ND	…	…	…	0	ND
Ethylbenzene	2	0.44	12	2	0.41	0.11	27	38	1	0.31
m,p-xylenes[a]	2	0.70	17	2	0.69	0.21	30	42	1	0.45
Styrene[a]	2	0.47	17	2	0.84	0.41	49	70	0	ND
o-xylene[a]	2	0.29	15	2	0.29	0.078	27	38	1	0.21
Alpha-pinene	2	1.06	18	2	1.21	…	…	100	1	0.17
1,2,4-trimethylbenzene	2	0.11	27	0	ND	…	…		0	ND
d-limonene	2	1.17	24	2	1.40	…	…	130	1	0.16
Propene	2	28.27	5.5	3	23.49	8.93	38	…	1	28.07
1,3-butadiene[a]	2	6.46	8.4	2	5.74	…	…	43	1	4.07
Ethanol	2	5.30	24	2	6.34	…	…	4.8	1	4.64

[a] On EPA's list of hazardous air pollutants.
[b] Number of samples with detectable levels.

Table 16 VOC EFs from firing of the M4 carbine in per round

	M855			M855 salted					Legacy	
	n[b]	Average µg/round	RPD %	n[b]	Average µg/round	Stand. dev. µg/round	RSD %	RPD %	n[b]	µg/round
Acetonitrile	2	151.53	0.07	3	103.63	32.80	32	…	1	162.75
Acrolein[a]	2	2.13	12	3	5.00	1.02	20	…	1	3.57
Acetone	2	1.00	54	1	2.93	…	…	…	0	ND
Trichlorofluoromethane	2	1.33	57	2	1.08	…	…	33	1	0.45
2-propanol	2	3.67	99	2	10.49	…	…	145	1	7.32
Acrylonitrile[a]	2	16.63	2.5	3	11.59	3.95	34	…	1	21.56
MeCl[a]	2	314.92	51	1	2072.98	…	…	…	1	23.96
Carbon disulfide[a]	2	1.00	48	2	3.32	…	…	178	1	0.28
2-butanone (MEK) [a]	2	1.09	12	2	0.67	…	…	26	1	0.82
Ethyl acetate	2	7.12	4.9	2	7.39	…	…	16	1	11.80
n-Hexane	2	0.13	12	1	0.28	…	…	…	0	ND
Benzene[a]	2	175.17	1.7	3	161.95	46.62	29	…	1	207.36
Carbon tetrachloride[a]	2	0.024	12	1	0.02			…	0	ND
Trichloroethene	2	15.72	57	3	59.11	91.36	155	…	1	1.75
Methyl methacrylate[a]	2	3.78	61	3	23.75	39.02	164	…	1	0.41
n-heptane	2	0.17	12	0	ND			…	0	ND
Toluene[a]	2	12.65	17	3	11.45	3.80	33	…	1	13.30
2-hexanone	2	0.20	12	0	ND	…	…	…	0	ND
n-Butyl acetate	0	ND	…	1	5.27	…	…	…	0	ND
Tetrachloroethene	2	0.41	105	0	ND	…	…	…	0	ND
Ethylbenzene	2	0.78	12	2	0.71	0.19	27	38	1	0.53
m,p-xylenes[a]	2	1.22	17	2	1.19	0.36	30	42	1	0.77
Styrene[a]	2	0.83	17	2	1.44	0.71	49	70	0	ND
o-xylene[a]	2	0.51	15	2	0.50	0.13	27	38	1	0.36
alpha-pinene	2	1.85	18	2	2.09	…	…	100	1	0.30
1,2,4-trimethylbenzene	2	0.19	27	0	ND	…	…	…	0	ND
d-limonene	2	2.03	24	2	2.41	…	…	130	1	0.27

[a] On EPA's list of hazardous air pollutants.
[b] number of samples with detectable levels.

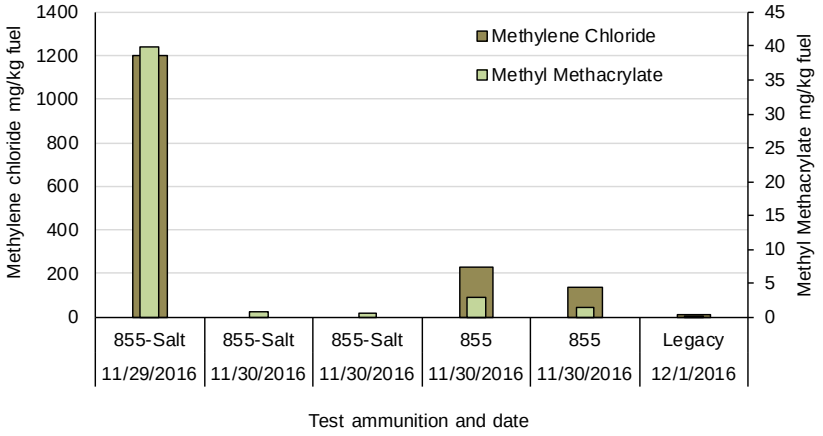

Fig. 19 EFs of methylene methacrylate and MeCl in order of the testing

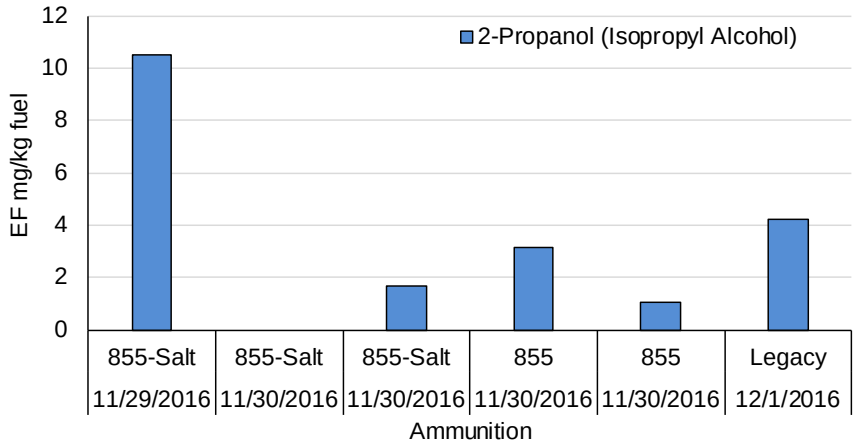

Fig. 20 EFs of 2-propanol (isopropyl alcohol) in order of the testing

2.5.5 Energetics

None of the target nitroaromatics were above the instrument detection limit and so are reported at the method detection limit (MDL) (Tables 17 and 18).

Table 17 Energetics MDLs in milligrams per kilograms of fuel

MDLs	855 salt	855	Legacy
	MDL mg/kg fuel	MDL mg/round	MDL mg/round
1,3,5-trinitrobenzene	<22.4	<19.8	<15.2
1,3-dinitrobenzene	<22.4	<19.8	<15.2
2,4,6-trinitrotoluene	<22.4	<19.8	<15.2
2,4-dinitrotoluene	<22.4	<19.8	<15.2
2,6-dinitrotoluene	<22.4	<19.8	<15.2
2-amino-4,6-dinitrotoluene	<22.4	<19.8	<15.2
2-nitrotoluene	<22.4	<19.8	<15.2
3,5-DNA	<22.4	<19.8	<15.2
3-nitrotoluene	<22.4	<19.8	<15.2
4-amino-2,6-dinitrotoluene	<22.4	<19.8	<15.2
4-nitrotoluene	<22.4	<19.8	<15.2
HMX	<22.4	<19.8	<15.2
Nitrobenzene	<22.4	<19.8	<15.2
Nitroglycerine	<22.4	<19.8	<15.2
PETN	<55.9	<49.4	<38.0
RDX	<22.4	<19.8	<15.2
Tetryl	<22.4	<19.8	<15.2

Table 18 Energetics MDLs in milligrams per round

MDLs	M855 salted MDL mg/round	M855 MDL mg/round	Legacy MDL mg/round
1,3,5-trinitrobenzene	<0.039	<0.034	<0.026
1,3-dinitrobenzene	<0.039	<0.034	<0.026
2,4,6-trinitrotoluene	<0.039	<0.034	<0.026
2,4-dinitrotoluene	<0.039	<0.034	<0.026
2,6-dinitrotoluene	<0.039	<0.034	<0.026
2-Amino-4,6-dinitrotoluene	<0.039	<0.034	<0.026
2-nitrotoluene	<0.039	<0.034	<0.026
3,5-DNA	<0.039	<0.034	<0.026
3-nitrotoluene	<0.039	<0.034	<0.026
4-amino-2,6-dinitrotoluene	<0.039	<0.034	<0.026
4-nitrotoluene	<0.039	<0.034	<0.026
HMX	<0.039	<0.034	<0.026
Nitrobenzene	<0.039	<0.034	<0.026
Nitroglycerine	<0.039	<0.034	<0.026
PETN	<0.096	<0.086	<0.066
RDX	<0.039	<0.034	<0.026
Tetryl	<0.039	<0.034	<0.026

2.5.6 PAHs

Particle plus gas phase PAH emission factors are shown in Figure 5–7 (Sum PAHs) and Tables 19 and 20 (details). While Fig. 21 indicates higher Sum PAHs from the legacy bullet, the limited data (n = 5 total points) for these results suggest that these preliminary results remain to be verified. Naphthalene, pyrene, and phenanthrene are the most predominant PAHs across all three bullet types. The most toxic PAH, common for all three bullet types, is benzo(a)pyrene, which accounts for over 55% of the 16-PAH toxic equivalency value.

Table 19 PAH EFs from firing of the M4 carbine, in milligrams per kilograms of fuel

Targets	M855 salted, n = 2			M855, n = 1		Legacy, n = 2		
	Average mg/kg fuel	Average mg B[a]P TEQ/kg fuel	RPD[a] %	Average mg/kg fuel	Average mg B[a]P TEQ/kg fuel	Average mg/kg fuel	Average mg B[a]P TEQ/kg fuel	RPD[a] %
Naphthalene	9.22E+00	NA[b]	25	8.96E+00	NA[b]	1.59E+01	NA[b]	42
Acenaphthylene	9.33E-01	NA[b]	25	8.25E-01	NA[b]	1.31E+00	NA[b]	49
Acenaphthene	ND	NA[b]	NA[b]	ND	NA[b]	ND	NA[b]	NA[b]
Fluorene	ND	NA[b]	NA[b]	ND	NA[b]	ND	NA[b]	NA[b]
Phenanthrene	9.02E-01	4.51E-04	4	8.48E-01	4.24E-04	1.26E+00	6.28E-04	49
Anthracene	1.48E-01	7.38E-05	37	1.34E-01	6.69E-05	1.76E-01	8.79E-05	34
Fluoranthene	4.10E-01	2.05E-02	7	3.68E-01	1.84E-02	5.08E-01	2.54E-02	62
Pyrene	1.07E+00	1.07E-03	4	9.54E-01	9.54E-04	1.62E+00	1.62E-03	99
Benzo(a)anthracene	7.06E-02	3.53E-04	6	6.35E-02	3.17E-04	6.33E-02	3.16E-04	57
Chrysene	1.21E-01	3.62E-03	4	1.16E-01	3.47E-03	1.52E-01	4.57E-03	66
Benzo(b)fluoranthene	1.92E-01	1.92E-02	5	1.58E-01	1.58E-02	2.09E-01	2.09E-02	62
Benzo(k)fluoranthene	8.42E-02	4.21E-03	37	8.07E-02	4.04E-03	9.28E-02	4.64E-03	91
Benzo(a)pyrene	1.36E-01	1.36E-01	6	1.28E-01	1.28E-01	1.34E-01	1.34E-01	64
Indeno(1,2,3-cd)pyrene	2.00E-01	2.00E-02	11	1.54E-01	1.54E-02	1.82E-01	1.82E-02	76
Dibenz(a,h)anthracene	2.73E-02	3.00E-02	88	ND	0.00E+00	ND	ND	NA[b]
Benzo(ghi)perylene	6.29E-01	1.26E-02	0.04	5.08E-01	1.02E-02	1.09E+00	2.18E-02	114
SUM 16-EPA PAHs	1.41E+01	2.48E-01	18	1.33E+01	1.97E-01	2.27E+01	2.32E-01	51

[a]RPD calculated when n=2.
[b]Naphthalene, acenaphthylene, acenaphthene, and fluorene have not been assigned a toxic equivalent number.

Table 20 PAH EFs from firing of the M4 carbine, in milligrams per round

Targets	M855 Salted, n = 2			M855, n = 1		Legacy, n = 2		
	Average mg/round	Average mg B[a]P TEQ/round	RPD[a] %	Average mg/round	Average mg B[a]P TEQ/round	Average mg/round	Average mg B[a]P TEQ/round	RPD[a] %
Naphthalene	1.59E-02	NA[b]	25	1.56E-02	NA[b]	2.75E-02	NA[b]	42
Acenaphthylene	1.61E-03	NA[b]	25	1.44E-03	NA[b]	2.27E-03	NA[b]	49
Acenaphthene	ND	NA[b]	NA[b]	ND	NA[b]	ND	NA[b]	NA[b]
Fluorene	ND	NA[b]	NA[b]	ND	NA[b]	ND	NA[b]	NA[b]
Phenanthrene	1.56E-03	7.78E-07	4	1.48E-03	7.40E-07	2.18E-03	1.09E-06	49
Anthracene	2.55E-04	1.27E-07	37	2.33E-04	1.17E-07	3.05E-04	1.52E-07	34
Fluoranthene	7.08E-04	3.54E-05	7	6.43E-04	3.22E-05	8.82E-04	4.41E-05	62
Pyrene	1.84E-03	1.84E-06	4	1.67E-03	1.67E-06	2.81E-03	2.81E-06	99
Benzo(a)anthracene	1.22E-04	6.09E-07	6	1.11E-04	5.54E-07	1.10E-04	5.49E-07	57
Chrysene	2.08E-04	6.24E-06	4	2.02E-04	6.05E-06	2.64E-04	7.92E-06	66
Benzo(b)fluoranthene	3.31E-04	3.31E-05	5	2.76E-04	2.76E-05	3.62E-04	3.62E-05	62
Benzo(k)fluoranthene	1.45E-04	7.27E-06	37	1.41E-04	7.05E-06	1.61E-04	8.04E-06	91
Benzo(a)pyrene	2.35E-04	2.35E-04	6	2.23E-04	2.23E-04	2.33E-04	2.33E-04	64
Indeno(1,2,3-cd)pyrene	3.46E-04	3.46E-05	11	2.70E-04	2.70E-05	3.16E-04	3.16E-05	76
Dibenz(a,h)anthracene	4.70E-05	5.17E-05	88	ND	ND	ND	ND	NA[b]
Benzo(ghi)perylene	1.08E-03	2.17E-05	0.04	8.88E-04	1.78E-05	1.89E-03	3.79E-05	114
SUM 16-EPA PAHs	2.44E-02	4.29E-04	18	2.32E-02	3.44E-04	3.93E-02	4.03E-04	51

[a]RPD calculated when n = 2.

[a] Naphthalene, acenaphthylene, acenaphthene, and fluorene have not been assigned a toxic equivalent number.

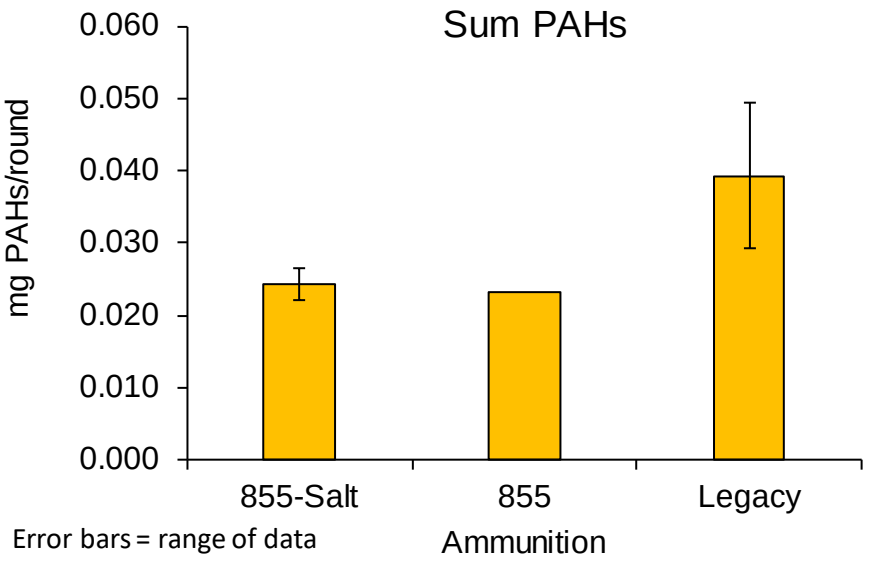

Fig. 21 PAH EFs from firing of the M4 carbine

The PAH results obtained here are often three orders of magnitude higher than particle phase (only) data from Wingfors et al. (2014; Table II, p. 286) indicating the predominantly volatile nature of the PAHs.

2.5.7 Size Distributions

The initial normalized mass weighted size distribution of the emissions is shown in Fig. 22. The size distribution was similar for all three ammunition types, with a mass median diameter ranging of 0.389 ± 0.109 µm for the M855 salted, 0.330 ± 0.124 µm for the M855, and 0.575 ± 0.130 µm for the legacy ammunitions. These differences in size distribution between ammunition types were not statistically significant.

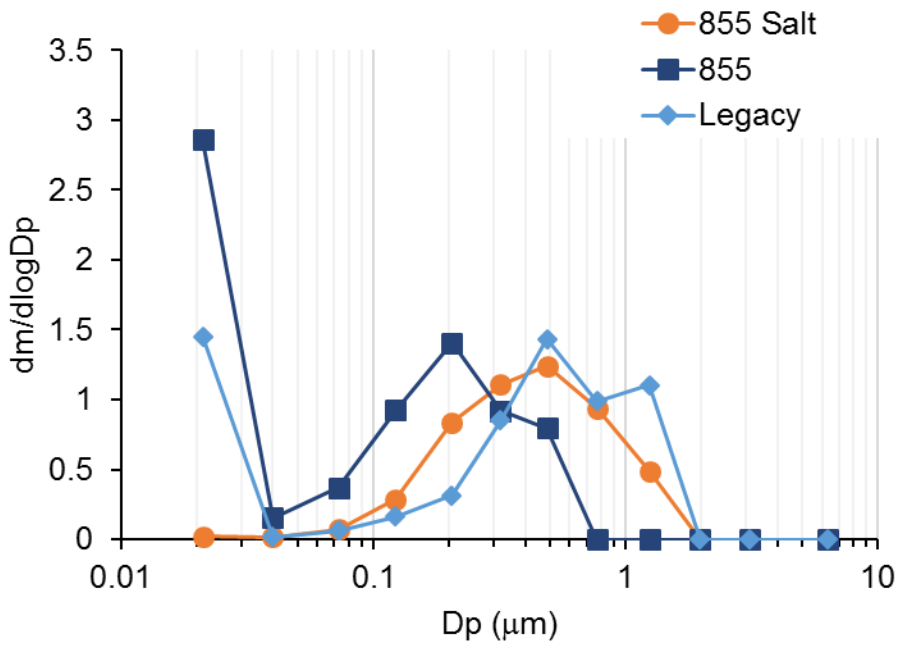

Fig. 22 Representative initial mass normalized mass weighted PM size distributions from the M4 carbine for different ammunition types

The initial size distribution evolved rapidly over the first few seconds as the particles aggregated causing a shift toward larger diameter particles (Fig. 23). Initially, the mass distribution has a median diameter of approximately 96 nm and all the particles present are smaller than 2.5 µm. Over the first minute, the particles agglomerate rapidly and the median diameter shifts to 766 nm after 30 s, with a sizeable fraction of particles larger than 1 µm. This agglomeration process explains the slightly larger PM_{10} emission factors versus $PM_{2.5}$ emission factors despite the initial particle distributions all being significantly smaller than 10 µm in diameter.

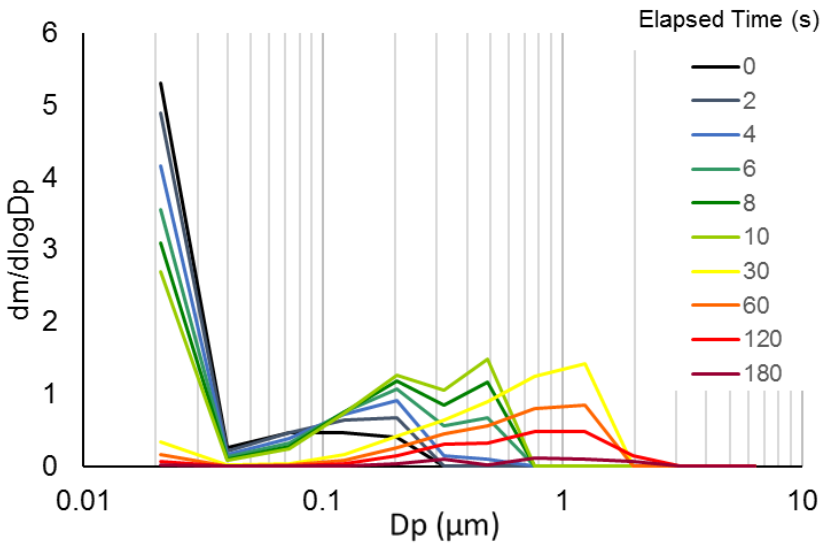

Fig. 23 Mass normalized mass weighted PM size distributions from the M4 carbine for M855 ammunition over the first 3 min after the blast

The color ratio is the ratio of the incandesce signal for each particle in the range from 580 to 710 nm to that of the incandescence in the wavelength range from 330 to 550 nm. A larger color ratio indicates a shift toward longer wavelengths in the incandescence spectrum, which is caused by a lower temperature at which the particle incandesces, which denotes a differing particle composition. The color ratio of incandescing particles emitted from gun blasts with M855 ammunition and M855 salted ammunition is shown in Fig. 24. The color ratio had a bimodal distribution that varied between ammunition types, indicating that two different incandescing particle types were present in the emissions. The smaller mode of the color ratio is consistent with that for carbonaceous soot and the larger mode may be associated with a metal oxide. These results suggest that the SP2 color ratio may be used to distinguish between particles of different composition, although further study is needed to identify the composition of these particles.

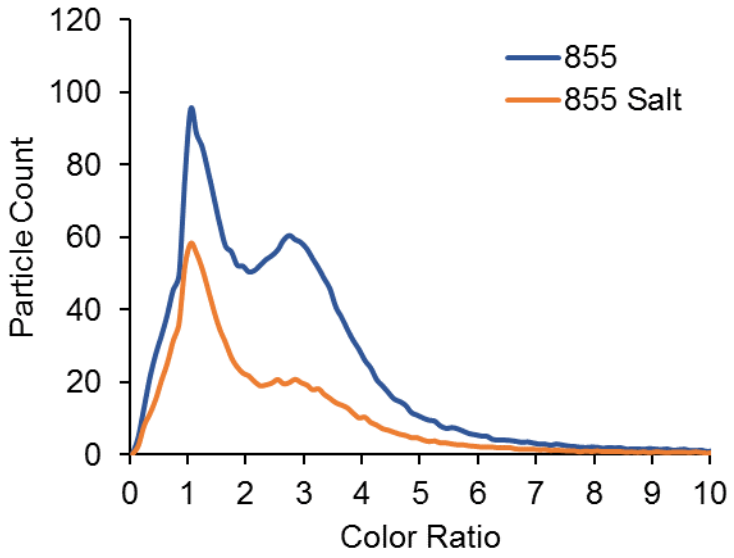

Fig. 24 Color ratio for incandescing particles in the emissions from the M4 carbine for M855 and M855 salted ammunition types

2.6 Discussion

Table 21 shows measured and calculated MCE for the M855 ammunition fired by the M4 carbine. The NASA-Lewis simulation and the CHEETAH-CHEMKIN simulation overpredict the MCE for the gun-firing event.

Table 21 MCE for firing of M855 ammunition in the M4 rifle based on results reported here

	MCE
M855 salted (experiment)	0.49 (0.056)
M855 (experiment)	0.5 (0.064)
M855 legacy (experiment)	0.44 (0.080)
NASA-Lewis simulation with soot formation M855	0.732
CHEETAH/CHEMKIN gun calculation M855	0.998

Although the NASA-Lewis simulation results in a MCE closer to the measured results, the code overpredicts CO_2 at the muzzle. The prediction of zero condensed species by CHEETAH does not match with high-speed images of the event (see Figs. 1 and 7) or measurements of particulates. The NASA-Lewis simulation allows for variable amounts of condensed carbon, but overpredicts measured CH_4 and CO_2 concentrations. It should be noted that the temperature used in the CHEMKIN kinetic calculation to predict CO oxidation was 1,000 K, and heat dissipation was not accounted for during the kinetic calculation. We believe that an improved simulation will take better account of particle production during interior ballistics, and that a much lower temperature for afterburn of muzzle gases may lower the calculated MCE. Finally, future testing should include detailed measurement of

HCN gas. HCN is expected to be present at levels of approximately 1 mg per gram of propellant burned (Kirchner et al. 1993; Wingfors et al. 2014).

3. Detonations of Solid Chemical Explosives

3.1 Background

Our approach to predicting the products from open detonation (OD) of neat and metallized solid chemical explosives is based on time evolution of the energy release processes. This has been studied by thousands of researchers over the last 150 years (Rankine 1870; Kistiakowski and Wilson 1941; Mader 2008), yet because of the high rate at which energy release occurs, many aspects of the process remain under investigation (Glumac 2013). Energy release following initiation of solid chemical explosives may be approximated to occur in stages (McNesby et al. 2010). The first stage of energy release includes detonation of the solid explosive, in which an exothermic chemical reaction is propagated by a compressive shock wave, and the subsequent anaerobic expansion of the products of the chemical reaction (Kinney and Graham 1985). The second stage of energy release occurs when the products of the first-stage burn in surrounding air (called afterburn, or fireball) (Kuhl et al. 1998). The power of the second stage is dependent on chemical species produced in the first stage. The power in each stage is dependent upon the initial chemical formulation, although the first stage of energy release in most solid explosives is more powerful than the second stage (Kim 2004). Figure 25 is a set of images, taken by the authors, depicting energy release following initiation of 2.2 kg of solid TNT. This image sequence was created using high-speed cameras and high-brightness illumination techniques (McNesby et al. 2005). In solid TNT, the rate at which the detonation propagates is approximately 7 mm/μs. In the first stage, near the peak of the compressive shock wave, the reacting TNT has a density slightly higher than bulk (1.7 g/cm^3), a peak temperature near 3,300 K, and a pressure near 20 GPa. In the second stage, the fireball radial expansion rate varies as a function of time, from 7 mm/μs at very early times to sonic velocity (0.35 mm/μs) at later times (Meyer et al. 2007).

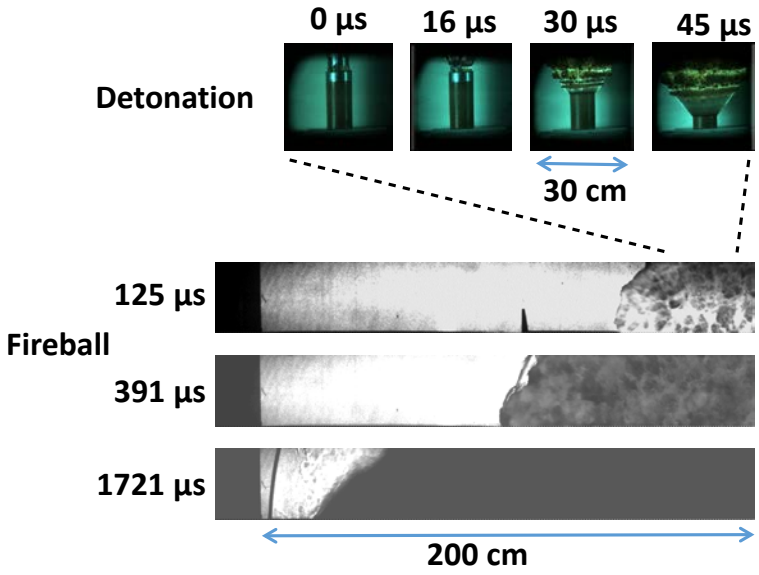

Fig. 25 A composite image sequence (two different experiments) showing stages of energy release following initiation of 2.2 kg of the solid explosive TNT. The air shock may be seen detaching from the detonation product species in the last two images.

As shown in Fig. 25, when the detonation has completed, the detonation product gases are hot, dense, and expanding. As the gases expand and cool, chemical reactions occur between the initial detonation products, reaching an equilibrium composition at each temperature (Johansson and Persson 1970). The chemistry occurring in the initial expansion is anaerobic. As the gases continue to expand and cool, their composition becomes fixed. For simulation purposes, this is the end of the first stage of energy release. As the hot gases of fixed composition continue to expand, they mix with air, and if they are fuel-rich and hot enough, afterburning (fireball) begins (Frost et al. 2002). Combustion chemistry occurring during afterburning determines the magnitude of second stage of energy release.

The approach we employ to predict final products of detonation/explosion attempts to simulate, and link, the two stages of energy release described previously. For this, we use equilibrium chemical calculations to predict anaerobic detonation product species (first stage) followed by finite-rate CHEMKIN to calculate air combustion of these detonation products (second stage). The initial chemical species produced during detonation and anaerobic expansion and their relative amounts, density, and temperature are predicted by the equilibrium simulation computer code CHEETAH (LLNL 2010). As mentioned previously, we approximate the end of the first stage of energy release as the density and temperature at which chemical species stop changing (i.e., “freeze out”). For most energetic materials this occurs near a temperature of 1,800 K. To predict the second stage of energy release (aerobic combustion), we use the CHEMKIN simulation

code, marketed by Reaction Design, Inc. The CHEMKIN simulation code uses finite-rate chemical kinetics to predict rates of combustion, species evolution, temperature, and energy release. To use this simulation, it is necessary to have initial temperature and pressure, type of combustion system (e.g., premixed, well-stirred reactor, opposed flow, and so on), chemical species, and individual chemical reactions and their rates (the reaction mechanism) (Glassman 1987). In the work described here, the chemical species used in the input to CHEMKIN are those predicted by CHEETAH at species freeze out. The time evolution of chemical species and temperature is simulated as a function of initial temperature in a homogeneous mixture of 1% to 50% detonation products with the balance air. The reaction mechanism is based on the GRI-mech kinetic database (Smith et al. 2004) and is supplemented by the chemical combustion mechanisms found in the Lawrence Livermore National Laboratory (LLNL) explosives handbook, on the Sandia National Laboratories (SNL) website (Appel et al. 2000), and through published articles in the peer-reviewed literature (Spadaccini and Colket 1994). It should be noted that a more complete picture is provided by incorporating flow dynamics, turbulence, and multiphase combustion (i.e., combustion of solid particles) (Davini et al. 1996). The inclusion of these enhancements is beyond the scope of the present work.

3.2 Materials

Two types of detonable solid chemical explosives were tested:

- TNT
- TNT with Mg:B additives at 80:4:16 mass ratio

TNT was selected as the base solid chemical explosive because it has a large negative oxygen balance. At the end of stage-one energy release as described previously, the explosive products consist of approximately 30% by mole fraction of graphitic carbon (LLNL 2010). The Mg:B metal additive was chosen because it consists of a metal (Mg) known to react rapidly in explosive formulations and a semi-metal (B) known to partially react in explosive formulations (McNesby et al. 2010). Table 22 lists composition, by mass, for each detonative material tested, including the explosive train (excluding RP-80 detonator). The RP-80 detonator (Teledyne-RISI) is an exploding bridgewire device, and uses 80 mg of PETN as an initiator and 123 mg of 1,3,5-trinitro-1,3,5-triazinane (RDX) as an output explosive. According to the manufacturer, it does not contain lead azide.

Table 22 Detonation composition in mass per charge (includes detonation train components, excluding detonator)

Test item	TNT g/charge	TNT:Mg:B g/charge
TNT	640	565
PMMA centering device	18.9	18.9
Pentolite	5.0	6.0
Comp B: TNT	67	67
RDX	103	103
Wax	17	17
B	NA	70.5
Mg	NA	70.5

NA = not applicable (not in the composition).

3.3 Methods

3.3.1 TNT Test Series

For the TNT test series to measure EFs, TNT right circular cylinders, each weighing approximately 660 g, were exploded in ARL Detonation Science Facility indoor blast chamber at Aberdeen Proving Ground, Maryland. To obtain assurance of a detonation, each explosion was imaged using a high-speed framing camera (2.5 million fps, Cordin Co. Model 570) and wavelength-resolved emission spectra were recorded for each event for the duration of the framing camera recording time (Princeton Instruments PI-Max-4). By measuring the rate at which the imaged detonation front travelled through the solid explosive (McNesby et al. 2016), it was determined that the reaction front travelled faster than the sound speed in solid TNT, and at the velocity found in the literature, satisfying the main criterion for a detonation (Cooper 1996). Figure 26a shows the explosive assembly to include an RP-80 detonator (not shown, Teledyne-RISI), a 0.5- × 0.75-inch pentolite initiator pellet (50% TNT, 50% PETN, $C_5H_8N_4O_{12}$) in a PMMA holder (into which the detonator is inserted), a 2- × 2-inch Comp-B booster (40% TNT, 60% RDX, $C_3H_6N_6O_6$), and the main TNT charge (2- × 8-inch right circular cylinder, labelled no. 3 in Fig. 26a). Figure 26b shows the assembled explosive charge prior to initiation. Because an emission spectrum of the event was being recorded, no exterior illumination was used. Figure 27a–h shows the cigarette-like progression of the reaction front following initiation of the explosive charge. The images are self-illuminating. The brightest region in images Fig. 27g–h are from air ionization as the detonation pushed out the bottom end of the cylindrical explosive charge (Davis et al. 2006).

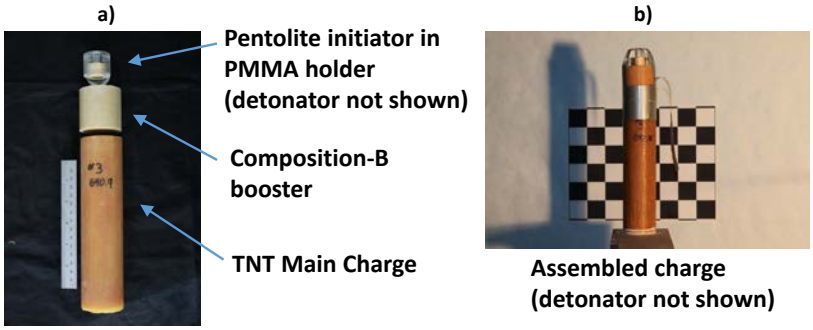

Fig. 26 a) a photo of the components of the TNT charge used in the tests. b) The assembled charge. The detonator (RISI RP-80) is not shown.

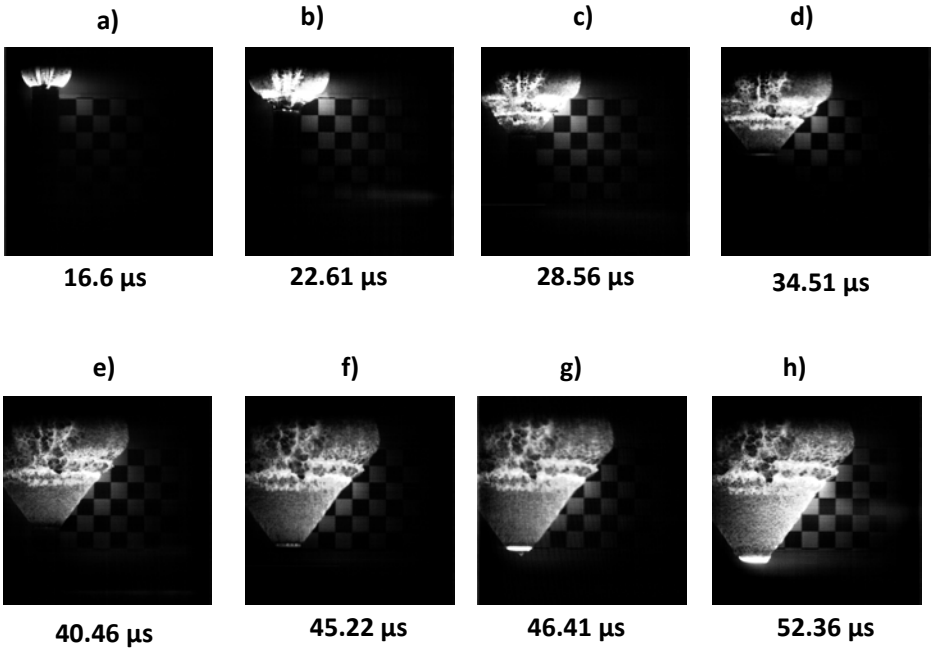

Fig. 27 Sequential images (self-illuminating) of the reaction front following initiation of the TNT charge shown in Fig. 26. The measured velocity of the reaction front was 7 mm/µs, consistent with the detonation velocity in neat TNT (Cooper 1996).

3.3.2 TNT:Mg:B Test Series

Figure 28 shows a photo of the explosive assembly to include an RP-80 detonator (not shown, Teledyne-RISI), a 0.5- × 0.75-inch pentolite initiator pellet (50% TNT, 50% PETN, $C_5H_8N_4O_{12}$) in a PMMA holder (into which the detonator is inserted), a 2- × 2-inch Comp-B booster (40% TNT, 60% RDX, $C_3H_6N_6O_6$), and the main TNT:Mg:B charge (80:4:16 by weight). Because an emission spectrum of the event was being recorded (not shown in this report), no exterior illumination was used for imaging the explosives cylinder during function. Figure 29a–g shows the cigarette-

like progression of the reaction front following initiation of the explosive charge. The images are self-illuminating.

Fig. 28 A photo of the components of the TNT:Mg:B charge used in the tests. The black color of the main charge is caused by the B additive.

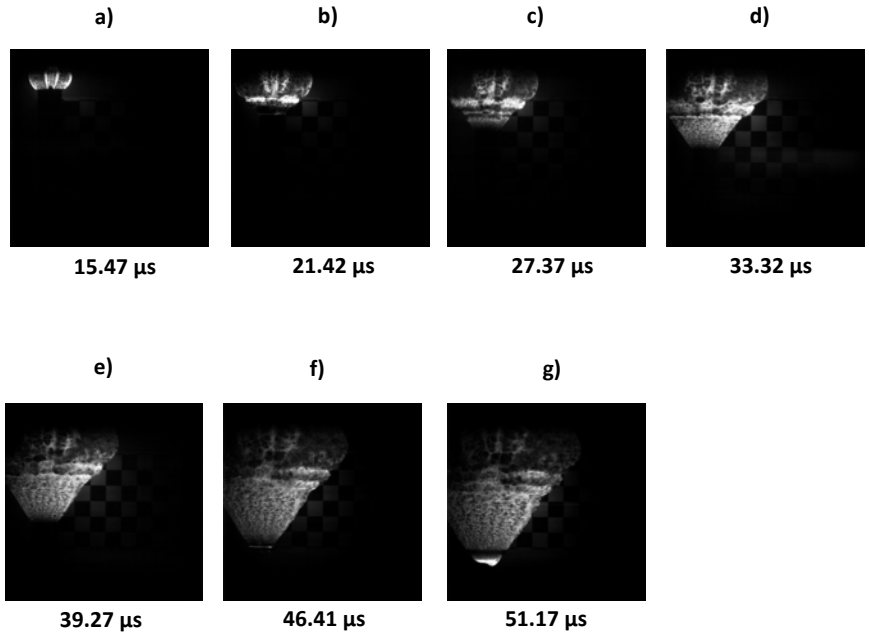

Fig. 29 The cigarette-like progression of the reaction front following initiation of the TNT:Mg:B (80:4:16 by weight) explosive charge. The images are self-illuminating.

3.3.3 Target Analytes and Collected Target Analytes – Detonations of Solid Explosives

The target analytes for detonations of solid explosives are listed in Table 23. CO_2 and CO were successfully measured continuously through all tests. The total number of target analyte samples collected for each type of detonation are shown in Table 24.

Table 23 Target analytes for detonations of solid explosives

Analyte	Instrument/method	Frequency
CO_2	Nondispersive infrared	Continuous
CO	Electrochemical cell	Continuous
$PM_{2.5}$[a]	Impactor, Teflon filter	Batch
PM_{10}[b]	Impactor, Teflon filter	Batch
NC	Glass fiber filter	Batch
Nitroaromatics	Glass fiber filter	Batch
PAHs	Glass fiber filter and PUF	Batch
Elements	Teflon filter from $PM_{2.5}$ batch filter	Batch
VOCs	SUMMA canister	Batch
PM size distribution	Electrical low pressure impactor	Continuous and batch
PM composition/size	Single particle soot photometer	Continuous and batch

[a]Fine particles in the ambient air with particles less than or equal to 2.5 μm in diameter.
[b]Fine particles in the ambient air with particles less than or equal to 10 μm in diameter.

Table 24 Collected target analytes for the solid explosives TNT and TNT:Mg:B

Analyte	TNT	TNT:Mg:B	Total
$PM_{2.5}$	3	3	6
PM_{10}	2	2	4
Nitroaromatics	2	3	5
Elements	5	5	10
VOCs	2	2	4
PAHs	2	3	5
PM size	2	2	4
PM size/composition	3	3	6

3.3.4 Samplers and Analytical

The sampling equipment for analysis of detonations of solid explosives was the same used for analysis of M4 gun firings (see Section 3).

3.3.5 Test Chamber

Detonations of solid chemical explosives took place within the small blast chamber at the ARL Detonation Science Experimental Facility in Aberdeen, Maryland. The blast chamber is a squashed sphere, 4.9 m tall and 4.9 m in diameter. The chamber

is equipped with a stack attached to the ceiling, open to atmosphere, to prevent overpressure. Following explosive initiation, a second vent was opened and the bulk of product gases exhausted to the outside via a separate roof port, typically a 15–20 min process. The charges were 50- × 200-mm right circular cylinders. Each type of charge (neat TNT and TNT:Mg:B), and the explosive train, are described in detail in Sections 3.2 and 3.3. Detonator initiation was by a RISI FS-43 control unit, with time gating provided by a Cordin Company Model 454 time-delay generator. The charges were initiated in two configurations, depending upon whether imaging was being used to verify detonation of the solid chemical explosive or whether species emission was being measured.

For verification of detonation, the solid chemical explosive assembly sat on a wooden platform approximately 1.2 m from the blast chamber floor, and detonation and explosion imaged indirectly via a 20-inch square first-surface mirror through one of the chamber optical ports. This was done to maximize time before ground shock reflections disturb the detonation product expansion. A schematic of the charge within the blast chamber and position of the Cordin Model 570 digital framing camera is shown in Fig. 30. The photo of a TNT charge assembly, positioned on the wooden platform within the ARL small blast chamber is shown in Fig. 31.

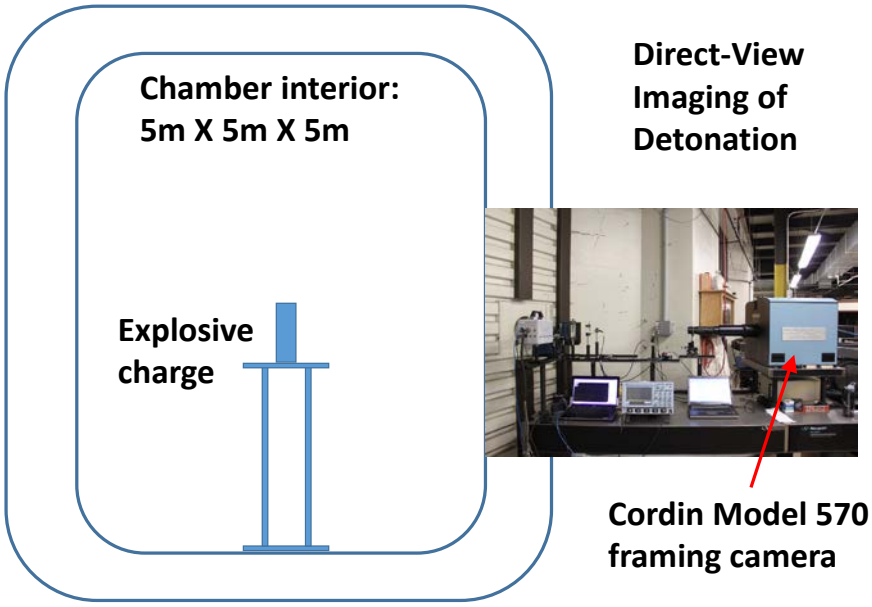

Fig. 30 A schematic of the charge placement within the ARL small blast chamber for testing when the Cordin Model 570 high-speed framing camera was used to verify detonation of the solid chemical explosive

Fig. 31 The TNT charge assembly (minus detonator), positioned on the wooden platform within the ARL small blast chamber (also see Fig. 30). This configuration was used for high-speed imaging of the detonation and explosion.

For emission sampling of gases and particles, the explosive charge was placed on the deck (floor) of the ARL small blast chamber, to minimize wood combustion products being sampled. A schematic of the charge on the deck of the ARL small blast chamber, and the relative position of the gas and particle sampling apparatus is shown in Fig. 32.

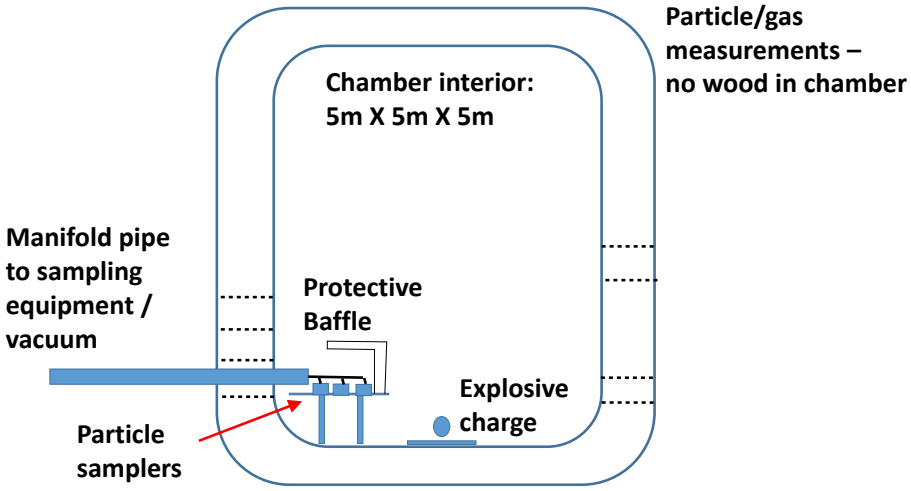

Fig. 32 A schematic of the charge assembly and gas and particle emission apparatus during gas and particle emission measurement

Figure 33 shows a photograph of a TNT:Mg:B explosive assembly, positioned on the deck of the blast chamber, prior to gas and particle emission measurement.

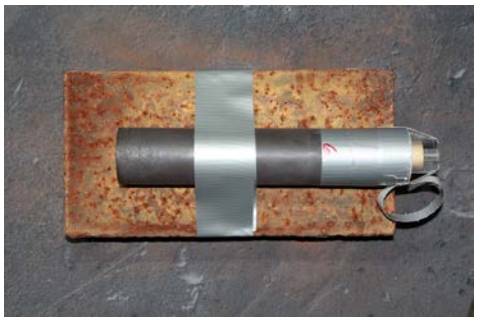

Fig. 33 A photograph of a TNT:Mg:B explosive assembly, positioned on the deck of the blast chamber, prior to initiation and subsequent gas and particle emission measurement

Emission sampling of gases and particles was accomplished via an extractive probe set through the blast chamber wall. Additionally, $PM_{2.5}$ and PM_{10} were collected inside the chamber in tandem with a second set of CO_2 and CO sensors. The sampling apparatus for emissions from detonations of solid chemical explosions is shown in Fig. 34.

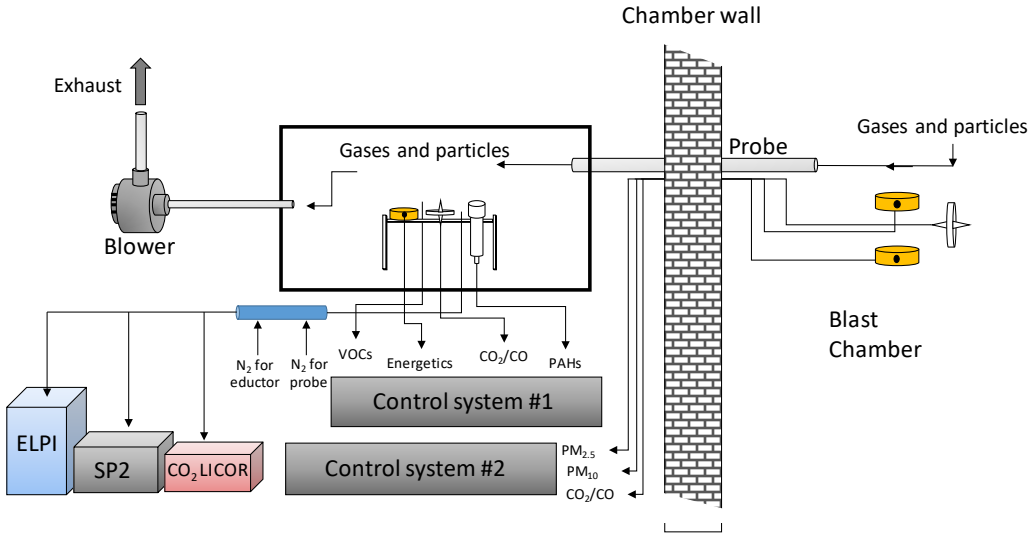

Fig. 34 The sampling apparatus for emissions from detonations of solid chemical explosions

Figure 35 shows a photograph of the sampling apparatus interior to the blast chamber and a detail of this apparatus, showing the particle sample canisters and the interior CO_2 and CO sensors. Figure 36 is a photo of the sampling and control electronics exterior to the blast chamber.

a) b)

Fig. 35 a) The sampling apparatus interior to the blast chamber and b) a detail of the interior sampling apparatus, showing the particle sample canisters and the interior CO_2 and CO sensors

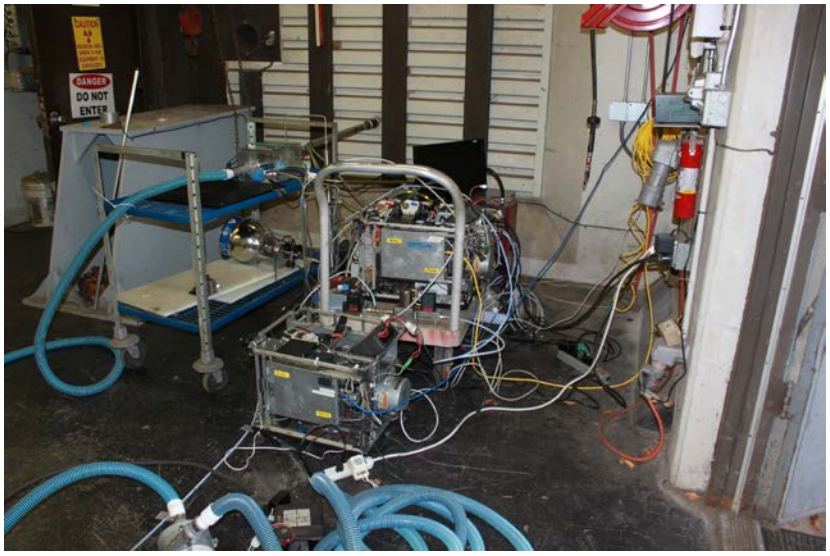

Fig. 36 A photo of the sampling and control electronics, and plumbing for sample extraction, exterior to the ARL small blast chamber

3.4 Results of Simulations

3.4.1 Prediction of Detonation Product Species of TNT – CHEETAH

As mentioned previously, the approach we employ to calculate products of TNT detonation/explosion uses CHEETAH and CHEMKIN to mimic the stages of energy release of the actual event (see Fig. 25). The output of CHEETAH is used to simulate the first stage of TNT energy release (i.e., the detonation), and determines the input to CHEMKIN, which is used to simulate the second stage of TNT energy release (i.e., the fireball). The chemical equilibrium calculator

CHEETAH (V6.0, note later versions are available) predicts the composition, density, temperature of the initial products of the detonation prior to expansion (the "Chapman-Jouguet [C-J] point" for TNT, T = 3,400 K, P = 20 GPa), and the changing chemical composition for the anaerobic expansion of the detonation product gases (Cooper 1996). At some time after detonation, the composition of the expanding gases becomes fixed. For TNT, this temperature and composition is called "freeze out" and occurs near 1,800 K at a pressure of 1 atm. Because TNT does not contain enough oxygen to fully oxidize the carbon in the molecule, the detonation products are a fuel source (Kim 2004). When they mix with ambient air, an aerobic combustion reaction may occur that produces the yellow fireball associated with TNT detonation/explosion. CHEETAH will also predict the species that result when the original explosive is burned in excess air. Using CHEETAH, it is possible to predict the composition of chemical species produced when TNT detonates, TNT products expand, and TNT products burn in excess air. The balanced chemical equation for the full detonation and combustion of TNT in excess air is

$$4\ C_7H_5N_3O_6 + 21\ O_2 \ = \ 6\ N_2 \ + 28\ CO_2 \ + 10\ H_20 \qquad \Delta H = -15\ kJ/g. \tag{5}$$

Table 25 shows the predicted evolution of the most prevalent (99.9% accounting) detonation products (solid and gaseous) of TNT from the C-J point (3,240 K, 20 GPa), to freeze out (1,800 K, 1 atm), as predicted by CHEETAH. The full combustion data are based on the reaction stoichiometry as shown in Eq. 5.

Table 25 Detonation products for TNT at different stages of energy release, as predicted by CHEETAH 6.0

C-J point (3,240 K, 20 GPa)		Freeze out (1,800 K, 1 atm)		Full combustion	
Species	**Mole fraction**	**Species**	**Mole fraction**	**Species**	**Mole fraction**
C(gr[a])	0.4311	CO	0.2578	CO_2	0.636
H_20	0.1827	C (gr[a])	0.2575	H_2O	0.227
CO_2	0.1516	N_2	0.1549	N_2	0.136
N_2	0.1036	CO_2	0.1426	…	…
CHNO	0.07937	H_20	0.08459	…	…
CO	0.03361	CH_4	0.06878	…	…
NH_3	0.01306	H_2	0.02635	…	…
CH_4	0.001841	NH_3	0.003647	…	…
H_2	0.001748	C_2H_6	0.001561	…	…
C_2H_4	0.0005828	C_2H_4	0.001193	…	…
CH_3OH	0.0003933	CHNO	0.0007385	…	…
NO	0.00008430	CH_2O_2	0.00009456	…	…
C_2H_6	0.00008216	CH_3OH	0.00007871	…	…
CH_2O_2	0.00007333	HCN	0.00007650	…	…
H	0.00001951	C_2H_2	0.00004298	…	…

Notes: CHNO=isocyanic acid, C_2H_4=ethylene, CH_3OH=methanol, CH_2O_2=formic acid, gr[a] = graphite

3.4.2 Inclusion of Finite-Rate Chemical Kinetics for TNT Afterburn – CHEMKIN

The final chemical species actually produced by exploding TNT may not be those of full combustion (Glassman 1987). The final species may depend on charge confinement, available oxygen, ambient temperature, initial detonation product temperature, and so on. To begin to account for these variations, we use finite-rate CHEMKIN to calculate air combustion of TNT detonation products when these products are mixed with ambient air at varying mixture ratios. The CHEMKIN simulation code, marketed by Reaction Design Inc., is used to predict the time evolution of gas-phase chemical species in the afterburn, or fireball. The initial chemical species and their relative amounts in the CHEMKIN calculation are those predicted by CHEETAH at freeze out (see Table 25). The evolution of the gas phase combustion is simulated as a function of initial temperature in a homogeneous mixture of from 1% to 50% TNT detonation products at atmospheric pressure, with the remainder air. As noted previously, a more accurate chemical kinetic simulation is provided by incorporating flow dynamics, turbulence, and multiphase combustion (i.e., combustion of solid particles) (Kuo and Acharya 2012). The inclusion of these enhancements is beyond the scope of the present work.

3.4.3 Chemical Kinetic Mechanism Reduction

To perform the kinetic calculation, a chemical reaction mechanism (McNesby et al. 2010) was compiled that includes known reaction parameters (rate constants, activation energies) for the combustion of all species predicted by CHEETAH at freeze out for TNT detonation. This mechanism is based on the GRI-mech kinetic database and is supplemented by the chemical combustion mechanisms found in the LLNL explosives handbook, on the SNL website, and through published articles in the peer reviewed literature (Smith et al. 2004). The initial mechanism for combustion of all species predicted at freeze out for TNT contained 2,032 reactions and 249 species (McNesby et al. 2010). This initial chemical kinetic mechanism is too large to allow simulations over a range of input conditions, and for future inclusion of flow dynamics to include incomplete mixing. Therefore, 4 reduced mechanisms were compiled, with between 20 and 34 species and up to 88 reactions (Montgomery et al. 1999; Tomlin et al. 1997).

These reduced mechanisms were compared to results of the full mechanism for ignition delay (the time it takes for the fireball to begin burning after detonation) and peak OH radical concentrations (OH is a main flame propagation radical species, as shown in Figs. 37 and 38). The reduced mechanism that produced results most consistent with those of the full mechanism was selected for the full set of calculations presented here. Although the reduced mechanism was not mandatory

for the homogeneous reactor calculations we believe that it will be needed for calculations that simulate any degree of incomplete mixing (Menon et al. 2003). The reduced mechanism (CHEMKIN format) for combustion of TNT detonation products is provided in Appendix B.

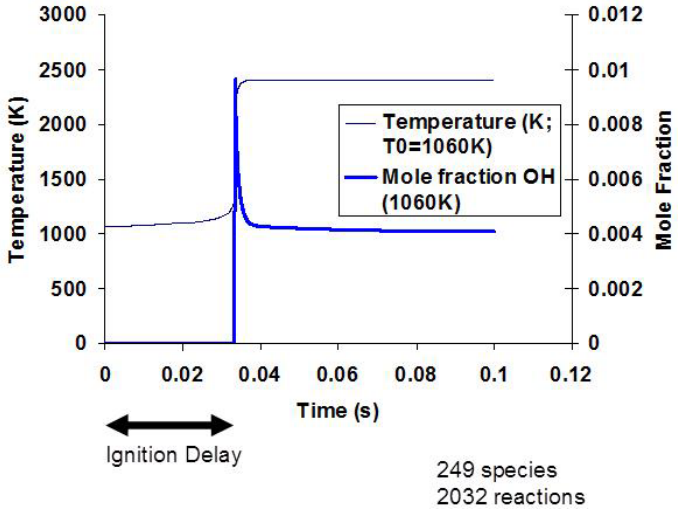

Fig. 37 A CHEMKIN calculation for the onset of ignition (the fireball) for the detonation products of TNT. The full reaction mechanism was used, homogeneous mixing with air (1:1 by volume), initial temperature of 1,060 K.

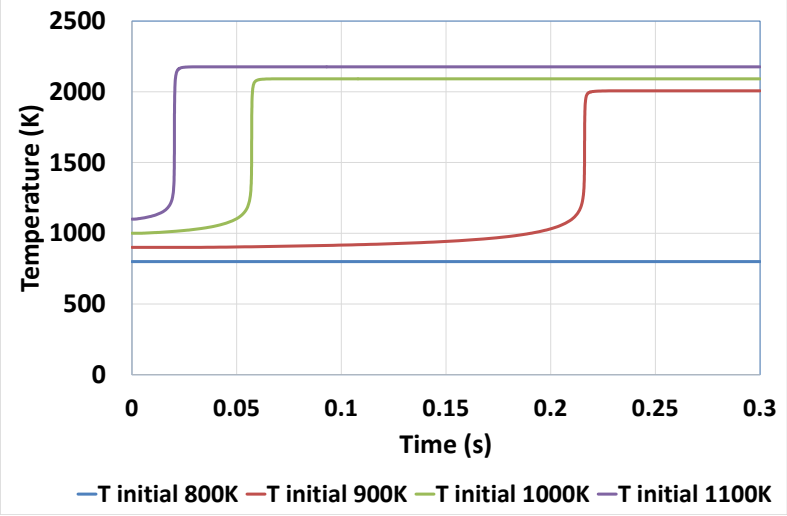

Fig. 38 The temperature dependence of the onset of afterburning (ignition delay) for a 1:1 by volume mixture of TNT detonation products (freeze out) and air

Figure 38 shows the temperature dependence of the ignition delay for onset of afterburn, or fireball. Note that for a temperature below 900 K, the afterburn does not occur. In this case, the species present after explosion would be those predicted by CHEETAH at freeze out.

3.4.4 Combustion of Detonation Products of TNT – Results of CHEMKIN Simulations

The model homogeneous reaction vessel used by us in CHEMKIN does not include heat dissipation. Therefore, if the initial temperature is high enough, the gas phase reaction proceeds until one or more reactants is consumed. Figure 39 shows a bar graph of the most common gas phase species predicted by CHEMKIN before and after the afterburn (fireball) of TNT detonation products in a 1:1 mixture with air. As expected, combustion occurring in this "nascent" fireball (simulating the beginning of the second stage of energy release) further oxidizes CO and hydrocarbons to CO_2 and H_2O. In this case (the 1:1 mixture), the reactant limiting the duration of the afterburn is oxygen from ambient air.

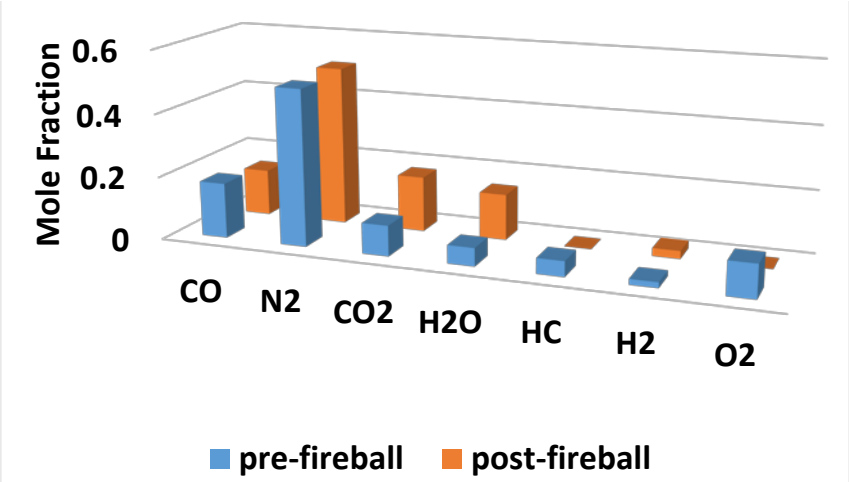

Fig. 39 Results of a CHEMKIN calculation of a homogeneous reactor containing a 1:1 by volume mixture of TNT detonation products and air. Initial temperature was 1,060 K. Pre-fireball are concentrations before combustion begins.

Figure 40 shows a bar graph of the most common gas phase species predicted by CHEMKIN before and after the afterburn (fireball) of TNT detonation products in a 100 parts air: 1 part TNT detonation product mixture. This simulation more closely mimics full combustion. The excess O_2 fully oxidizes CO, hydrocarbons, and H_2 to CO_2 and H_2O. In Fig. 40, neither the O_2 or N_2 mole fractions are shown. Because this figure depicts combustion of small amounts of TNT detonation products in excess air, the N_2 and O_2 mole fractions are omitted because their amounts change minutely relative to actual concentration and because their inclusion would make the mole fractions of detonation product species indistinguishable from each other in Fig. 40.

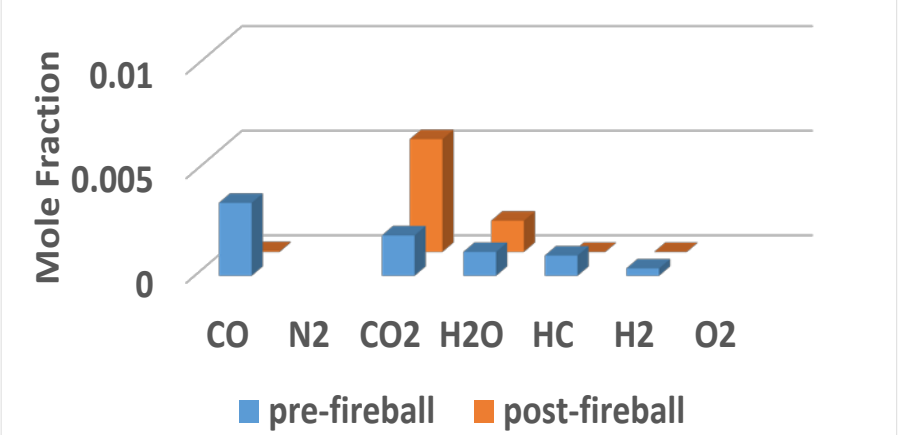

Fig. 40 Results of a CHEMKIN calculation of a homogeneous reactor containing a 100:1 by volume mixture of air and TNT detonation products, respectively. Initial temperature was 1,000 K. N_2 and O_2 are not reported on this graph (see text).

3.4.5 Predicted Emission Factors for TNT Detonations

A comparison of emission factors, calculated using CHEETAH and CHEMKIN for detonation/explosions of TNT, based upon simulations described previously, is shown in Table 26. The simulation of the 100:1 TNT detonation product:air EF is very similar to the full combustion emission factor, with the exception that the full combustion simulated EF (based on stoichiometry shown in Eq. 5) assumes all initial carbon is oxidized to CO_2.

Table 26 Predicted EFs for explosions of neat TNT (gram of emitted species per gram TNT)

Species	CHEETAH	CHEMKIN 1:1 air	CHEMKIN 100:1 air	Full combustion
C-graphite	0.13	0.13	0.13	…
CO	0.304	0.255	0.005	…
N_2	0.182	0.184	0.184	0.184
CO_2	0.264	0.476	1.17	1.36
H_2O	0.064	0.162	0.172	0.176
CH_4	0.0464	Trace	Trace	…
H_2	0.00224	0.00311	Trace	…

Note: MCE = $\Delta C_{CO2}/(\Delta C_{CO2} + \Delta C_{CO} + \Delta C_{CH4} + \Delta C_{PC}) = 0.866$.

3.4.6 Prediction of Detonation Product Species of TNT:B:Mg – CHEETAH

As mentioned previously, the approach we employ to calculate products of TNT (neat, 100%) and TNT:Mg:B (80%:4%:16% by weight) detonation/explosion uses CHEETAH and CHEMKIN to mimic the stages of energy release of the actual event (see Fig. 25). The output of CHEETAH determines the input to CHEMKIN. The chemical equilibrium calculator CHEETAH (V6.0; later versions are available) predicts the composition, density, temperature of the initial products of the

detonation prior to expansion (C-J point for TNT:Mg:B (inactive) T = 2,975 K, P = 7.4 GPa), and changing chemical composition for the anaerobic expansion of the detonation product gases (Cooper 1996).

For TNT:B:Mg, the CHEETAH calculation offers predictions for B active and for B inactive. For B active calculations, enthalpy of formation of B oxidation products are considered in the calculation (e.g., ΔH for B_2O_3, HOBO, and so on [Dreizin et al. 1999]). For B inactive (Yeh and Kuo 1996), B is considered to be inert. The Mg in the explosive formulation is considered to be reactive in all CHEETAH calculations described here. As described previously for TNT, at some time after detonation, the composition of the expanding gases becomes fixed (freeze out). Because the TNT:B:Mg formulation does not contain enough oxygen to fully oxidize the carbon, B, and Mg in the formulation, the detonation products are a fuel source (Kim 2004). When they mix with ambient air, an aerobic reaction may occur, producing a fireball. As for neat TNT, using CHEETAH, it is possible to predict the composition of chemical species produced when the TNT:B:Mg formulation detonates, and products expand to a fixed composition. The balanced chemical equation for the detonation and combustion of TNT:Mg:B (B inactive) in oxygen is

$$4\ C_7H_5N_3O_6 + B + 2Mg + 22\ O_2 = 6\ N_2 + 28\ CO_2 + 10\ H_20 + B + 2MgO. \quad (6)$$

For B active, the balanced chemical equation is

$$4\ C_7H_5N_3O_6 + 2B + Mg + 23\ O_2 = 6\ N_2 + 28\ CO_2 + 10\ H_20 + B_2O_3 + MgO. \quad (7)$$

Tables 27 and 28 show the predicted evolution of the most prevalent (99.9% accounting) detonation products (solid and gaseous) of TNT:Mg:B from the C-J point (3,514 K, 16.9 GPa, B inert) to freeze out (1,800 K, 1 atm), for B inactive and B active, respectively. Also shown are the product mole fractions based upon Eqs. 6 and 7, respectively.

Table 27 Detonation products for TNT:B:Mg (80:4:16 by weight, B inactive) at different stages of energy release, as well as products based on reaction stoichiometry (Eq. 6).

C-J point (3,514 K, 16.9 Pa)		Freeze out (1,800 K, 1 Atm)		Full combustion	
Species	**Mole fraction**	**Species**	**Mole fraction**	**Species**	**Mole fraction**
C (gr[a])	0.3354	CO	0.3131	CO_2	0.47
H_20	0.1204	C (gr[a])	0.1365	H_2O	0.169
CO_2	0.06704	N_2	0.1130	N_2	0.101
N_2	0.08052	CO_2	0.01948	MgO	0.079
CHNO	0.04457	H_20	0.01488	B	0.178
CO	0.05129	CH_4	0.05785	…	…
NH_3	0.01240	H_2	0.05299	…	…
CH_4	0.004711	NH_3	0.0009868	…	…
H_2	0.004455	C_2H_6	0.0006369	…	…
C_2H_4	0.002061	C_2H_4	0.001167	…	…
CH_3OH	0.0005025	CHNO	0.0001106	…	…
NO	0.00007832	CH_2O_2	trace	…	…
C_2H_6	0.0002948	CH_3OH	trace	…	…
CH_2O_2	0.0001280	HCN	0.0007358	…	…
H	0.00005574	C_2H_2	0.0001708	…	…
MgO (s[b])	0.08492	MgO (s[b])	0.08875	…	…
B (s)	0.1909	B (s[b])	0.1995	…	…

gr[a] = graphite; s[b] = solid

Table 28 Detonation products for TNT:Mg:B (80:4:16 by weight, B active) at different stages of energy release, as well as products based on reaction stoichiometry (Eq. 7)

C-J point (3,746 K, 16.9 GPa)		Freeze out (1,800 K, 1 Atm)		Full combustion	
Species	Mole fraction	Species	Mole fraction	Species	Mole fraction
C(gr[a])	0.03955	CO	0.3642	CO_2	0.519
H_20	0.03643	C (gr[a])	0.1538	H_2O	0.185
CO_2	0.002121	N_2	0.01385	N_2	0.111
N_2	0.1102	CO_2	0.0002987	B_2O_3	0.098
CHNO	0.01013	H_20	0.0005218	MgO	0.087
CO	0.02226	CH_4	0.009040	…	…
NH_3	0.02917	H_2	0.1690	…	…
HOBO	0.007589	HCN	0.001039	…	…
C_2H_2	0.001033	C_2H_2	0.0007332	…	…
NO	0.00007832	HOBO	0.0001096	…	…
CH_4	0.03052	NH_3	Trace	…	…
H_2	0.02056	C_2H_6	Trace	…	…
C_2H_4	0.01633	C_2H_4	0.0001953	…	…
CH_3OH	0.0005025	CHNO	Trace	…	…
C_2H_6	0.003131	CH_2O_2	Trace	…	…
CH_2O_2	0.0001280	CH_3OH	Trace	…	…
H	0.00005574	HCN	0.001039	…	…
MgO (s[b])	0.08492	C_2H_2	0.0007332	…	…
B (s[b])	0.1909	MgO (s[b])	0.08849	…	…
C (l[c])	0.4588	BN (s[b])	0.1985	…	…
B_2O_3 (l[c])	0.1099	B_2O_3 (l[c])	0.0001562	…	…
MgO (l[c])	0.1012	…	…	…	…

gr[a] = graphite; s[b] = solid; l[c] = liquid

Tables 29 and 30 show EFs and MCEs based upon CHEMKIN input derived from Table 29.

Table 29 Calculated EFs (gram of emitted species per gram TNT:Mg:B) and MCEs, for neat TNT:Mg:B (80:4:16 by weight), B inactive

Species	CHEMKIN 100:1 air	Full combustion
C (gr[a])	0.076	…
CO	0.00026	…
N_2	…	0.184
CO_2	0.803	1.36
B	0.1	0.1
MgO	0.165	0.166
H_2O	0.165	0.198
CH_4	Trace	…
H_2	Trace	…

gr[a] = graphite

Note: MCE = $\Delta C_{CO2}/(\Delta C_{CO2} + \Delta C_{CO} + \Delta C_{CH4} + \Delta C_{PC}) = 0.74$.

Table 30 Calculated EFss (gram of emitted species per gram TNT:Mg:B) and MCEs, for TNT:Mg:B (80:4:16 by weight), B active

Species	CHEMKIN 100:1 air	Full combustion
C (gr[a])	0.086	…
CO	0.00014	…
N_2	…	0.184
CO_2	0.768	1.36
B	…	…
MgO	0.165	0.166
H_2O	0.158	0.198
CH_4	Trace	…
H_2	Trace	…
BN	0.23	…
B_2O_3	…	0.644

gr[a] = graphite
Note: MCE = $\Delta C_{CO2} / (\Delta C_{CO2} + \Delta C_{CO} + \Delta C_{CH4} + \Delta C_{PC}) = 0.71$.

3.5 Results of Experiments: Solid Chemical Explosives Emission Factors

3.5.1 Emissions of CO_2, CO, and CH_4

Major gaseous carbon species are listed in Table 31 for explosions of neat TNT and for the TNT:Mg:B explosive formulation (80:4:16 by weight). For each explosive tested, initial C oxidation to CO_2 was near complete. Shot-to-shot variation was minor as seen by low RSD and RPD values.

Table 31 CO_2, CO, and CH_4 EFs as well as MCE

Compound	TNT			TNT:Mg:B		
	n[a]	Average g/kg fuel	RPD[b] %	n[a]	Average g/kg fuel	RPD[b] %
CO_2	2	1,314	0.65	2	1,117	1.5
CO	2	17	32	1	15	16
CH_4	2	ND	NA	2	0.16	NA
		Average fraction			Average fraction	
MCE[c]	2	0.980	0.66	2	0.979	0.35

[a] Number of samples collected.
[b] Calculated when n = 2.
[c] MCE = $(\Delta CO_2/(\Delta CO_2+\Delta CO+\Delta CH_4)$.

3.5.2 Particulate Matter (PM)

PM EFs for the detonations are shown in Table 32 and Fig. 41. RSD and RPD values below 23% indicate excellent test to test precision. The PM_{10} values found here for TNT, 61 g/kg, compare with previous values determined by an aerostat-

lofted instrument package in the field (130 g/kg net explosive weight [Aurell et al. 2011]) and laboratory scale (BangBox) studies 73 g/kg (Mitchell and Suggs 1998). Field values were most certainly elevated due to TNT detonation on the surface of a fine, sandy soil resulting in considerable entrainment of background particles. The addition of Mg:B powder to the TNT increases the PM emissions by a factor of 8 and 3 for $PM_{2.5}$ and PM_{10}, respectively.

Table 32 PM EFs from small detonations of TNT and TNT:Mg:B

PM size	Ordnance	n[a]	Average g/kg fuel	Stand. dev. g/kg fuel	RSD[b] %	RPD[c] %
$PM_{2.5}$	TNT	2	22	0.48	2.2	…
PM_{10}	TNT	2	61	…		23
$PM_{2.5}$	TNT:Mg:B	3	166	89	53	…
PM_{10}	TNT:Mg:B	2	204	…	…	23

[a] Number of samples collected.
[b] Calculated when n=3 or more.
[c] Calculated when n = 2.

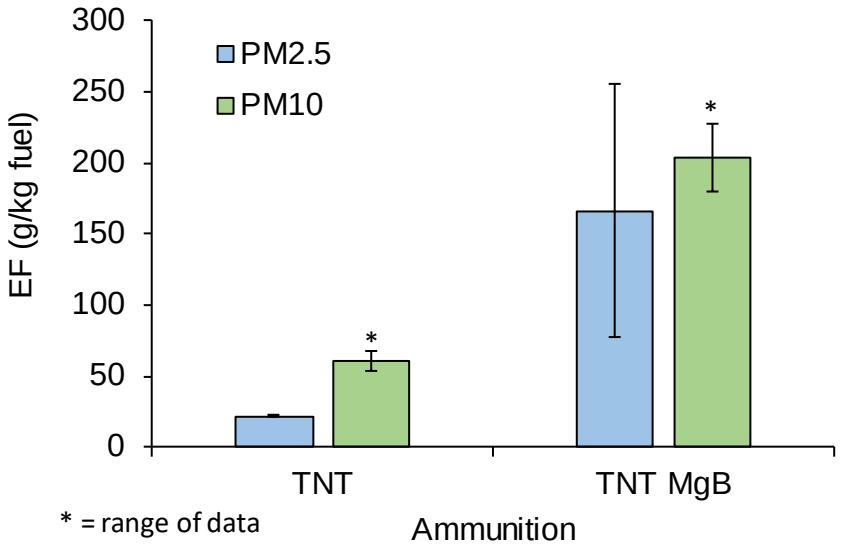

Fig. 41 PM EFs from TNT and TNT:Mg:B. Error bars represent one standard deviation if nothing else stated

3.5.3 Elements

Elemental emissions were found in collected particles. B was the most abundant element in particles from explosions of TNT:Mg:B (64.18±34.35 g/kg fuel) and considerably larger than for explosions of neat TNT (0.199±0.007 g/kg fuel) as shown in Fig. 42 and Tables 33 and 34. Figure 43 shows the element EFs in test order. The levels of Mg were also higher in the TNT:Mg:B plumes (5.20±2.48 g/kg fuel) than from the TNT plumes (0.034±0.014 g/kg fuel).

However, these Mg levels were low in most of the samples with levels less than three times the uncertainty of the analytical method. One of the three TNT tests was conducted after the TNT:Mg:B tests as a control to test for potential residual contamination of the facility. The levels of B and Mg in the last TNT plume sample were approximately 15 times higher than in the two TNT plumes conducted prior to the TNT:Mg:B tests, indicating contamination of chamber wall by previous tests. Fe levels were relatively high in all samples, most likely originating from the walls of the detonation chamber. This is most likely also true of other elements found in the collected plume samples.

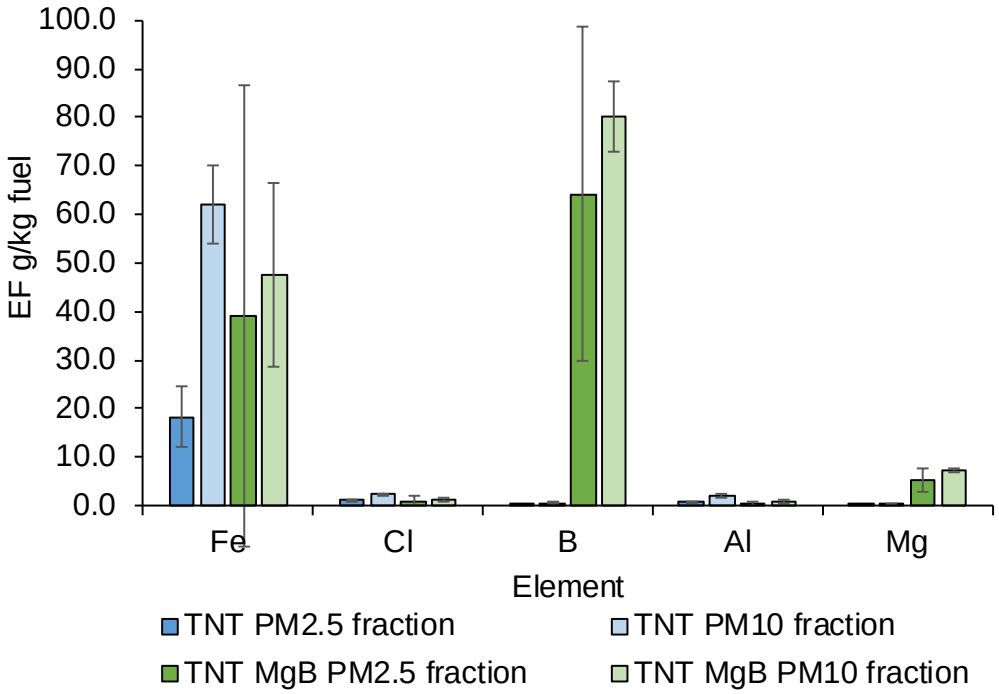

Fig. 42 Element EFs from detonation of TNT and TNT:Mg:B

Table 33 TNT element EFs

Metal	$PM_{2.5}$ n[a]	$PM_{2.5}$ Average g/kg fuel	$PM_{2.5}$ Stand. dev. g/kg fuel	$PM_{2.5}$ RSD[b] %	PM_{10} n[a]	PM_{10} Average g/kg fuel	PM_{10} RPD %
Fe	3	18.261	6.197	34	2	62.134	26
Cl	3	1.248	0.105	8.4	2	2.542	7.6
B	2	0.199	…	7.1	2	0.503	95
Al	3	0.750	0.198	26	2[d]	2.09	49
Cu	3	0.256	0.137	54	2	0.315	29
Mg	2[d]	0.034	…	86	2[e]	0.205	106
Mn	3	0.221	0.030	14	2	0.589	33
Zn	3	0.167	0.010	6.1	2	0.304	28
Ba	3	0.0482	0.0241	50	2	0.126	54
Ni	3	0.0460	0.0141	31	2	0.138	27
Sb	3	0.0427	0.0215	50	2	0.048	11
Cr	3	0.0345	0.0089	26	2	0.110	15
Pb	3	0.0197	0.0039	20	2	0.028	32
Bi	3	0.0114	0.0061	53	2[d]	0.015	79

[a] Number of samples collected.
[b] Calculated when n = 3 or more.
[c] Calculated when n=2.
[d] Some values were less than three times the uncertainty of the analytical method.
[e] All values were less than three times the uncertainty of the analytical method.

Table 34 TNT:Mg:B element EFs

Element	$PM_{2.5}$ n[a]	$PM_{2.5}$ Average g/kg fuel	$PM_{2.5}$ Stand. dev. g/kg fuel	$PM_{2.5}$ RSD[b] %	PM_{10} n[a]	PM_{10} Average g/kg fuel	PM_{10} RPD %
Fe	3	39.101	47.345	121	2	47.496	80
Cl	3	1.001	0.924	92	2	1.242	61
B	3	64.180	34.350	54	2	80.051	18
Al	3[d]	0.394	0.300	76	2[e]	0.84	68
Cu	3	0.169	0.135	80	2	0.243	40
Mg	3[d]	5.197	2.483	48	2[e]	7.331	11
Mn	3	0.321	0.364	113	2	0.421	72
Zn	3	0.197	0.142	72	2	0.271	30
Ba	3	0.1040	0.0872	84	2	0.113	69
Ni	3	0.0751	0.0833	111	2	0.105	67
Sb	3	0.0253	0.0159	63	2	0.038	57
Cr	3	0.0710	0.0892	126	2	0.084	94
Pb	3	0.0182	0.0126	69	2	0.027	4.0
Bi	2	0.0037		22[c]	2	0.002	113
		Average g/kg element in fuel	**Stand. dev**			**Average g/kg element in fuel**	
B	3	822.0	439.9	54	2	235.1	18
Mg	3[d]	66.6	31.8	48	2[e]	141.4	11

[a] Number of samples collected.
[b] Calculated when n=3 or more.
[c] Calculated when n = 2.
[d] Some values were less than three times the uncertainty of the analytical method.
[e] All values were less than three times the uncertainty of the analytical method.

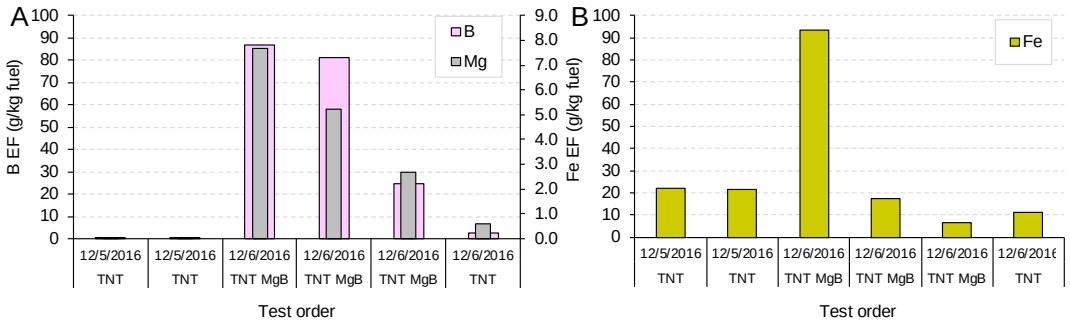

Fig. 43 B and Mg (graph A) and Fe (graph B) EFs in test order

3.5.4 VOCs

The most abundant VOC was methyl methacrylate followed by chloromethane and benzene from both TNT and TNT:Mg:B (80:4:16 by weight) (Table 35). The methyl methacrylate originates most probably from the PMMA centering device for the TNT cylinders. The benzene value from TNT (23.84 mg/kg fuel) was lower than previously found from OD of TNT sampled from an aerostat based sampling package (220 mg/kg fuel [Aurell et al. 2011]) and from an airplane (96 mg/kg fuel [US Army 1992]) during ODs but higher than from Bangbox testing of TNT (4.07 mg/kg [EPA 2009]). A VOC analysis on a TNT (only) test after the TNT:Mg:B testing was not done due to an insufficient number of canisters. Future tests should incorporate these test checks to ensure that observed reductions in VOCs (e.g., ethanol) are due to formulation changes rather than facility wall contamination from prior projects.

Table 35 VOC EFs from small-scale detonations of TNT and TNT:Mg:B (80:4:16 by weight)

VOC	TNT			TNT:Mg:B		
	n[b]	Average mg/kg fuel	RPD[c] %	n[b]	Average mg/kg fuel	RPD[c] %
Chloromethane[a]	2	35.44	1.4	2	27.35	33
Vinyl chloride[a]	2	11.84	46	2	9.56	21
1,3-Butadiene[a]	2	3.96	72	2	4.10	3.5
Bromomethane[a]	2	1.39	26	1	0.69	…
Chloroethane[a]	2	0.94	22	1	0.71	…
Ethanol	1	22.10	…	0	ND	…
Acetonitrile	2	18.13	33	2	12.71	31
Acrolein[a]	2	52.41	30	2	42.06	33
Acetone	1	23.14	…	0	ND	…
Trichlorofluoromethane	1	0.11	…	1	0.10	…
Acrylonitrile[a]	2	8.01	47	2	5.71	32
1,1-dichloroethene	2	0.53	18	0	ND	…
3-chloro-1-propene (allyl chloride) [a]	2	3.92	39	2	2.09	21
Carbon disulfide[a]	2	5.57	115	0	ND	…
Vinyl acetate[a]	2	2.63	30	0	ND	…
2-Butanone[a] (MEK)	2	2.08	17	2	1.81	19
Chloroform[a]	2	0.81	17	1	0.74	…
Tetrahydrofuran	2	0.60	28	0	ND	…
Benzene[a]	2	23.84	30	2	17.88	21
Carbon tetrachloride[a]	2	0.58	12	1	0.50	…
Trichloroethene	1	0.36	…	1	0.34	…
Methyl methacrylate[a]	2	1,597	17	2	1,675	14
2-Hexanone	2	0.48	30	0	ND	…
Chlorobenzene[a]	2	1.93	48	2	1.34	27
Styrene[a]	1	5.88	…	2	4.48	168
Benzyl chloride[a]	2	0.69	55	1	0.47	…

[a] On EPA's list of hazardous air pollutants.
[b] Number of samples with detectable levels.
[c] Calculated when n=2.

3.5.5 Energetics

Detectable levels of HMX and RDX were found from both TNT and TNT:Mg:B. TNT:Mg:B also showed detectable levels of the base explosive TNT—indicating some of the material did not react. Previous Bangbox (EPA 2009) studies showed no detectable levels of energetics from TNT while TNT and dinitrotoluene were found in the plumes of OD of TNT (EPA 2009). It is also conceivable that some of the detected RDX/HMX came from the chamber walls.

3.5.6 PAHs

Fourteen of the 16 EPA PAHs were detected (Table 36). No statistical difference was found between TNT and TNT:Mg:B ($p = 0.14$, $F = 0.4$), although the statistical analysis is based on only two replicates for the TNT (three or more replicates are

preferred). The TNT EFs for PAHs in this study were on average 3.4 and 2.5 times lower than previously found EFs from OD of TNT sampled using an aerostat (Aurell et al. 2011) and airplane (US Army 1992), respectively (Fig. 44 and Table 37) . This may be due to the significant difference in charge size (~0.8 kg here vs. 45 kg with the aerostat [EPA 2014b]).

Table 36 Energetics EFs from small-scale detonations of TNT and TNT:Mg:B (80:4:16 by weight)

Energetic	TNT mg/kg fuel	TNT:Mg:B mg/kg fuel
1,3,5-trinitrobenzene	<5.61	<4.47
1,3-dinitrobenzene	<5.61	<4.47
2,4,6-trinitrotoluene	<5.61	2.97 (35%)[a]
2,4-dinitrotoluene	<5.61	<4.47
2,6-dinitrotoluene	<5.61	<4.47
2-amino-4,6-dinitrotoluene	<5.61	<4.47
2-nitrotoluene	<5.61	<4.47
3,5-DNA	<5.61	<4.47
3-nitrotoluene	<5.61	<4.47
4-amino-2,6-dinitrotoluene	<5.61	<4.47
4-nitrotoluene	<5.61	<4.47
HMX	20.95 (46%)[a]	6.19 (56%)[a]
Nitrobenzene	<5.61	<4.47
NG	<5.61	<4.47
PETN	<14.03	<11.17
RDX	46.35 (42%)[a]	9.79±4.18[b] (43%)[c]
Tetryl	<5.61	<4.47

[a] Relative percent difference.
[b] One standard deviation.
[c] Relative standard deviation.

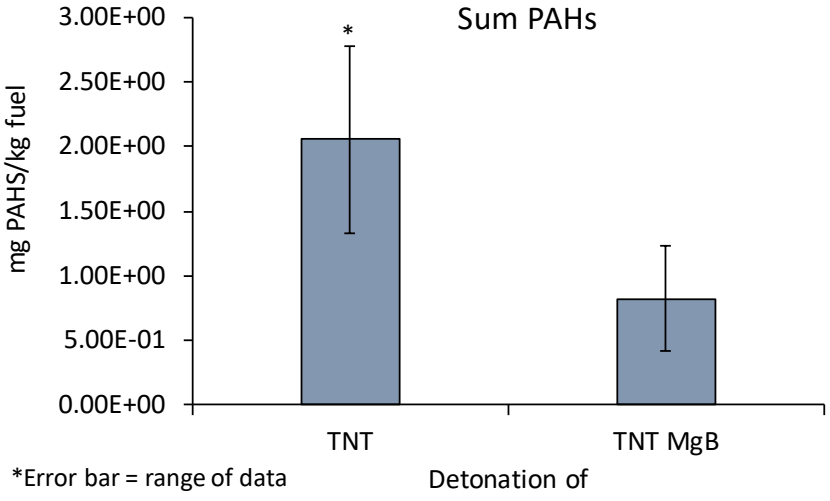

Fig. 44 PAH EFs from detonation of TNT and TNT:Mg:B. Error bars represents one standard deviation

Table 37 PAH EFs from small-scale detonations of TNT and TNT:Mg:B (80:4:16 by weight)

Targets	TNT			TNT:Mg:B				
	n = 2	n = 2	RPD	n = 3	STDV	n = 3	STDV	RSD
	mg/kg fuel	mg B[a]P TEQ/kg fuel	%	mg/kg fuel		mg B[a]P TEQ/kg fuel		%
Naphthalene	1.08E+00	NA[a]	68	4.88E-01	2.64E-01	NA[a]	NA[a]	54
Acenaphthylene	5.17E-02	NA[a]	104	1.30E-02	5.65E-03	NA[a]	NA	43
Acenaphthene	ND	NA[a]	NA[a]	ND	NA[a]	NA[a]	NA[a]	NA[a]
Fluorene	ND	NA[a]	NA[a]	ND	NA[a]	NA[a]	NA[a]	NA[a]
Phenanthrene	3.97E-01	1.99E-04	93	1.59E-01	6.79E-02	7.97E-05	3.39E-05	43
Anthracene	3.97E-02	1.98E-05	13	1.10E-02	4.67E-03	5.50E-06	2.33E-06	42
Fluoranthene	1.54E-01	7.72E-03	72	4.50E-02	2.06E-02	2.25E-03	1.03E-03	46
Pyrene	1.05E-01	1.05E-04	66	2.41E-02	1.16E-02	2.41E-05	1.16E-05	48
Benzo(a)anthracene	2.97E-02	1.49E-04	50	7.24E-03	3.16E-03	3.62E-05	1.58E-05	44
Chrysene	6.74E-02	2.02E-03	62	1.95E-02	1.09E-02	5.85E-04	3.27E-04	56
Benzo(b)fluoranthene	4.14E-02	4.14E-03	46	2.39E-02	6.16E-03	2.39E-03	6.16E-04	26
Benzo(k)fluoranthene	3.17E-02	1.59E-03	57	6.80E-03	3.51E-03	3.40E-04	1.75E-04	52
Benzo(a)pyrene	1.46E-02	1.46E-02	18	ND	NA	ND	NA	NA
Indeno(1,2,3-cd)pyrene	1.95E-02	1.95E-03	8	1.01E-02	3.42E-03	1.01E-03	3.42E-04	34
Dibenz(a,h)anthracene	5.06E-03[a]	2.78E-03[b]	NA[a]	4.50E-03	3.21E-03	4.95E-03	3.53E-03	71
Benzo(ghi)perylene	2.12E-02	4.25E-04	3	8.86E-03	2.61E-03	1.77E-04	5.22E-05	29
SUM 16-EPA PAHs	2.06E+00	3.57E-02	70	8.22E-01	4.06E-01	1.18E-02	6.12E-03	49

[a] Naphthalene, acenaphthylene, acenaphthene, and fluorene have not been assigned a toxic equivalent number. n = 1

3.5.7 Particle Size Distributions

The initial normalized mass weighted size distribution of the emissions from detonations are shown in Fig. 45. The mass weighted particle size distributions for both detonations extended above the range of the ELPI, which was limited to particles less than 6 µm. The number distributions (Fig. 46) were within the instrument range and exhibited a lognormal shape. The TNT detonation exhibited a bimodal distribution with the first peak appearing below the range of the ELPI (<0.02 µm) and a second peak at 0.63 µm. The TNT:Mg:B detonation exhibited a trimodal distribution with a peak at approximately 0.04, 0.11, and 0.53 µm. The larger-size modes dominate the mass distribution and result in a mass median diameter of 4.3 µm for the TNT:Mg:B detonation and 1.4 µm for the TNT detonation. These mass weighted particle size distribution are consistent with the filter results showing larger PM_{10} EFs as compared to $PM_{2.5}$.

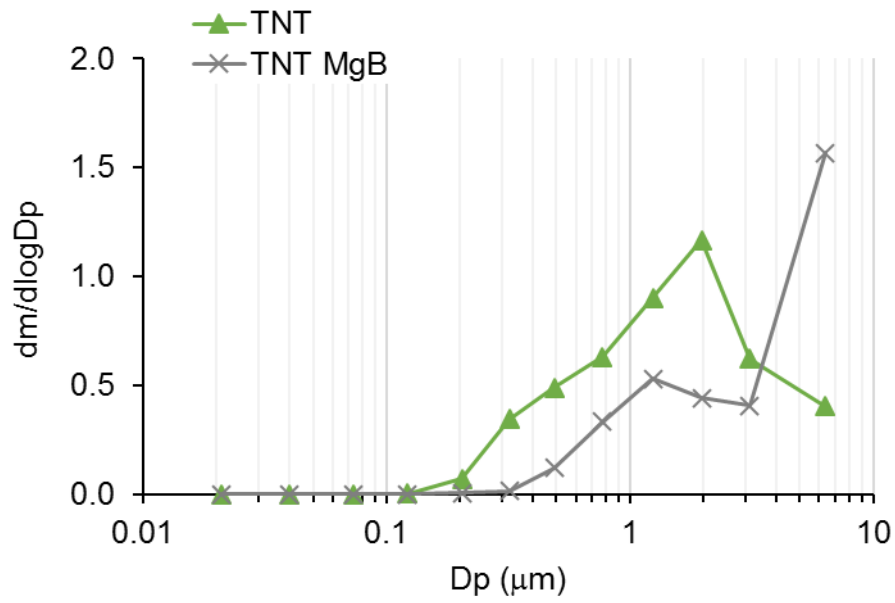

Fig. 45 Representative initial mass normalized mass weighted PM size distributions for detonations

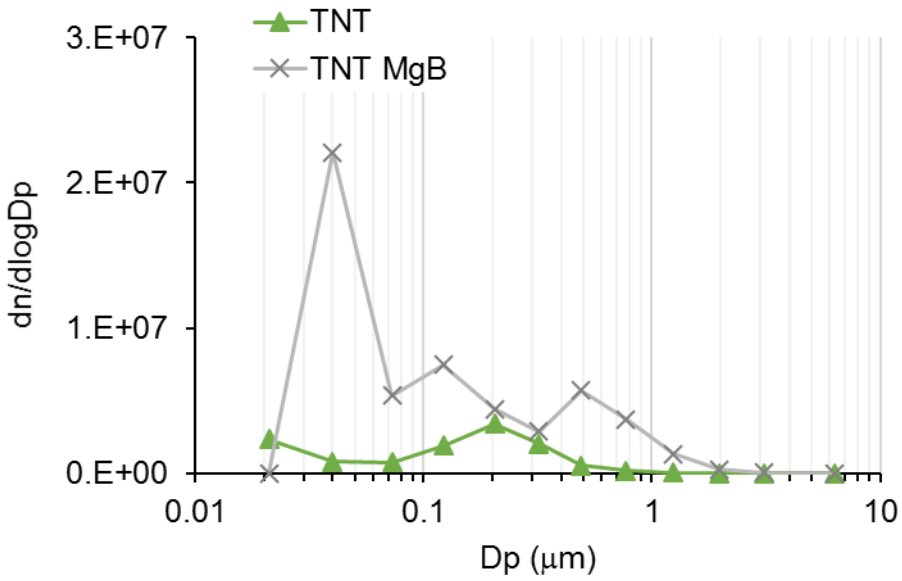

Fig. 46 Normalized number weighted PM size distributions corresponding to mass weighted size distributions in Fig. 45

The initial size distribution evolved over the first minute as the particles aggregated causing a shift toward larger diameter particles (Fig. 47). The smaller-size modes decreased in number concentration as the larger-size modes increased until eventually the aerosol was just a single large mode.

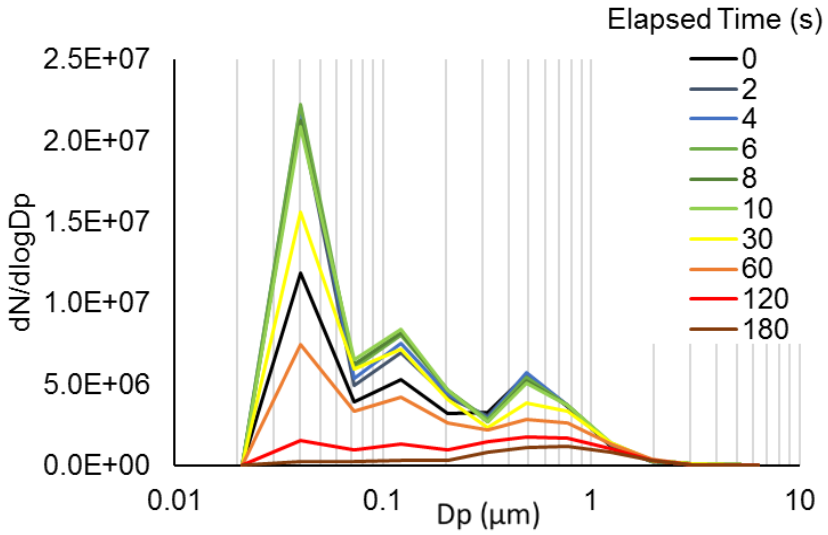

Fig. 47 PM number distributions from TNT:Mg:B detonation over the first 3 min after the blast

The color ratio of incandescing particles emitted from detonations is shown in Fig. 48. The color ratio for TNT detonations had a bimodal distribution, indicating that two different incandescing particle types were present in the emissions. The TNT:Mg:B detonation had a single mode distribution. As with the gun blasts, these results suggest that the SP2 color ratio may be used for some emissions to distinguish between particles of different composition, although further study is needed.

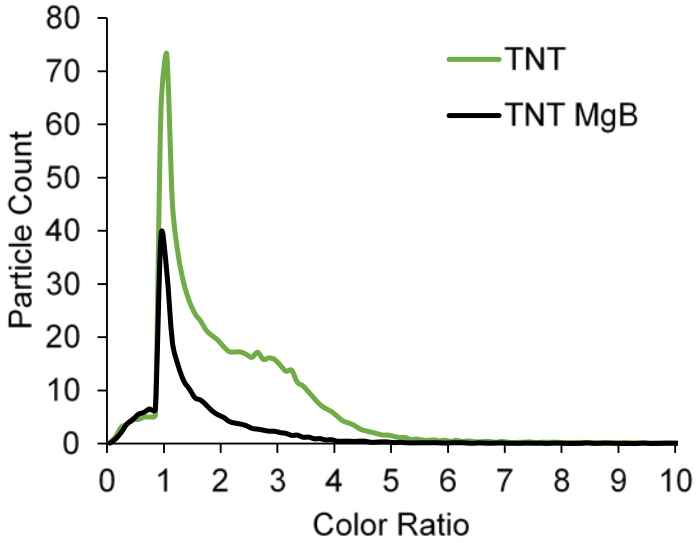

Fig. 48 Color ratio for incandescing particles in the emissions from TNT and TNT:Mg:B detonations

3.6 Discussion

Tables 38 and 39 summarize simulation and measurement of EFs and MCEs for detonation/explosions of TNT and TNT:Mg:B (80:4:16 by weight). In general, there is reasonable agreement between experiment and simulation values for MCE (approximately 14% to 27%), with the largest error for the B active simulation. We believe the main source of error between simulation and experiment, for the present work, is our inability to include heterogeneous combustion (i.e., burning of particles) in the CHEMKIN calculations. Since the CHEETAH calculations predict up to 0.35-mole fraction graphitic carbon for detonations of TNT, this is a source of nonreactive carbon, lowering the simulated MCE relative to the measured value.

Table 38 MCE for detonation/explosion of TNT and TNT:Mg:B (80:4:16 by weight) with B inactive and active, simulated and measured

Type	MCE
TNT	0.98 (0.66)
TNT:Mg:B	0.979 (0.35)
TNT simulation	0.866
TNT:Mg:B (B inactive) simulation	0.74
TNT:Mg:B (B active) simulation	0.71

Table 39 EFs for detonation/explosion of TNT and TNT:Mg:B (80:4:16 by weight) with B inactive and active, simulated and measured

	TNT			TNT:Mg:B			TNT simulated	TNT:Mg:B simulated B inactive	TNT:Mg:B simulated B active
Compound	n[a]	Average g/kg fuel	RPD[b] %	n[a]	Average g/kg fuel	RPD[b] %	g/kg fuel	g/kg fuel	g/kg fuel
CO_2	2	1,314	0.65	2	1,117	1.5	1,170	803	860
CO	2	17	32	1	15	16	5	0.26	0.14
CH_4	2	ND	NA	2	0.16	NA	trace	trace	trace

[a] Number of samples collected.
[b] Calculated when n = 2.

This is also evident in the measured and predicted EFs for CO_2. If the CHEMKIN calculations included heterogeneous combustion (i.e., if particle combustion was included), we believe that the CHEMKIN simulation will provide a good estimate of the afterburn occurring in the blast chamber.

4. Conclusions, Recommendations, and Implications for Future Research

This work has demonstrated simulation approaches and experimental methodologies for comprehensive estimation and sampling of emissions from metal-based energetics under conditions that simulate potential warfighter exposure. Simulations used an approach based on verified stages of energy release. Tests firing an M4 carbine and detonating metallized TNT charges examined the effect of propellant and explosive formulations on emissions. Emphasis was placed on a comprehensive array of samplers to determine emission characterization, repeatability, and an ability to discern effects of changing metal formulations. Measurement technologies were successful, resulting in high precision between replicates and comparable values with the limited available field data. Where available, measured EFs compared well with simulation and previous studies, either by this group or elsewhere. EFs determined from this work can be used in activity models to determine warfighter exposure.

4.1 M4

Emissions from the M4 carbine firing M855 ammunition exhibited average CO concentrations around 1500 ppm after firing, suggesting that inhalation studies on firing ranges may be warranted. Emitted particles had mass median diameters between 0.389 and 0.575 µm, a respirable particle size. With particle agglomeration, these sizes increase but are still less than 2 µm after 120 s. Three different round types were tested; differences in PM EFs could be observed due to the low relative standard deviation (10%), indicating the precision of the method. PM was highest from the 855 salted round, likely due to incomplete secondary combustion in the muzzle blast, caused by addition of K to scavenge combustion radicals. Cu was the metal observed in highest concentration for all three round formulations; it originated from the Cu jacket on the bullet. More than 100% of the Pb in the propellant formulations was observed to be emitted for all three round types. This could be due to contributions by the Cu-jacketed Pb slug, and to combined error of sampling and the determination of the formula composition. The same issue was observed for Bi on all but the legacy rounds. The methodology for sampling volatile organic compounds successfully detected residual gases from the initial fracturing of the PMMA M4 carbine chamber and the glass cleaner used to clean the box interior between shots. No residual energetics were detected at levels typically less than 19.8 mg/round.

Simulations of EFs provided reasonable results, and in all cases, differed from experimental measurements by a maximum of a factor of two. For the NASA-Lewis

based simulation, predicted MCE differed from measured MCE by approximately 30% (0.732 predicted vs. 0.5 measured for salted rounds). We believe that improved estimates of EFs for chemical species during M4 weapon firing will result from the combination of accurate flow dynamics, improved IB thermodynamic calculations, with incorporation of a CHEMKIN mechanism to simulate muzzle flash. We believe this report makes a reasonable case to continue this effort along those lines, combining experimental evidence with modeling predictions.

4.2 TNT

Emissions from the TNT detonations indicated combustion efficiencies of about 98%. Comparison of PM EFs show that our laboratory results, while consistent with others, are half that of our field values, likely due to detonations in the field entraining sandy soil. The addition of Mg:B to the TNT formulations significantly increased the $PM_{2.5}$ emission by a factor of 8. As expected, Pb EFs are unaffected by the presence of Mg:B; EFs only differed by 4%—in fact, Pb may be coming from blast chamber walls, as there was no Pb in the explosive train, including the RP-80 detonator. The sensitivity of the VOC sampling was again observed through detection of PMMA from the TNT cylinder centering device. Residual TNT, HMX, and RDX were detected.

The simulation of emission factors using a combination of thermodynamic calculations for detonation (CHEETAH) and chemical kinetics (CHEMKIN) for afterburn produced results in reasonable agreement with experimental measurement (0.865 predicted vs. 0.997 measured). We believe this shows that the approach of using observed stages of energy release during and following detonation of solid explosives as a guide to simulation is acceptable when full CFD with detailed finite-rate chemistry is not available. It is worth noting that performing the experiments in a blast chamber is advantageous as the transit of the shock wave back and forth within the chamber, following detonation, provides mixing approximating the homogeneous reactor used in the CHEMKIN calculations. Finally, the need to incorporate finite-rate CHEMKIN for heterogeneous mixtures would be a welcome addition to any future effort.

4.3 Recommendations/Implications for Future Research

- The high levels of CO and respirable PM emitted from the M4 carbine warrant additional sampling and analysis on outdoor and indoor range environments.

- The sampling methods should be extended to assess emissions from the carbine breech due to its proximity to the user and greater inhalation likelihood
- The analytical methods employed were sufficiently sensitive to detect residual chemicals unrelated to the test formulations. Care should be taken to document cleaning formulas and prior testing formulations. Time-series background analyses should be done prior to test formulation changes to determine potential residual carry over. Indoor results should be compared with outdoor range results to verify carry over and wall effects.
- Ground-deposited residuals should be sampled concurrently with emissions to assess potential range contamination issues.
- Compositional analyses of the formulations should be determined prior to testing to ensure that trace variations in components are properly accounted.
- Finite-rate CHEMKIN should be incorporated with improved estimates of temperature and the inclusion of heat loss.
- Investigations of NASA-Lewis (NASA-Glenn) simulations with soot production during the IB cycle should be expanded.

5. References

AMCCOM. Development of methodology and technology for identifying and quantifying emission products from open burning and open detonation thermal treatment methods. In: Proceedings of the Technical Steering Committee Symposium; 1988 July 6–8; Salt Lake City, UT; Armament Munitions & Chemical Command, Rock Island, IL.

AMCCOM. Development of methodology and techniques for identifying and quantifying products from open burning and open detonation thermal treatment methods-field test series a, b and c, vol. 1, test summary. Rock Island (IL): Armament Munitions & Chemical Command; 1992 Jan.

Appel J, Bockhorn H, Frenklach MY. Kinetic modeling of soot formation with detailed chemistry and physics: laminar premixed flames of C_2 hydrocarbons. Combust Flame. 2000;121:122–136.

Burling IR, Yokelson RJ, Griffith DWT, Johnson TJ, Veres P, Roberts JM, Warneke C, Urbanski SP, Reardon J, Weise DR, Hao WM, de Gouw J. Laboratory measurements of trace gas emissions from biomass burning of fuel types from the southeastern and southwestern United States. Atmos Chem Phys. 2010;10:11115–11130.

Cooper PW. Explosives engineering. New York (NY): Wiley-VCH Inc.; 1996.

Davini P, Ghetti P, Bonfanti L, De Michele G. Investigation of the combustion of particles of coal. Fuel. 1996 July;75(9):1083–1088.

Davis WC, Salyer TR, Jackson SI, Aslam TD. Explosive driven shock waves in argon. In Proceedings of the 13th International Detonation Symposium; 2006; The Office of Naval Research, US Navy; p. 1035–1044.

Dreizin EL, Keil DG, Felder W, Vicenzi EP. Phase changes in boron ignition and combustion. Combust Flame. 1999;119:272–290.

EPA 40 CRF Part 50. National primary and secondary ambient air quality standards. Appendix J. Reference method for determination of particulate matter as PM_{10} in the atmosphere. Washington (DC): Environmental Protection Agency (US); 2014a [accessed 2016 Nov 22]. https://www.gpo.gov/fdsys/pkg/CFR-2014-title40-vol2/pdf/CFR-2014-title40-vol2-part50-appJ.pdf.

EPA 40 CRF Part 50. National primary and secondary ambient air quality standards. Appendix L. Reference method for the determination of particulate

matter as $PM_{2.5}$ in the atmosphere. Washington (DC): Environmental Protection Agency (US); 2014b [accessed 2016 Nov 22]. https://www.gpo.gov/fdsys/pkg/CFR-2014-title40-vol2/pdf/CFR-2014-title40-vol2-part50-appL.pdf.

EPA AP-42. Compilation of emission factors. Washington (DC): Environmental Protection Agency (US); 2009. Draft Chapter 16. Emission factors for demilitarization processes: open burning and open air detonation.

EPA Com13214852pendium Method IO-3.3. Determination of metals in ambient particulate matter using X-ray fluorescence (XRF) spectroscopy. Washington (DC): Environmental Protection Agency (US); 1999a [accessed 2014 May 5]. http://www.epa.gov/ttnamti1/files/ambient/inorganic/mthd-3-3.pdf.

EPA Compendium Method IO-3.4. Determination of metals in ambient particulate matter using inductively coupled plasma (ICP) spectroscopy. Washington (DC): Environmental Protection Agency (US); 1999b [accessed 2014 May 5]. http://www.epa.gov/ttn/amtic/files/ambient/inorganic/mthd-3-4.pdf.

EPA Compendium Method TO-15. Determination of volatile organic compounds (VOCs) in air collected in specially-prepared canisters and analyzed by gas chromatography/mass spectrometry (GC/MS). Washington (DC): Environmental Protection Agency (US); 1999c [accessed 2015 Nov 10]. http://www.epa.gov/ttnamti1/files/ambient/airtox/to-15r.pdf.

EPA Compendium Method TO-9A. Determination of polychlorinated, polybrominated and brominated/chlorinated dibenzo-p-dioxins and dibenzofurans in ambient air. Washington (DC): Environmental Protection Agency (US); 1999d [accessed 2012 Nov 21]. http://www .epa.gov/ttnamti1/files/ambient/airtox/to-9arr.pdf.

EPA Method 25C. Determination of nonmethane organic compounds (NMOC) in landfill gases. Washington (DC): Environmental Protection Agency (US); 2017 Aug 2 [accessed 2016 May 11]. https://www.epa.gov/emc/method-25c-nonmethane-organic-compounds-landfill-gases.

EPA Method 353.2. Determination of nitrate-nitrite nitrogen by automated colorimetry. Washington (DC): Environmental Protection Agency (US); 1993 [accessed 2016 July 18]. https://www.epa.gov/sites/production/files/2015-08/documents/method_353-2_1993.pdf.

EPA Method 3A. Determination of oxygen and carbon dioxide concentrations in emissions from stationary sources (instrumental analyzer procedure).

Washington (DC): Environmental Protection Agency (US); 1989 [accessed 2014 May 5]. http://www.epa.gov/ttn/emc/promgate/m-03a.pdf.

EPA Method 8330B. Nitroaromatics, nitramines, and nitrate esters by high performance liquid chromatograph (HPLC). Washington (DC): Environmental Protection Agency (US); 2006 [accessed 2016 July 18]. https://www.epa.gov/sites/production/files/2015-07/documents/epa-8330b.pdf.

Frost DL, Goroshin S, Levin J, Ripley R, Zhang F. Critical conditions for ignition of metal particles in a condensed explosive. In Proceedings of 12th International Detonation Symposium; 2002; San Diego (CA); Office of Naval Research, Arlington, VA, p. 693–701.

Glassman I. Combustion. 2nd ed. San Diego (CA): Academic Press; 1987. p. 360–375.

Glumac N. Early time spectroscopic measurements during high-explosive detonation breakout into air. Shock Waves. 2013;23:131–138.

Gordan S, McBride BJ. Computer program for calculation of complex chemical equilibrium compositions and applications. Cleveland (OH): NASA-Glenn. 1994 Oct. Report No.: 1311.

Horst AW, Nusca MJ. The charge designer's workbench: a range of interior ballistic modeling tools. Aberdeen Proving Ground (MD): Army Research Laboratory (US); 2006 May. Report No.: ARL-TR-3796

Johansson CH, Persson PA, editors. Detonics of high explosives. New York (NY): Academic Press Inc.; 1970.

Jones RN, Hitchcock HP, Villegas DR. Engineering design handbook ballistics series - interior ballistics of guns. Washington (DC): Headquarters, Army Materiel Command (US); 1965 Feb. Report No.: AMCP 706-150.

Kim K. Thermobarics: promises, challenges and recommendations. 7th Joint Classified Bombs/Warheads and Ballistics Symposium; 2004 Aug 9–12; Monterey (CA).

Kinney GF, Graham KJ. Explosive shocks in air. 2nd ed. Berlin (Germany): Springer-Verlag; 1985.

Kirchner DB, Gaydos JC, Battigelli MC. Combustion products of propellants and ammunition. In Occupational health: the soldier and the industrial base. Aberdeen Proving Ground (MD): Office of the Surgeon General, Department of the Army (US); Bethesda (MD): Army Environmental Hygiene Agency

(US); Washington (DC): Uniformed Services University of the Health Sciences; 1993.

Kistiakowski GB, Wilson EB. The prediction of detonation velocities of solid explosives. Washington (DC): Office of Scientific Research and Development; 1941 Jan 17. Report No.: OSRD No. 69, Serial No. 6.

Kotlar AJ. The thermodynamics of interior ballistics and propellant performance. Proceedings 29th JANNAF Combustion Meeting; 1992 Oct; CPIA Publication 593.

Kuhl AL, Forbes J, Chandler J, Oppenheim AK, Spektor R, Ferguson RE. Confined combustion of TNT explosion products in air. In Proceedings of the 8th International Colloquium on Dust Explosions; 1998 Sep 21–25; Schaumberg, IL.

Kuo KK, Acharya R. Ignition and combustion of single energetic solid particles. New York (NY): John Wiley and Sons, Inc.; 2012.

Larsen JC, Larsen PB. Chemical carcinogens. In: Air Pollution and Health. Cambridge (UK): The Royal Society of Chemistry; 1998. p. 33–56.

[LLNL] CHEETAH 6.0 user's manual. Livermore (CA): Lawrence Livermore National Security; 2010. Report No.: LLNL-SM-416166.

Mader CL. Numerical modeling of explosives and propellants. 3rd ed. Boca Raton (FL): CRC Press; 2008.

McNesby KL, Homan BE, Benjamin RA, Boyle VM, Densmore JM, Biss MM. Quantitative imaging of explosions with high-speed cameras. Review of Scientific Instruments. 2016;87:051301.

McNesby KL, Homan BE, Lottero RE. High brightness imaging for real time measurement of shock, particle, and combustion fronts produced by enhanced blast explosives. Aberdeen Proving Ground (MD): Army Research Laboratory (US); 2005 Jan. Report No.: ARL-TR-3411.

McNesby KL, Homan BE, Ritter JJ, Quine Z, Ehlers RZ, McAndrew BA. Afterburn ignition delay and shock augmentation in fuel rich solid explosives. Propellants, Explos, Pyrotech. 2010;35(1):57–65.

Menon S, Sankaran V, Stone C. Subgrid combustion modeling for the next generation national combustion code. Cleveland (OH): National Aeronautics and Space Administration; 2003; Report No.: NASA/CR—2003-212202.

Meyer R, Kohler J, Homburg IA. Explosives. 6th ed. Berlin (Germany): John Wiley and Sons, Wiley-VCH Verlag GmbH and Co; 2007.

Mitchell WJ, Suggs JC. Emission factors for the disposal of energetic materials by open burning and open detonation (OB/OD). Washington (DC): Environmental Protection Agency (US); 1998. Report No.: EPA/600/R-98/103.

Montgomery CJ, Cremer MA, Heap MP, Chen J-Y, Westbrook CK, Maurice LQ. Reduced chemical kinetic mechanisms for hydrocarbon fuels. LLNL Report UCRL-JC-136815; Published in Proceedings of 35th American Institute of Aeronautics and Astronautics/Association for the Study of Medical Education/American Society for Engineering Education Society of Automotive Engineers Joint Propulsion Conference and Exhibit; 1999 June 20–24; Los Angeles, CA.

Nusca MJ. Recent upgrades to the ARL-NGEN3 computational interior ballistics model. Aberdeen Proving Ground (MD): Army Research Laboratory (US); 2011 Aug. Report No.: ARL-TR-5613.

Nusca M, McNesby K, Biss M. Muzzle pressure management. In: Ciezak-Jenkins J, editor. Disruptive energetics and propulsion technologies: FY15 annual report. Aberdeen Proving Ground (MD): Army Research Laboratory (US); 2016 Feb. Report No.: ARL-SR-0325.

Rankine WJM. On the thermodynamic theory of waves of finite longitudinal disturbances. Philosophical Transactions of the Royal Society of London. 1870;160:277–288.

Schmidt JR, Nusca MJ. Progress toward a multi-dimensional representation of the 5.56-mm interior ballistics. Aberdeen Proving Ground (MD): Army Research Laboratory (US); 2009 Aug. Report No.: ARL-TR-4903.

Sinha P, Hobbs PV, Yokelson RJ, Bertschi IT, Blake DR, Simpson IJ, Gao S, Kirchstetter TW, Novakov T. Emissions of trace gases and particles from savanna fires in southern Africa. J Geophys Res. 2003;108:8487. doi:10.1029/2002JD002325.

Smith GP, Golden DM, Frenklach M, Moriarty NW, Eiteneer B, Goldenberg M, Bowman T, Hanson RK, Song S, Gardiner Jr WC, Lissianski VV, Qin Z. GRI-Mech home page; 2014 [accessed 2018]. http://www.me.berkeley.edu/gri_mech/.

Spadaccini LJ, Colket MB III. Ignition delay characteristics of methane fuels. Prog Energy Combust Sci. 1994;20:431.

Tomlin AS, Tur´anyi T, Pilling MJ. Mathematical tools for the construction, investigation and reduction of combustion mechanisms. In Low temperature combustion and autoignition. Amsterdam (The Netherlands): Elsevier; 1997. p. 293.437 (Comprehensive Chemical Kinetics, vol. 35).

Ward DE, Radke LF. Emissions measurements from vegetation fires: a comparative evaluation of methods and results. In: Crutzen PJ, Goldammer JG, editors. Fire in the environment: the ecological, atmospheric, and climatic importance of vegetation fires. New York (NY): John Wiley; 1993. p. 53–76.

Windex. Racine (WI): SC Johnson & Son Inc.; 2017 [accessed 2018]. http://www.whatsinsidescjohnson.com/us/en/brands/windex/windex-Original-Glass-Cleaner.

Wingfors H, Svensson K, Hagglund L, Hedenstierna S, Magnusson R. Emission factors for gases and particle-bound substances produced by firing lead-free small-caliber ammunition. J Occup Environ Hyg. 2014;11:282–291.

Yeh CL, Kuo KK. Ignition and combustion of boron particles. Prog Energy Combust Sci. 1996;22:511–541.

Appendix A. Reduced Mechanism for Combustion of Trinitrotoluene (TNT) Detonation Products

Reduced chemical mechanism (chemical kinetics [CHEMKIN] format) for combustion of the anaerobic detonation products of trinitrotoluene (TNT) at freeze out (1,800 K):

```
ELEMENTS
O  H  C  N
END
SPECIES
H2
H
O
O2
OH
H2O
HO2
H2O2
C
CH
CH2
CH2*
CH3
CH4
CO
CO2
HCO
CH2O
CH2OH
CH3O
CH3OH
C2H2
C2H3
C2H4
C2H5
C2H6
HCCO
CH2CO
C2H3O
N2
CH3O2
CH3OCH3
CH3OCH2
N
NO
A4
!C(B)
END
REACTIONS
 H+O2 = O+OH                      8.300E+13    0.000  14413.00
 O+H2 = H+OH                      5.000E+04    2.670   6290.00
 OH+H2 = H+H2O                   2.160E+08    1.510   3430.00
```

```
 OH+OH = O+H2O                  3.570E+04    2.400  -2110.00
 H+H+M = H2+M                   1.000E+18   -1.000      0.00
   H2/0.0/ H2O/0.0/ CH4/2.0/ CO2/0.0/ C2H6/3.00/
 H+H+H2O = H2+H2O               6.000E+19   -1.250      0.00
 H+OH+M = H2O+M                 2.200E+22   -2.000      0.00
   H2/0.73/ H2O/3.65/ CH4/2.0/ C2H6/3.0/
 H+O2+M = HO2+M                 2.800E+18   -0.860      0.00
   O2/0.0/ H2O/0.0/ CO/0.75/ CO2/1.5/ C2H6/1.5/ N2/0.0/
 H+O2+H2O = HO2+H2O             9.380E+18   -0.760      0.00
 H+O2+N2 = HO2+N2               3.750E+20   -1.720      0.00
 OH+OH(+M) = H2O2(+M)           7.400E+13   -0.370  0.00
      LOW  /  2.300E+18   -0.900  -1700.00/
      TROE/  0.7346   94.00  1756.00  5182.00 /
   H2/2.0/ H2O/6.0/ CH4/2.0/ CO/1.5/ CO2/2.0/ C2H6/3.0/
 HO2+H = O+H2O                  3.970E+12    0.000    671.00
 HO2+H = O2+H2                  2.800E+13    0.000   1068.00
 HO2+H = OH+OH                  1.340E+14    0.000    635.00
 HO2+O = OH+O2                  2.000E+13    0.000      0.00
 HO2+OH = O2+H2O                2.900E+13    0.000   -500.00
 HO2+HO2 = O2+H2O2              1.300E+11    0.000  -1630.00
  DUPLICATE
 HO2+HO2 = O2+H2O2              4.200E+14    0.000  12000.00
  DUPLICATE
 H2O2+OH = HO2+H2O              5.800E+14    0.000   9560.00
 CO+O+M = CO2+M                 6.020E+14    0.000   3000.00
  H2/2.0/   O2/6.0/   H2O/6.0/   CH4/2.0/   CO/1.5/   CO2/3.5/
C2H6/3.0/
 CO+OH = CO2+H                  4.760E+07    1.228     70.00
 CO+O2 = CO2+O                  2.500E+12    0.000  47800.00
 CO+HO2 = CO2+OH                1.500E+14    0.000  23600.00
 C+O2 = CO+O                    5.800E+13    0.000    576.00
 CH+H = C+H2                    1.100E+14    0.000      0.00
 CH+H2 = CH2+H                  1.107E+08    1.790   1670.00
 CH+O2 = HCO+O                  3.300E+13    0.000      0.00
 HCO+H = CO+H2                  7.340E+13    0.000      0.00
 HCO+OH = CO+H2O                5.000E+13    0.000      0.00
 HCO+M = CO+H+M                 1.870E+17   -1.000  17000.00
    H2/2.0/ H2O/12.0/ CH4/2.0/ CO/1.5/ CO2/2.0/ C2H6/3.0/
 HCO+O2 = CO+HO2                7.600E+12    0.000    400.00
 CH2+O = HCO+H                  8.000E+13    0.000      0.00
 CH2+OH = CH2O+H                2.000E+13    0.000      0.00
 CH2+O2 = CO2+H+H               1.320E+13    0.000   1500.00
 CH2*+N2 = CH2+N2             1.500E+13    0.000    600.00
 CH2*+O2 = H+OH+CO            2.800E+13    0.000      0.00
 CH2*+O2 = CO+H2O             1.200E+13    0.000      0.00
 CH2*+CO = CH2+CO             9.000E+12    0.000      0.00
 CH2*+CO2 = CH2O+CO           1.400E+13    0.000      0.00
 CH2O+H(+M) = CH3O(+M)          5.400E+11    0.454   2600.00
      LOW  /  2.200E+30   -4.800   5560.00/
      TROE/  0.7580   94.00  1555.00  4200.00 /
    H2/2.0/ H2O/6.0/ CH4/2.0/ CO/1.5/ CO2/2.0/ C2H6/3.0/
 CH2O+H = HCO+H2                2.300E+10    1.050   3275.00
```

```
CH2O+O = HCO+OH                  3.900E+13    0.000   3540.00
CH2O+OH = HCO+H2O                3.430E+09    1.180   -447.00
CH3+H(+M) = CH4(+M)              1.270E+16   -0.630    383.00
    LOW  /  2.477E+33   -4.760   2440.00/
    TROE/  0.7830   74.00  2941.00  6964.00 /
   H2/2.0/ H2O/6.0/ CH4/2.0/ CO/1.5/ CO2/2.0/ C2H6/3.0/
CH3+O = CH2O+H                   8.430E+13    0.000      0.00
CH3+OH(+M) = CH3OH(+M)           6.300E+13    0.000      0.00
     LOW  /  2.700E+38   -6.300   3100.00/
     TROE/  0.2105   83.50  5398.00  8370.00 /
   H2/2.0/ H2O/6.0/ CH4/2.0/ CO/1.5/ CO2/2.0/ C2H6/3.0/
CH3+OH = CH2+H2O                 5.600E+07    1.600   5420.00
CH3+OH = CH2*+H2O                2.501E+13    0.000      0.00
CH3+O2 = O+CH3O                  2.675E+13    0.000  28800.00
CH3+O2 = OH+CH2O                 3.600E+10    0.000   8940.00
CH3+HO2 = CH4+O2                 1.000E+12    0.000      0.00
CH3+HO2 = CH3O+OH                2.000E+13    0.000      0.00
CH3+HCO = CH4+CO                 2.648E+13    0.000      0.00
CH3+CH2O = CH4+HCO               3.320E+03    2.810   5860.00
CH3+CH2 = C2H4+H                 4.000E+13    0.000      0.00
CH3+CH3(+M) = C2H6(+M)           2.120E+16   -0.970    620.00
     LOW  /  1.770E+50   -9.670   6220.00/
     TROE/  0.5325  151.00  1038.00  4970.00 /
H2/2.0/ H2O/6.0/ CH4/2.0/ CO/1.5/ CO2/2.0/ C2H6/3.0/
CH3+CH3 = H+C2H5                 4.990E+12    0.100  10600.00
CH2OH+O2 = CH2O+HO2              1.800E+13    0.000    900.00
CH4+H = CH3+H2                   6.600E+08    1.620  10840.00
CH4+O = CH3+OH                   1.020E+09    1.500   8600.00
CH4+OH = CH3+H2O                 1.000E+08    1.600   3120.00
CH3OH+H = CH2OH+H2               1.700E+07    2.100   4870.00
CH3OH+CH3 = CH3O+CH4             1.000E+07    1.500   9940.00
HCCO+O = H+CO+CO                 1.000E+14    0.000      0.00
C2H2+H(+M) = C2H3(+M)            5.600E+12    0.000   2400.00
     LOW  /  3.800E+40   -7.270   7220.00/
     TROE/  0.7507   98.50  1302.00  4167.00 /
   H2/2.0/ H2O/6.0/ CH4/2.0/ CO/1.5/ CO2/2.0/ C2H6/3.0/
C2H2+O = HCCO+H                  1.020E+07    2.000   1900.00
C2H2+O = CH2+CO                  1.020E+07    2.000   1900.00
CH2CO+H = HCCO+H2                5.000E+13    0.000   8000.00
CH2CO+H = CH3+CO                 1.130E+13    0.000   3428.00
CH2CO+OH = HCCO+H2O              7.500E+12    0.000   2000.00
C2H3+H = C2H2+H2                 3.000E+13    0.000      0.00
C2H3+O2 = C2H3O+O               1.24E+13   -0.120   1696.0
C2H4+H(+M) = C2H5(+M)            1.080E+12    0.454   1820.00
     LOW  /  1.200E+42   -7.620   6970.00/
     TROE/  0.9753  210.00   984.00  4374.00 /
   H2/2.0/ H2O/6.0/ CH4/2.0/ CO/1.5/ CO2/2.0/ C2H6/3.0/
C2H4+H = C2H3+H2                 1.325E+06    2.530  12240.00
C2H4+O = CH3+HCO                 1.920E+07    1.830    220.00
C2H4+OH = C2H3+H2O               3.600E+06    2.000   2500.00
C2H5+O = CH3+CH2O                1.320E+14    0.000      0.00
C2H5+O2 = C2H4+HO2               8.400E+11    0.000   3875.00
```

```
 C2H6+H = C2H5+H2                1.150E+08    1.900   7530.00
 C2H6+O = C2H5+OH                8.980E+07    1.920   5690.00
 C2H6+OH = C2H5+H2O              3.540E+06    2.120    870.00
 CH2CO + H = C2H3O              5.40E+11    0.454 1820.0
CH3OCH3     =      CH3+CH3O       1.380E+52 -10.85   9.664E+04
                                   rev  /   3.000E+13       .00
0.000E+00 /
CH3OCH3+OH    =    CH3OCH2+H2O     1.402E+08   1.61 -3.500E+01
                           rev   /     1.544E+08        1.31
2.303E+04 /
CH3O2+m       =      CH3+O2+m       3.450E+17   -.12  2.707E+04
                                     rev /  1.410E+16    .00 -
1.100E+03 /
CH3O2+CH3          =       CH3O+CH3O       1.900E+12    .00 -
1.200E+03
                                         rev /  2.000E+10    .00
0.000E+00 /
N+NO<=>N2+O                       2.700E+13     .000     355.00
N+CO2<=>NO+CO                     3.000E+12     .000   11300.00

END
```

Appendix B. CHEETAH 6.0 Output

CHEETAH 6.0 output for a standard gun run using the double-base propellant in M855 ammunition. Additives not in the CHEETAH database have been replaced by urea:

THE COMPOSITION

Name	% weight	% mol	% volume	Formula
nitrocellulose-13	82.700	70.358	81.432	$C_6H_{7.37}N_{2.64}O_{10.29}$
nitroglycerin	13.400	14.112	13.750	$C_3H_5N_3O_9$
urea	3.900	15.531	4.818	CH_4N_2O

Gas phase species	moles / kg of propellant
CO	1.443e+001
H_2O	1.040e+001
CO_2	5.562e+000
N_2	5.403e+000
H_2	3.096e+000
OH	1.0930e-001
H	7.802e-002
NO	1.862e-002
NH_3	6.47e-003
CHO	5.825e-003
formac	4.878e-003

HCN	3.054e-003
CH_2O	2.250e-003
O_2	1.935e-003
HNCO	1.758e-003
O	1.661e-003
NH_2	5.690e-004
HNO	1.513e-004
H_2O_2	1.018e-004

List of Symbols, Abbreviations, and Acronyms

2-D	two-dimensional
Al	aluminum
ANOVA	analysis of variance
B	boron
Ba	barium
Bi	bismuth
C_2H_4	ethylene
C_2H_6	ethane
CBP	Constant Breech Pressure
CE	combustion efficiency
CFD	computational flow dynamics
CH_2O_2	formic acid
CH_3OH	methanol
CH_4	methane
CHEMKIN	chemical kinetic
CHNO	isocyanic acid
C-J	Chapman-Jouguet
Cl	chlorine
CO	carbon monoxide
CO_2	carbon dioxide
Cu	copper
EF	emission factor
ELPI	electrical low-pressure impactor
EPA	US Environmental Protection Agency
F_C	carbon fraction

Fe	iron
GC/LRMS	gas chromatograph/low-resolution mass spectrometer
gr	graphite
H_2	hydrogen
H_2O	water
H_2S	hydrogen sulfide
HC	hydrocarbons
HCN	hydrogen cyanide
IB	interior ballistics
K	potassium
KNO_3	potassium nitrate
LLNL	Lawrence Livermore National Laboratory
MCE	modified combustion efficiency
MDL	method detection limit
MeCl	methylene chloride
Mg	magnesium
N_2	nitrogen
NASA	National Aeronautics and Space Administration
Na	sodium
NA	not applicable
NC	nitrocellulose
ND	not detected
NDIR	nondispersive infrared
NG	nitroglycerin
NH_3	ammonia
NIST	National Institute of Standards and Technology
NMOC	nonmethane organic carbon

NO_x	nitrogen oxide
NSPS	New Source Performance Standards
O_2	oxygen
OD	open detonation
PAHs	polycyclic aromatic hydrocarbons
Pb	lead
PC	particulate carbon
PM	particulate matter
PMMA	polymethylmetacrylate
PUF	polyurethane foam
RH	relative humidity
RPD	relative percent difference
RSD	relative standard deviation
S	sulfur
Sb	antimony
SNL	Sandia National Laboratories
SP2	single particle soot photometer
TNT	trinitrotoluene
UDRI	University of Dayton Research Institute
V	vanadium
VOC	volatile organic compound
Zn	zinc

1 (PDF) DEFENSE TECHNICAL INFORMATION CTR DTIC OCA

2 (PDF) DIR ARL
IMAL HRA
RECORDS MGMT
RDRL DCL
TECH LIB

1 (PDF) GOVT PRINTG OFC
A MALHOTRA

1 (PDF) ARL
RDRL WML C
K MCNESBY